Review on VUV to MIR absorption spectroscopy of atmospheric pressure plasma jets

OPEN ACCESS
IOP Publishing
Plasma Sources Science and Technology
Plasma Sources Sci. Technol. **24** (2015) 054001 (41pp)
doi:10.1088/0963-0252/24/5/054001

Review on VUV to MIR absorption spectroscopy of atmospheric pressure plasma jets

Stephan Reuter[1,2], Joao Santos Sousa[3], Gabi Daniel Stancu[4,5] and Jean-Pierre Hubertus van Helden[1]

[1] Leibniz Institute for Plasma Science and Technology (INP Greifswald), Felix-Hausdorff-Str. 2, 17489 Greifswald, Germany
[2] ZIK plasmatis, Felix-Hausdorff-Str. 2, 17489 Greifswald, Germany
[3] LPGP, UMR 8578, CNRS & Université Paris-Sud, 15 rue Georges Clemenceau, 91405 Orsay, France
[4] Ecole Centrale Paris, Grande Voie des Vignes, 92290 Chatenay-Malabry, France
[5] CNRS, UPR 288, EM2C, Grande Voie des Vignes, 92290 Chatenay-Malabry, France

E-mail: stephan.reuter@inp-greifswald.de

Received 11 March 2015, revised 15 May 2015
Accepted for publication 2 June 2015
Published 13 August 2015

Abstract

Absorption spectroscopy (AS) represents a reliable method for the characterization of cold atmospheric pressure plasma jets. The method's simplicity stands out in comparison to competing diagnostic techniques. AS is an *in situ*, non-invasive technique giving absolute densities, free of calibration procedures, which other diagnostics, such as laser-induced fluorescence or optical emission spectroscopy, have to rely on. Ground state densities can be determined without the knowledge of the influence of collisional quenching. Therefore, absolute densities determined by absorption spectroscopy can be taken as calibration for other methods. In this paper, fundamentals of absorption spectroscopy are presented as an entrance to the topic. In the second part of the manuscript, a review of AS performed on cold atmospheric pressure plasma jets, as they are used e.g. in the field of plasma medicine, is presented. The focus is set on special techniques overcoming not only the drawback of spectrally overlapping absorbing species, but also the line-of-sight densities that AS usually provides or the necessity of sufficiently long absorption lengths. Where references are not available for measurements on cold atmospheric pressure plasma jets, other plasma sources including low-pressure plasmas are taken as an example to give suggestions for possible approaches. The final part is a table summarizing examples of absorption spectroscopic measurements on cold atmospheric pressure plasma jets. With this, the paper provides a 'best practice' guideline and gives a compendium of works by groups performing absorption spectroscopy on cold atmospheric pressure plasma jets.

Keywords: atmospheric pressure plasma jets, absorption spectroscopy, UV VIS, VUV absorption spectroscopy, NIR to MIR spectroscopy, self-absorption, tuneable diode laser absorption spectroscopy (TDLAS), quantum cascade laser LAS, FTIR, broadband absorption spectroscopy

(Some figures may appear in colour only in the online journal)

1. Introduction

Since the 1990s, cold non-equilibrium atmospheric pressure plasma jets [1–6] have emerged worldwide and sparked new

application fields such as plasma medicine [7, 8], where the high reactivity at low gas temperature is crucial for interaction with sensitive biological systems. In plasma medicine, it is essential to diagnose species fluxes generated by plasma sources to identify relevant fundamental processes [9, 10]. Especially in plasma jets, which can access cavities and inactivate bacteria in for example hair root channels, these fluxes are difficult to obtain [11]. However, cold non-equilibrium plasmas pose a challenge for diagnostic techniques as many rely on equilibrium calculations and these plasmas have small dimensions and high density gradients in space and time [12]. While in gas phase chemistry, typically gas chromatography mass spectrometry is used [13], which exhibits the problem that, e.g. ozone reacts vividly in the column and disturbs the results, optical diagnostics have been a useful means to diagnose reactive species or plasma properties [12, 14–18]. Most commonly used techniques are optical emission spectroscopy and laser fluorescence based techniques [12, 14, 15, 19]. Only recently, absorption spectroscopy (AS) has been in the focus of the field as it has several advantages over other techniques. A hindrance for the application of AS, especially to characterize atmospheric pressure plasma jets (APP-jets) or, in short, atmospheric plasma jets, has to date been oflower sensitivity compared to several other techniques, as well as the line-of-sight averaged densities obtained from the measurements. Both drawbacks have been overcome by technical or methodical solutions, and improved light source and detector technology allow more and more sensitive measurement setups. With this development, the manifold advantages of AS come to light and this diagnostic method rapidly gains relevance for plasma jet diagnostics. The range of information on the environment of the species that can be deduced from spectra makes absorption spectroscopy a valuable tool for gaseous detection in plasmas. The main advantage of AS is its calibration-free nature providing absolute densities of the absorbing species without the problems of complete instrument calibration inherent to optical emission spectroscopy (OES) [20], laser-induced fluorescence (LIF) [21], or mass spectrometry (MS) techniques [22, 23]. In addition, the measurement of the absorption coefficient is based on the ratio of incident and transmitted intensities. Consequently, there is no need for measurements in absolute units of light intensities (Wm^{-2} sr^{-1} nm^{-1}) as required in OES and LIF techniques. Furthermore, the direct determination of the absolute density of the ground state is a strong inherent advantage in comparison with OES, which is restricted to the measurement of electronically excited molecules. The main drawback of AS is that the obtained densities are usually line-of-sight averaged values. But due to the intrinsic properties of absorption spectroscopy described above, the technique has the following advantages over other diagnostic methods.

Firstly, absorption spectroscopy is simple and reliable. If spectral properties (line strength, oscillator strength, or absorption cross-section) are known, the absolute density is trivially determined by one equation: the Beer–Lambert law. For stable atoms and molecules, these properties are easily obtained by measurements in reference gas cells, where species densities (ideal gas law calculation) and absorption length (cell length measurement) are perfectly controlled. In uniform plasma environments, density precision below 1% is attainable for such species. For atomic and molecular radicals or metastable species, the precision is limited by the accuracy of the spectroscopic properties provided in the databases.

Secondly, absorption-based techniques provide *in situ* diagnostics for atmospheric plasmas. These techniques can offer direct knowledge on space- and time-resolved species densities and temperatures, except for cases where the low sensitivity imposes the necessity to study species concentrations by gas extraction followed by analysis in multipass cells. In particular, atomic or molecular radical or metastable species measurements require detection only inside the plasma due to the extremely short lifetime of these species compared to stable species.

Thirdly, absorption techniques are non-intrusive diagnostics. Even the perturbation induced in the plasma using laser sources can be easily controlled. Power saturation, which is the large pumping of the excited state by the absorption process [15], can be avoided using neutral filters or polarizing attenuators. As best practice, the used laser has to be progressively attenuated until the absorption coefficient remains constant while the laser intensity is further reduced.

In a comparison to other techniques, the advantages of AS become even clearer. Being able to directly determine ground state densities by absorption spectroscopy is advantageous compared to e.g. OES measurements, where excited states are probed. In the latter, a kinetic model is required to deduce the densities of molecules in ground electronic states from the measured densities of excited states. Furthermore, measured absorption data can be fitted in real-time using molecular parameters such as line strengths and pressure-broadening coefficients listed in for example the HITRAN database. No models or further analysis after the measurements is necessary. Not only ground state densities can be gained from absorption spectroscopy. In plasma diagnostics, for example, the gas temperature is an often-sought parameter. A large number of experiments provide temperature measurements from the ro-vibronic distribution of the electronic excited states using OES (see e.g. [24]). However, these are based on assumptions about pumping and loss mechanisms of the excited states, which mainly include excitation by direct electron impact and loss by spontaneous emission. In atmospheric pressure plasmas, mechanisms such as quenching often dominate the spontaneous emission while other pumping and loss mechanisms such as pulling and excitation transfer can provide a non-equilibrated Boltzmann distribution and therefore induce errors in the resulting temperatures from electronically excited states. Information on the rotational and vibrational temperatures can be deduced from the relative densities in the rotational and vibrational levels. Therefore, a very promising solution is the determination of the gas temperature from the rotational-vibrational population distribution in the electronic ground state by absorption techniques. Because the rotational energy separation is very small (energies of meV), few collisions by heavy particles are sufficient to establish the Boltzmann equilibrium over the rotational distribution in the molecular vibrational ground state. In addition, the characteristic time for rotational-translational relaxation is

on the order of hundreds of picoseconds [25]. Reliable gas temperature (translational temperature) is therefore obtained from Boltzmann plots of the absorption data.

Often, a combination of different diagnostic techniques is advised. For example, ground state absolute density measurements are often performed by fluorescence techniques, mainly due to their very high sensitivity but with the drawback of the complex calibration of the measured signals [6]. If not compared to a fluorescent signal of a known number of molecules, this includes detector sensitivity, transmission of the optical system (fibres, filters, and spectrometers), the collection volume and the solid angle of the optics employed. In addition, for plasmas at atmospheric pressure, besides the radiative fluorescence de-excitation, collisional quenching is often an even larger competing de-excitation mechanism [6, 26]. Frequently, quenching rates are estimated from data measured at low pressures and extrapolated to atmospheric pressure [27]. Large errors are then associated to densities obtained by fluorescence as a result of the not well-known dependency of the quenching rates on the local density, nature and temperature of the colliders. A trustworthy solution is then the calibration of fluorescence signals (which includes both detectability and quenching) by absorption experiments [21, 28]. The absorption measurement is then used to convert the relative fluorescence signals into a sensitive space and time-resolved absolute density measurement.

The absorption and fluorescence techniques are then complementary, the first providing reliable absolute densities and the second providing spatial and temporal resolved measurements with higher sensitivity.

In the present review, the state of the art, best practice and applications of absorption spectroscopy from vacuum ultraviolet (VUV) to the mid infrared (MIR) spectral region are presented.

2. Absorption spectroscopy: what do you need to know?

In this chapter, a brief overview of the most important fundamental knowledge required to perform absorption spectroscopy is described. As this paper does not intend to be a textbook on absorption spectroscopy, for a more in-depth description of the basics of absorption spectroscopy the reader is referred to various books [26, 29–31] and papers [12, 15, 32, 33]. Throughout the review, fundamental equations have been listed according to the SI system. Equations explaining a mechanism are listed according to their original publication and the reference is given. It is very common in the field of spectroscopy to use CGS units. In view of the 'best practice' approach of the special issue cluster, the respective equations are given in the system used within the respective database and approaches typical for the spectroscopic research field.

2.1. Atomic and molecular absorption

Sensitive atomic and molecular absorption spectroscopy in atmospheric plasmas commonly uses permitted dipole transitions (single-photon absorption) between eigenstates in the outermost shell. From quantum mechanics, eigenstate energies are obtained as solutions of the stationary Schrodinger equation and they are a unique set of energies for atoms and molecules. Transition dipole selection rules (e.g. parity change) limit the number of allowed transitions leading to specific spectral absorption patterns for each species. For electronic transitions, these patterns are typically observed in the VUV to NIR spectral region, and, for rotational-vibrational absorption transitions, in the MIR spectral region.

The central wavelength λ_{ik} of an absorption transition line from a lower energy state i to a higher energy state k is related to the photon energy ΔE by

$$\lambda_{ik} = \frac{hc}{\Delta E} = \frac{hc}{E_k - E_i}, \tag{1}$$

where h is the Planck constant, c the speed of light, E_i and E_k are the eigenstate energies of the lower and the upper level, respectively. Wavelength calibrated absorption spectra and thus absolute absorption line or absorption band positions are determined by various techniques: Usually in the VUV to NIR spectral domains, calibrated spectrometers or wavemeters are employed, while in the MIR, Fabry–Pérot etalons and reference gas cells are used.

The unique set of transition wavelengths for each species is generally available in spectroscopic databases (see section 2.5). This allows the distinct identification of a particular species present in a plasma. Limited instrumental resolution and overlapping of multiple lines may hamper plasma species identification. This is relatively easily solved by the identification of several absorption lines of the same species. Note that a particular absorption transition in plasmas is observed only if there is a significant population density in the lower state. Consequently, absorption lines may be absent as a result of certain plasma conditions, e.g. the electron temperature. In such a case, a careful line identification procedure is required.

2.2. Beer–Lambert law

Absorption spectroscopy relies on the Beer–Lambert law, which describes the absorption of light by a sample. The Beer–Lambert law links the intensity attenuation of optical radiation through a homogeneous sample to the density N of species present in it

$$I(\lambda) = I_0(\lambda)\mathrm{e}^{-N\sigma(\lambda)L} = I_0(\lambda)\mathrm{e}^{-k(\lambda)L}, \tag{2}$$

where $I(\lambda)$ is the transmitted radiation, I_0 the incident radiation, $\sigma(\lambda)$ the wavelength dependent absorption cross-section, L the absorption path-length, and $k(\lambda)$ the wavelength dependent absorption coefficient. The degree to which light is absorbed is thus quantified, and, from the magnitude of the absorbance, the density of absorbing species in a sample can be determined

$$\text{Absorbance}(\lambda) = -\ln\left(\frac{I}{I_0}\right) = N\sigma(\lambda)L. \tag{3}$$

Absorption features, however, are never strictly monochromatic and are generally spread over a range of wavelengths centred at λ_0, resulting in the line profile of the transition.

Several processes contribute to the increase of the width of the line profile, including the lifetimes and thermal motion of the species, the collisions between species, and the influence of electric and magnetic fields on the species behaviour. Hence, the integrated absorption coefficient over an absorption line, k_λ, gives a more useful measure of the absorbance

$$\frac{1}{L}\int_{-\infty}^{\infty} -\ln\left(\frac{I}{I_0}\right) = \sigma_{\text{int}} N = k_\lambda = \int_{\text{line}} k(\lambda)\mathrm{d}\lambda, \tag{4}$$

where σ_{int} is the integrated cross-section and is defined as

$$\sigma_{\text{int}} = \int_{-\infty}^{\infty} \sigma(\lambda)\mathrm{d}\lambda. \tag{5}$$

As shown in the next section, by using the Beer–Lambert law, absolute densities of absorbing species in the plasma can be extracted directly from their spectral profiles. The spectral line positions usually provide species identification while line profiles are connected with the properties of the species in the plasma, for example their translational temperature (see section 2.4).

2.3. Population densities (ground and excited states)

2.3.1. Oscillator strength: atomic density. The allowed dipole transitions from atomic ground states to excited states have typical energies in the VUV and UV range. When absorption spectroscopy is used to probe atomic densities in the electronic excited states (metastables, resonant levels, etc.), the corresponding transition wavelengths are usually in the VIS and NIR domain. In case of non-equilibrium atmospheric plasmas, excited electronic states of atoms are not in Boltzmann equilibrium with their ground states. Because the energy separation between electronic levels is large (eVs), the main pumping mechanisms are not the heavy particle collisions but electron kinetics, excitation transfer, and radiative processes. In this case, to relate excited state densities to electronic ground states, collisional-radiative models are required. However, the density of the lower state (which can be a ground state or an excited state) in the absorption process is easily determined by

$$\int_{\text{line}} k(\lambda)\mathrm{d}\lambda = \frac{e^2\lambda_{ik}^2}{4\varepsilon_0 m_e c^2} f_{ik}\left(N_i - \frac{g_i}{g_k}N_k\right), \tag{6}$$

where $k(\lambda)$ is the absorption coefficient integrated over the entire absorption line, λ_{ik} the resonance wavelength corresponding to the electronic transition $i \rightarrow k$, f_{ik} the oscillator strength (dimensionless), N_i and N_k the densities of the lower and upper states, ε_0 the vacuum permeability, e and m_e the electron charge and mass, respectively. If the two levels are in Boltzmann equilibrium, then the relation between the absorption coefficient and the lower level density is given by

$$\int_{\text{line}} k(\lambda)\mathrm{d}\lambda = \frac{e^2\lambda_{ik}^2}{4\varepsilon_0 m_e c^2} f_{ik} N_i\left(1 - \mathrm{e}^{-\frac{h\nu}{k_B T}}\right), \tag{7}$$

where k_B is the Boltzmann constant, T the electronic temperature [K], and $h\nu$ the energy of the absorbed photons [J] with $\nu = c/\lambda$. The bracket term in the right side of equation (7) accounts for stimulated emission. In atmospheric pressure plasmas, the population of the upper state of most atoms is a very small fraction of the lower state, because of the large energy separation between levels. Therefore, the bracket term in equation (7) normally equals to one. For simplicity, the above expressions are using atomic oscillator strengths. This spectroscopic property can be found for instance in the NIST Atomic Spectra Database [34]. We recommend this database, because it includes the statistical weights of the two levels, so it is easy to apply. Notice that in equations (6) and (7) the absorption is described in wavelength space (as this is mainly being used for UV and VIS atomic transitions in literature). For practical purpose, equation (7) can be written as

$$\int_{\text{line}} k(\lambda)\mathrm{d}\lambda = 8.85 \times 10^{-13}\lambda_{ik}^2 f_{ik} N_i, \tag{8}$$

where $k(\lambda)$ is in cm^{-1}, λ in cm, and N_i in cm^{-3}, and the constant in the right side of the equation is also in cm units.

Atomic lines in atmospheric plasmas often exhibit Lorentzian profiles due to collisional broadening dominating the broadening mechanisms of the line profile. A practical expression in that case is

$$N_i = \frac{k(\lambda_0)\Delta\lambda_L}{5.64 \times 10^{-13}\lambda_{ik}^2 f_{ik}}, \tag{9}$$

where $k(\lambda_0)$ is the peak absorption coefficient ($\lambda_0 \equiv \lambda_{ik}$, the resonance wavelength), and $\Delta\lambda_L$ the full-width at half-maximum (FWHM) value of the line profile [cm^{-1}]. Notice the expressions given above are for single line absorption; when line overlapping occurs, the contributions of different species (due to unresolved transitions of the same or of different atoms) need to be considered.

2.3.2. Line strength: molecular density. Using MIR absorption spectroscopy, individual absorption lines of vibrational-rotational transitions in electronic ground state of molecules can be measured. Often used techniques are laser-based methods, e.g. tunable diode laser absorption spectroscopy (TDLAS) and quantum cascade laser absorption spectroscopy (QCLAS) or a broadband high-resolution apparatus, e.g. a high resolution Fourier transform infrared (FTIR) spectrometer. The integrated absorption coefficient $k(\nu)$ in wavenumber space ($\nu = 1/\lambda$ in cm^{-1}) over an absorption line is related to the molecular species density by

$$\int_{\text{line}} k(\nu)\mathrm{d}\nu = S(T)n, \tag{10}$$

where $S(T)$ [$\text{cm}^2\ \text{cm}^{-1}\ \text{molecule}^{-1}$] is the line strength (or the line intensity) of a specific transition at temperature T [K], and n [molecules cm^{-3}] is the total density of the molecular species in all internal states of the molecule. We choose to give here the integral of the absorption coefficient in wavenumber space because MIR spectroscopy is commonly presented in wavenumber units. It should be noted that the line strength defined in this way is temperature dependent via the Boltzmann relation between n and $N_{v,J}$, the ro-vibronic level for which the absorption is measured. The information on the rotational and vibrational temperatures can be deduced from

the relative densities in the rotational and vibrational levels. Assuming local thermodynamic equilibrium, the line strength of a particular rotational-vibrational transition is given by [35]

$$S_{v''J''}^{v'J'}(T) = \frac{8\pi^3}{3hc} V_{v''J''}^{v'J'} \frac{g_{v''J''} \exp\left(-\frac{E_{v''J''}}{kT}\right)}{Q(T)} \mathfrak{R}_{v''J''}^{v'J'} \left[1 - \exp\left(-\frac{hcv_{v''J''}^{v'J'}}{kT}\right)\right], \tag{11}$$

where v and J are the quantum numbers of the lower ($''$) and upper ($'$) ro-vibronic levels, $V_{v''J''}^{v'J'}$ [cm^{-1}] the spectral line transition wavenumber, $g_{v''J''}$ the statistical weight of the lower level, $E_{v''J''}$ the energy of the lower level, $Q(T)$ the total internal partition function, and $\mathfrak{R}_{v''J''}^{v'J'}$ the weighted transition-moment squared. The statistical weight and the total internal partition function include the electronic, vibration, rotation and nuclear spin terms (see for details [36, 37]). The term in the squared brackets accounts for stimulated emission. While for electronic transitions this term can be neglected (large ΔE), in the case of rotational–vibrational transitions probed in the electronic ground state an important population is present in the upper state. This occurs even in room temperature plasma environments. Therefore stimulated emission is often significant and needs to be considered. Most of the above molecular parameters can be found in the HITRAN database [38, 39].

While the theoretical calculation of the line strength is complex, its measurement is easily obtained for stable molecules. Experimentally, a reference cell is filled with a molecular gas at ambient temperature and controlled pressure. The gas density is calculated based on the ideal gas law. Knowing the length of the cell, the integrated absorption coefficient is then measured and the $S(T)$ at room temperature is obtained using equation (10). For radicals, however, this procedure becomes very challenging. Due to their short lifetimes, a complex apparatus is needed to generate and maintain high radical densities, and calibration methods are then used to measure absolute radical population (e.g. [37]). Therefore, much less spectroscopic parameters of radical species are found in databases, strongly limiting absolute radical density measurements in plasmas nowadays.

2.3.3. Effective absorption cross-section: molecular density. When using broadband absorption techniques (e.g. grey body lamps) or unresolved molecular spectral features are measured by laser absorption (e.g. absorption of large molecules or absorption with pre-dissociation of the electronic excited state), effective absorption cross-sections are needed for species density measurements. In these cases, often the rotational, vibrational molecular spectral features are unresolved, resulting in a structureless absorption spectrum. Consequently, densities are obtained not from a single line absorption but from unresolved molecular bands, which are spectrally convolved with the instrumental functions. Absolute concentrations can then be obtained if not a distinct point in the spectrum is analysed, but a carefully defined spectral range $\Delta\nu$, which is in fact additional averaging. This gives the following relation between the molecular density and the effective absorption cross-section, $\sigma_{\text{eff}}(\nu)$ [40],

$$\sigma_{\text{eff}}(\langle\nu\rangle) = \frac{1}{nL} \ln\left(\frac{I_0(\langle\nu\rangle)}{I(\langle\nu\rangle)}\right) = \frac{1}{nL} \ln\left(\frac{\langle I_0(\nu)\rangle \cdot \Delta\nu}{\langle I_0(\nu)\rangle \cdot \Delta\nu}\right) = \frac{1}{nL} \ln\left(\frac{A_0}{A}\right). \tag{12}$$

In this way, the least error prone density determination is to not calculate the absorbance from the transmitted intensity I at ν, but to use the area (or integral) $A \approx I\Delta\nu$. In the calculation of σ_{eff}, the contribution of $\Delta\nu$ cancels out in equation (12), i.e. $\sigma(\lambda)$ is in cm^2 units. The effective absorption cross-section can depend on temperature, pressure, and instrumental resolution. When very high-resolution absorption devices are used, instrumentally independent cross-sections are needed. Otherwise, cross-section data need to be convolved with the instrumental function employed in the plasma diagnostic experiment. Underestimated densities are obtained if instrumental functions are disregarded. Absorption cross-sections from UV to MIR for molecular species can be found for example in the HITRAN database [39].

2.3.4. Power saturation. In case a high power light source such as a laser is used for the absorption measurements power saturation phenomena have to be avoided. Otherwise, the diagnostic is no longer non-intrusive. The absorption of radiation inherently reduces the population density in the lower state of the transition to which the laser frequency is tuned, and increases the density in the upper state. This modification of population densities should be such that the measured signal is still representative of the initial density of the lower state. At relatively high radiation powers (especially for lasers), this may be no longer the case. That no power saturation occurs can relatively simple be checked by repeating the absorption measurement for different radiation powers since the measured absorption percentage should be independent of the power. An overview on how to estimate the influence of power saturation on absorption measurements and on the determination of the saturation parameter S using a variety of techniques is discussed in [15].

2.4. Lineshape and broadening mechanisms

In absorption spectroscopy, line profile shapes can be gained from which properties of the plasma species can be derived. This is especially of interest where emission does not occur and emission spectroscopy or fluorescence spectroscopy are not alternative diagnostic methods. The area of the spectral profile yields the species density, while the spectral profile can be used to gain more insight into the mechanisms of line broadening. The lineshape of the spectral profile is determined by several factors dictated by the spectroscopic properties of the species studied as well as the experimental conditions such as the pressure and temperature of the gas sample and the existence of electric and magnetic fields. These factors can be divided into homogenous and non-homogeneous categories, i.e. contributions to the lineshape that affect every element present in the sample in an identical way, or contributions which arise from an average effect that is not identical to every

element, respectively. Here, the relevant mechanisms behind the lineshape of the spectral profile will be briefly discussed. They include natural broadening, collisional broadening (resonance and van der Waals broadening), Doppler broadening, Stark broadening, instrumental broadening, and saturation broadening. For a more detailed description and mathematical expressions, we refer the reader to [14, 15, 24, 29, 30, 41].

2.4.1. Natural line broadening. One example of a homogenous contribution to the lineshape is natural broadening, which arises from the natural lifetime, τ, of the upper state of the transition. From the Heisenberg uncertainty principle, $\tau\,\Delta E \geqslant \hbar$, it can be seen that the consequence of a finite lifetime of the upper state is an uncertainty in the corresponding energy and, therefore, the state is described by a range of energies, ΔE. The resulting natural broadening effect has a Lorentzian lineshape, but this contribution to the width of the absorption lineshape is, however, very small, being normally negligible in comparison with other broadening contributions.

2.4.2. Collisional broadening. Another example of homogeneous broadening of the lineshape is collisional broadening. When collisions in a gaseous sample containing atoms and/or molecules occur, this effectively reduces the natural lifetime of the transition and thus increases the uncertainty in the energy of the transition, i.e. there is a broadening of the lineshape. The extent of the lineshape broadening depends on the nature of the energy transfer during a collision, and of the natural lifetime of the transition compared to the frequency of collisions. As the pressure increases and the interval between collisional events reduces, the extent of broadening of the lineshape increases. The collisional broadening has two components: pressure-induced broadening, also known as van der Waals broadening, and resonance broadening. The former is due to collisions of the absorbing particle with neutral perturbers that do not share a resonant transition with the radiating particle. The latter is due to collisions with perturbing particles with similar energy levels as the absorbing particle, which introduces the possibility of an energy exchange process (when both particles are from the same species this is often termed self-broadening in literature). Collisional broadening leads to a Lorentzian lineshape, analytically described by

$$L(\nu) = \frac{2}{\pi}\frac{\Delta\nu_{\mathrm{L}}}{\Delta\nu_{\mathrm{L}}^2 + 4(\nu-\nu_0)^2}, \tag{13}$$

where $\Delta\nu_{\mathrm{L}}$ is the Lorentzian linewidth given as a full width half maximum (FWHM) value and ν_0 is the resonance frequency, i.e. the line center of the absorption profile. The Lorentzian linewidth due to collisional broadening is often conveniently expressed as

$$\Delta\nu_{\mathrm{L}} = 2\gamma p, \tag{14}$$

with p being the operating buffer gas pressure [atm] and γ the pressure broadening coefficient dependent on the nature of the colliding species, generally given in half width half maximum (HWHM) [cm^{-1}/atm] at $T_{\mathrm{ref}} = 296$ K and reference pressure $p_{\mathrm{ref}} = 1$ atm. This parameter is transition dependent [35]. The broadening coefficient is often tabulated in literature in spectroscopic databases (see section 2.5). If the broadening coefficients are not tabulated in the literature, which is often the case for atoms, then they have to be calculated using the analytical expressions of resonance and van der Waals broadening as one can find in the book by Griem ([30], p 97 and 99). Resonance broadening occurs if either the lower (l) or the upper (u) state of the radiative transition under consideration is the upper level of a resonance transition, i.e. if the level is connected to the ground state (g) by an allowed dipole transition [31]. When including all three perturbing transitions, the resonance broadening can be expressed as [14]

$$\Delta\lambda_{\mathrm{resonance}} = \frac{3e^2}{16\pi^{2\varepsilon_0 m_e c^2}}\lambda_{\mathrm{ul}}^2\left[\lambda_{\mathrm{lg}} f_{\mathrm{gl}}\sqrt{\frac{g_{\mathrm{g}}}{g_{\mathrm{l}}}}\,n_{\mathrm{g}} + \lambda_{\mathrm{ug}} f_{\mathrm{gu}}\sqrt{\frac{g_{\mathrm{g}}}{g_{\mathrm{u}}}}\,n_{\mathrm{g}} + \lambda_{\mathrm{ul}} f_{\mathrm{lu}}\sqrt{\frac{g_{\mathrm{l}}}{g_{\mathrm{u}}}}\,n_{\mathrm{l}}\right]. \tag{15}$$

Van der Waals broadening for radiator r colliding with perturber p is given by [14]

$$\Delta\lambda_{\text{van der Waals}} \approx \frac{\lambda_{\mathrm{ul}}^2}{2c}\left(\frac{9\pi\hbar^5\overline{R_\alpha^2}}{16 m_e^3 E_p^2}\right)^{\frac{2}{5}} \overline{v_{rp}^{\frac{3}{5}}} N_p, \tag{16}$$

where E_p is the energy of the first excited state of the perturber connected with its ground sate by an allowed transition, N_p the number density of the perturber, v_{rp} the relative speed of the radiating atom and the perturber, and the matrix element $\overline{R_\alpha^2}$ equals to

$$\overline{R_\alpha^2} \approx \frac{1}{2}\frac{E_{\mathrm{H}}}{E_\infty - E_\alpha}\left[5\frac{z^2 E_{\mathrm{H}}}{E_\infty - E_\alpha} + 1 - 3l_\alpha(l_\alpha+1)\right]. \tag{17}$$

Here, E_{H} and E_∞ are the ionization energies of the hydrogen atom and of the radiating atom, respectively, E_α the term energy of the upper state of the transition, l_α its orbital quantum number, and z the number of effective charges ($z = 1$ for a neutral emitter, $z = 2$ for a singly ionized emitter, etc) [14]. In [14], the values of the HWHM contributions of the various broadening mechanisms to the line profile of the H_β line at 486.132 nm are calculated for an air plasma with a few percent of hydrogen (see table 1).

Collisional broadening of the lineshape tends to dominate at atmospheric pressure and Doppler broadening, an example of inhomogeneous broadening, is negligible especially for cold plasmas. At higher temperatures, however, its contribution has to be taken into account, and from it the translational temperature of the species can be obtained.

To conclude this subsection, we would like to point out that even if the profile is pure Lorentzian, due to the Doppler broadening being very small, in principle a value for the temperature can still be obtained via the expression for the temperature and pressure correction of the pressure broadening coefficient. The pressure broadened coefficient $\gamma(p,T)$ for a gas at pressure p [atm], temperature T [K], and partial pressure p_{s} is given by the following expression [35]:

Table 1. HMHM (in nm) for the H_β line at 486.132 nm. P is the pressure in atm, T the gas temperature in K, n_e the electron number density in cm^{-3}, and X_H the mole fraction of hydrogen atoms [14].

$\Delta\lambda_{Stark}$	$\Delta\lambda_{resonance}$	$\Delta\lambda_{van\ der\ Waals}$	$\Delta\lambda_{Natural}$	$\Delta\lambda_{Doppler}$
$1.0 \times 10^{-11}(n_e)^{0.668}$	$30.2X_H(P/T)$	$1.8P/T^{0.7}$	3.1×10^{-5}	$1.74 \times 10^{-4}T^{0.5}$

$$\gamma(p,T) = \left(\frac{T_{ref}}{T}\right)^n (\gamma_{air}(p_{ref},T_{ref})(p-p_s) + \gamma_{self}(p_{ref},T_{ref})p_s), \quad (18)$$

where n is the coefficient of temperature dependence of the pressure broadening coefficient. In the absence of other data, the coefficient of temperature dependence of the self-broadening coefficient is assumed to be equal to that of the pressure broadening coefficient. Alternatively, the classical value of 0.5 can be used by default.

2.4.3. Doppler broadening. Doppler broadening results from the shift in the frequency of the absorbed radiation during a transition, and this shift is dependent on the relative velocity of the absorber with respect to the direction of propagation of the radiation. For an atom or molecule that absorbs at a resonant frequency of ν_{res} when stationary, the actual frequency at which the transition is observed is shifted to ν_a when the molecule travels with velocity, v, away from the radiation source and is given by

$$\nu_a = \frac{\nu_{res}}{1 - v/c}. \quad (19)$$

As a result of thermal motion, the molecules within the sample exhibit a Maxwellian distribution of their velocities along the propagation direction of the radiation, leading to a distribution of absorbed frequencies according to the direction of the particle's motion relative to the source. This inhomogeneous mechanism gives rise to the following normalized Gaussian lineshape

$$G(\nu) = \frac{2}{\Delta\nu_{Dopp}}\sqrt{\frac{\ln 2}{\pi}}\exp\left[-\frac{4\ln 2(\nu-\nu_0)^2}{\Delta\nu_{Dopp}^2}\right], \quad (20)$$

where $\Delta\nu_{Dopp}$ is the FWHM Gaussian linewidth for Doppler broadening with its dependence on temperature, T, given by

$$\Delta\nu_{Dopp} = 2\nu_0\sqrt{\frac{2\ln 2\, k_B T}{mc^2}} = 7.16\times10^{-7}\nu_0\sqrt{\frac{T}{M}}, \quad (21)$$

where m is the molecular mass and M the molecular weight. Additionally, as the equation above highlights, the FWHM Doppler contribution, $\Delta\nu_{Dopp}$, is an increasing function of the resonant frequency, ν_0, and thus ranges from tens of MHz in the mid-infrared, up to a few GHz in the UV. Such dependence results in different instrumental resolutions required for conducting Doppler-resolved studies in different regions of the electromagnetic spectrum.

2.4.4. Stark broadening. The interaction of a molecule with the electric field caused by the free electrons in the sample can be thought of as many weak collisions with the electrons. This results in a lifetime shortening (like in collisional broadening) of the molecular state under consideration. When the contribution of electrons is much higher than that of ions, the Stark broadening is characterized by a Lorentzian profile, whose FWHM is directly related to the electron density. OES measurements on the H_β-line are commonly used for the determination of electron densities ranging from 10^{14}–10^{18} cm^{-3} [19]. However, absorption spectroscopy on this transition is not trivial. Alternatively, one could in principle use measurements on metastable argon or helium atoms. The Stark broadening, however, is generally much smaller than the Doppler and collisional broadening. Therefore, the contribution of Stark broadening to the line profile is hard to determine and is usually neglected [42]. Despite these problems, in [43], an estimation of the electron density was performed in an argon/oxygen micro structured electrode discharge up to a pressure of 400 mbar; although, this was not possible at higher pressures. For more detailed information, we refer the reader to a review on Stark broadening in this special issue cluster [41].

2.4.5. Instrumental and saturation broadenings. When deducing properties of the plasma from the lineshape of a spectral absorption profile, one has to take into account the influence of the spectrometer or the laser on the lineshapes, i.e. instrumental broadening. Depending on the components of the spectrometer (laser), this instrumental broadening can have a Gaussian or a Lorentzian lineshape with FWHM linewidth $\Delta\nu_{inst}$. Preferably, the instrumental linewidth of the spectrometer is much smaller than or similar to the spectral width of the investigated atomic or molecular transition. When the instrumental linewidth is comparable or larger than the width of the spectral linewidth, large errors can be made when deconvoluting the spectra profile to obtain information on parameters such as temperature or other broadening mechanisms. This is generally less of an issue for atmospheric pressure plasmas due to larger collisional broadening of the studied spectral profiles compared to instrumental broadening. Another broadening effect appears in case of power saturation. Due to the optical coupling of the lower and the upper states by the radiation field, the homogeneous line width of the transition is broadened and becomes $\Delta\nu_S = \Delta\nu_L\sqrt{1+S}$ [15], S being the saturation parameter. In this case, the absorption coefficient gets smaller in amplitude and larger in width.

2.4.6. Best practice on analysis of the absorption spectral profile. After recording a spectral profile of a single transition of the species of interest, there are various ways to analyse the data to obtain absolute number densities. The most accurate values are obtained by using the integrated absorbance as defined in equation (4) or the area under the line profile of the fractional absorption ($A(\nu)$) of any absorption spectral profile. The latter has to be sometimes used instead of the absorbance as discussed in detail in this section, and the integrated fractional absorption, W, is defined as:

$$W = \int A(\nu)\mathrm{d}\nu = \int 1 - \frac{I(\nu)}{I_0(\nu)}\mathrm{d}\nu = \int 1 - \exp(-\sigma(\nu, T)NL)\,\mathrm{d}\nu. \quad (22)$$

Note that the integrated cross-section has to be known; how to obtain it is discussed in section 2.2. The density can also be obtained from the peak absorbance or fractional absorption of an isolated line if the peak absorption cross-section is known. The peak absorption cross-section can be obtained from the integrated cross-section by incorporating the lineshape function $\Phi(\nu)$

$$\sigma_{\mathrm{peak}} = \sigma_{\mathrm{int}}\Phi(\nu). \quad (23)$$

The lineshape function is normalised, so that its integral over wavenumber is one

$$\int_{-\infty}^{\infty}\Phi(\nu - \nu_0)\mathrm{d}\nu = 1. \quad (24)$$

In the case of a pure Gaussian lineshape function, $\Phi(\nu)$ can be written as

$$\Phi(\nu) = \sqrt{\frac{4\ln 2}{\pi}}\,\frac{1}{\Delta\nu_{\mathrm{G}}}. \quad (25)$$

In case of a pure Lorentzian lineshape function, $\Phi(\nu)$ can be written as

$$\Phi(\nu) = \frac{2}{\pi}\,\frac{1}{\Delta\nu_{\mathrm{L}}}. \quad (26)$$

For conditions where there are appreciable contributions from different mechanisms, the lineshape takes a form that is a convolution of the Gaussian and Lorentzian components, namely a Voigt lineshape that can be described by

$$V(\nu, a) = \frac{2}{\Delta\nu_{\mathrm{G}}}\sqrt{\frac{\ln 2}{\pi}}\,\frac{a}{\pi}\int_{-\infty}^{\infty}\frac{\mathrm{e}^{-t^2}}{a^2 + (x - t)^2}\mathrm{d}t, \quad (27)$$

where x and a are given by

$$x = \sqrt{\ln 2}\,\frac{2(\nu - \nu_0)}{\Delta\nu_{\mathrm{G}}} \text{ and } a = \sqrt{\ln 2}\,\frac{\Delta\nu_{\mathrm{L}}}{\Delta\nu_{\mathrm{G}}}. \quad (28)$$

In the case of multiple Gaussian profiles, the overall FWHM Gaussian linewidth is given by the square root of the combination in quadrature of components, for example

$$\Delta\nu_{\mathrm{G}} = \left(\Delta\nu_{\mathrm{inst}}^2 + \Delta\nu_{\mathrm{Dopp}}^2\right)^{1/2}, \quad (29)$$

while the overall FWHM Lorentzian linewidth is given by the sum of each individual contribution. The best analytical approximation of the FWHM width of the Voigt profile, $\Delta\nu_{\mathrm{Voigt}}$, with an accuracy of 0.02% is given by [44]

$$\Delta\nu_{\mathrm{Voigt}} \approx 0.5346\Delta\nu_{\mathrm{L}} + \sqrt{0.2166\Delta\nu_{\mathrm{L}}^2 + \Delta\nu_{\mathrm{Dopp}}^2}. \quad (30)$$

In case of a Voigt lineshape function, $\Phi(\nu)$ can be written as [45]

$$\Phi(\nu) = \frac{1}{\left[1.065 + 0.447\left(\frac{\Delta\nu_{\mathrm{L}}}{\Delta\nu_{\mathrm{Voigt}}}\right) + 0.058\left(\frac{\Delta\nu_{\mathrm{L}}}{\Delta\nu_{\mathrm{Voigt}}}\right)^2\right]\Delta\nu_{\mathrm{Voigt}}}. \quad (31)$$

In for example [46], it was shown that when the spectral line profile is much narrower than the spectral resolution of the spectrometer, using the peak fractional absorption can lead to an underestimation of the real density. Furthermore, it was demonstrated that for strongly absorbed lines, the area under the absorbance is not conservative, i.e. again the density is not correctly determined from the integrated absorbance. Therefore, in such a case, the area under the fractional absorption, W, has to be used to obtain the correct density, regardless of the instrumental function of the spectrometer. An example where the integrated fractional absorption has to be considered is given in [47], where a 310 nm light-emitting diode (LED) is used as a light source together with a very high resolution spectrometer to record the spectra (2.6 pm resolution). Despite this high resolution, the real linewidth is still much smaller. Therefore, to obtain the absorption spectrum of OH(X), the fractional absorption, A(λ), has to be determined, which is now defined as follows [47]

$$A(\lambda) = 1 - \frac{I(\nu)}{I_0(\nu)} = 1 - \frac{L_{\mathrm{plasma+LED}}(\nu) - L_{\mathrm{plasma}}(\nu)}{L_{\mathrm{LED}}(\nu) - L_{\mathrm{background}}(\nu)}. \quad (32)$$

Therefore, four spectra have to be recorded: the background spectrum with LED and plasma off ($L_{\mathrm{background}}$), the spectral emission of the LED without the plasma (L_{LED}), the emission of the plasma without LED (L_{plasma}) and the transmitted light of the LED with the plasma on ($L_{\mathrm{plasma+LED}}$). Integrating over the spectral line profile of the transition and using a modified equation (26), the OH(X) density in the ground state of a particular rotational state, N_i, can be determine as follows

$$W = \int A(\nu)\mathrm{d}\nu = \int 1 - \exp\left(-\frac{hc}{\nu}B\Phi(\nu)N_iL\right)\mathrm{d}\nu, \quad (33)$$

where B is the Einstein coefficient for absorption. Note that the area under the spectral profile, W, is independent of the spectral line profile, and the experimental spectral profile without including the instrumental broadening has to be considered only in the exponential of the right-hand side.

2.5. Databases and tools

To obtain absolute species densities in plasmas using light absorption diagnostics, it is essential to know the spectroscopic properties of atoms and molecules. Firstly, data on energy levels together with selection rules provide spectral line positions observed in spectra. This is a key parameter for identification of species present in plasmas. Secondly, oscillator strengths, line strengths, absorption cross-sections and broadening coefficients are key properties for absolute densities and temperature measurements in plasmas. Nowadays, free-access spectroscopic databases contain these properties for most atoms and many molecules. Nonetheless, there is a lack of these properties for a large number of radical species. Furthermore, for atmospheric plasmas, accurate data on the pressure broadening coefficients of transitions is necessary to accurately be able to use fitting routines to obtain values for the densities and line broadening mechanisms. These values are also not always available in the literature. In particular for molecules, comparison of measured spectra with simulations

Table 2. Molecules and electronic transitions available in Specair [48].

Molecule/ transition	X-X	A-X	B-X	C-X	D-X	B′-X	E-X	A-B	C-B	D-A
O_2			X							
NO	X	X	X	X	X	X	X			
N_2								X	X	
N_2^+			X							
OH	X	X	X							
NH		X								
CO	X	X								
C_2										X
CN		X	X							

is often necessary. The large number of possible transitions, the appearance of spectra that strongly depend on temperature, the pressure broadening, the instrumental function and the spectral overlapping make the species identification and the density as well as temperature measurements practically unfeasible without adequate simulation tools. Here, examples of databases and tools for absorption spectra simulations are given.

2.5.1. NIST atomic spectra database. The NIST Atomic Spectra Database [34] of the National Institute of Standards and Technology (NIST) is particularly adequate if densities of atoms and atomic ions in ground and excited states (e.g. resonant, metastable) are to be probed by absorption spectroscopy. Energy levels and transitions are represented in a Grotrian diagram and the associated oscillator strengths are provided. This is useful for the choice of transition to use and detection sensitivity calculations. The NIST Atomic Spectra Database includes observed transitions of 99 elements and energy levels of 89 elements, with in total more than 90 000 energy levels and 180 000 lines. A key point for species density measurements in plasmas is the availability of 73 000 transitions for which oscillator strengths are given.

2.5.2. Specair tool. Specair is a commercially available program for calculating emission or absorption spectra of radiation of air plasmas [48]. It calculates electronic molecular spectra (VUV-IR) based on a wide range of parameters, which include plasma column length, pressure, gas temperature, and rotational, vibrational and electronic temperatures. If instrumental functions are measured, they can be use as well as an input parameter in the spectral simulations. In table 2, a list of molecules with the available electronic transitions is presented. Absorption coefficients [cm^{-1}] can be simulated by Specair for numerous plasma conditions. NO, CO and OH MIR rotational-vibrational transitions are also included together with atomic transitions of N, O and C.

2.5.3. LIFBASE tool. LIFBASE, available as freeware from SRI, is a program to chart the spectroscopy of diatomic molecules. In LIFBASE, absolute ro-vibrational emission and absorption coefficients are listed, with a variation of transition probabilities taking into account ro-vibrational wavefunctions and electronic transition moments. The program contains rotational radiative lifetimes and tabulated predissociation rates and frequencies for all ro-vibrational transitions. Spectral simulations of optical emission, absorption, excitation, laser-induced fluorescence, including thermal and non-thermal population distributions, and line broadening effects can be performed. The graphics interface allows an interactive change of simulation parameters. At present, the following molecules and electronic bands are covered [49] (see table 3):

Table 3. Molecules and electronic bands covered by LIFBASE [49].

Molecule/ transition	A-X	B-X	C-X	D-X
OH	X			
OD	X			
NO	X	X	X	X
CH	X	X	X	
CN		X		
CF	X	X		
SiH	X			
N_2^+		X		

Especially for the evaluation and simulation of laser induced fluorescence spectra of OH and CH in flames, *LASKIN*, a simulation tool of time resolved LIF spectra, can be used [50].

2.5.4. HITRAN database. HITRAN is an acronym for HIgh-resolution TRANsmission molecular absorption database [38, 39]. HITRAN is a compilation of spectroscopic parameters of molecules relevant for the prediction and simulation of the transmission and emission of light in the atmosphere including many trace constituents. Initially concentrating on the infrared spectral region, it also contains nowadays data in spectral regions beyond the infrared. The database is freely accessible through the HITRAN website run by the Harvard-Smithsonian Center for Astrophysics. For plasma spectroscopy, the traditional line-by-line spectroscopic parameters, such as the line strength, the Einstein-A coefficient and the pressure broadening coefficients required in fitting routines of spectra to obtain species densities are of most interest. Spectroscopic parameters of 47 molecules and their isotopologues are currently in the HITRAN database. Many of those are relevant for plasma spectroscopy such as H_2O, CO_2, O_3, N_2O,

CO, NO, NO_2, HNO_3, and OH. A helpful tool for analysis of absorption spectra is the commercially available software Q-MACSoft-HT that visualizes the HITRAN database [51].

2.5.5. PNNL database. Although the acronym 'PNNL database' is often used in the spectroscopic community, its full name is the PNNL Northwest-Infrared vapor phase infrared spectral library [52]. The database is freely accessible and contains information about infrared spectra of over 400 compounds. Although it does not contain information on the line-by-line spectroscopic parameters, the data give enough information to calculate effective absorption cross-sections.

2.5.6. The MPI-Mainz UV/VIS spectral atlas of gaseous molecules of atmospheric interest. A further example for a cross section database is the MPI-Mainz UV/VIS Spectral Atlas [53, 54], which is a comprehensive collection of cross sections for gaseous molecules and radicals, primarily relevant to earth atmosphere research. These molecules often are the same that are relevant to atmospheric pressure plasma community. The database lists absorption cross-sections and photon yields for photochemical reactions. It is a collection of data sets from original publications. In addition, several spectra were obtained from databases of several research centers and via private communication. As of February 2015, the database contains 5722 cross section data files for 962 species, 151 quantum yield data files for 30 reactions, 1629 references, and 2536 graphical representations.

2.5.7. PGOPHER. PGOPHER [55] is a software package to simulate rotational, vibrational and electronic spectra. It has been developed at the University of Bristol in the UK. With PGOPHER molecular spectra can be simulated from the basic spectroscopic parameters generally available in the literature to give line positions and line strengths. In this way, the lack of line-by-line spectroscopic parameters of radicals can be overcome as it has been reported in literature [56, 57].

2.6. Detection limit and sensitivity enhancement

Let us have a closer look at the Beer–Lambert law presented in section 2.2. The sensitivity achieved with an absorption spectroscopy technique can be characterized by the ratio of signal-to-noise (S/N). Signal (S) here corresponds to the measured fractional change of intensity through a sample, and noise, N, is the standard deviation of the baseline signal. In this case, it is evident that in order to increase the signal magnitude and thus the sensitivity of absorption spectroscopy, there are two relevant variables: the optical path length and the absorption cross-section. The path length may be increased, whether by a multipass cell or through the use of an optical cavity, as it is discussed in detail in section 2.6.1. The absorption cross-section, a measure of how strongly a molecule interacts with light, whilst not initially appearing to be mutable, is in fact variable. A given molecule absorbs at a wide range of wavelengths corresponding to transitions between different forms of energy levels (rotational, vibrational and electronic) with cross-sections varying by many orders of magnitude. However, in the process of choosing the right spectral region to use for absorption spectroscopy other factors come into play such as the availability of simple-to-use light sources and the possibility of multiple species absorbing at the same wavelength. Thus, it is important to choose the spectral region of your absorption measurement wisely (see section 2.6.2). Reducing the noise is another way to increase the signal-to-noise ratio. This can be achieved for example by using modulation techniques (see section 2.6.3).

2.6.1. Absorption length. One main disadvantage of simple absorption techniques is that the absorption is measured with a line-of-sight approach. As a result, the determined density is a spatially averaged value over the absorption length. The same is true for the temperature or pressure obtained from the measured spectral profile. Related to that is the question: how accurate is the effective absorption path length known? The geometry of a plasma jet is generally very small (in μm to cm range). This severely limits the sensitivity of the method. In conventional linear absorption spectroscopy, an increase in absorption path length is often realized by folding the laser beam using multiple pass optics. Most commonly, two different types of multipass cells are used: White cell [58] and Herriott cell [59]. The multipass White cell consists of three independently movable mirrors (one field mirror and two objective mirrors) to adjust the multi-reflection pathway of the laser beam. This type of multipass cell has been used for example to perform MIR laser absorption spectroscopy of ozone in an atmospheric plasma jet [60]. The second type is the Heriott-type multipass cell, which relies on only two mirrors. It is more stable than the White cell but can only accept low aperture beams and requires large mirrors for long absorption path lengths. Herriott-type multiple-pass cells, however, are less prone to etalon formation than are White cells. Often an astigmatic Herriott-type multipass cell is used, for example in the case of tunable diode laser absorption spectroscopy to detect the NO production rate of an atmospheric plasma jet [61]. The absorption path length is generally below 100 m when a multipass cell is combined with a plasma jet. Furthermore, in the case of a plasma jet with its small geometry, the effluent has to be placed in the multipass cell and the concentration measured corresponds to the average concentration over the measuring volume, i.e. the entire volume of the multipass cell. This makes it harder to establish a direct correlation between the measured densities in the multipass cell and the production rate of species in the plasma jet. Despite these disadvantages, it has been shown that with this method very accurate concentration measurements of species generated by the plasma jet can be performed [60, 61]. In [60], complimentary OES measurements are used to determine the space-resolved distribution of the densities. Increasing the effective absorption length by employing high finesse optical cavities can provide increased sensitivities as kilometric path lengths can be achieved at inherently small base lengths in a small volume. For details on cavity ring down spectroscopy (CRDS) and cavity enhanced absorption spectroscopy (CEAS) techniques, see [62, 63] and references therein. This method is ideally suited for localized measurements in plasma jets. For

more details, see the devoted contribution in this special issue cluster.

2.6.2. Choice of the spectral region. As mentioned in the beginning of this section, it is important to choose the spectral region of the absorption measurement wisely. Firstly, a given molecule absorbs at a wide range of wavelengths corresponding to transitions between different forms of energy levels. Strong electronic transitions mainly occur in the UV and visible spectral range, while strong fundamental vibrational transitions are in the MIR spectral range (3–20 μm). In the NIR, many transitions in overtone and combination bands of molecules have their absorption wavelength, although these are generally weaker than in the UV or the MIR. As a consequence, the absorption cross-sections for the same molecule vary by many orders of magnitude over the whole spectral region. Furthermore, the absorption cross-section is temperature dependent. This means that the ideal transition to use to obtain the highest sensitivity changes with the temperature of the species in the plasma. In connection with this, the temperature of the species under investigation has to be known to ensure that the correct value for the absorption cross-section is used to determine the density from the measured absorption spectra. Another aspect that needs to be taken into account is that in the UV and NIR range, light sources are more readily available than in the MIR domain. This comes with the drawback that spectra are more congested in the UV and NIR spectral region compared to MIR. One of the main problems of working in the UV region is that many molecules have absorptions there in a small spectral window, meaning that at one specific wavelength multiple molecules can absorb light and overlap of molecular spectra easily occurs. This makes selectivity for the respective species under investigation more difficult. Absorption spectroscopy on atmospheric plasma jets has another aspect that needs to be considered when choosing the spectral region for the absorption spectroscopy experiments. Working at atmospheric conditions means that molecules present in the surrounding atmosphere are also detected at certain wavelengths, this is especially true for water and carbon dioxide. Due to their strong absorption cross-sections and their high abundance in the atmosphere, these species efficiently absorb NIR and MIR radiation. Therefore, they may disturb significantly the diagnostic of other species. For example, NO_2 and water absorption spectra overlap in many spectral ranges. By using the very narrow spectral radiation of laser sources, a spectral region can be selected with high specificity, i.e. where the overlapping is negligible or well contained. Moreover, the 3–5 μm and 8–10 μm MIR regions are relatively free of atmospheric absorbers such as water vapour.

2.6.3. Light sources for absorption spectroscopy. A key item of an absorption spectroscopy experiment that has a big influence on the choice of the spectral region is the availability and properties of light sources. Especially the introduction of new light sources applied to plasma spectroscopy has triggered the use of absorption spectroscopy for smaller and smaller absorption lengths at shorter and shorter integration times. Two separate developments were significant. The wavelength range extension of light emitting diodes (LEDs) to the UV spectral range [28, 64], and the development of new laser sources including novel broad band lasers with high time resolution [65], or the introduction of simple to use quantum cascade laser systems for the MIR spectral region [66]. The extension of the wavelength range of light sources and their increased stability has significantly improved absorption spectroscopy in the last decades. A few light sources are described briefly in the following—quantum cascade lasers are discussed in more detail in section 3.4.2. The use of VUV radiation grants the access to light atoms such as O, N or H, as their transitions from the ground state usually lie in the VUV spectral range [67]. In this spectral region, two-photon techniques such as TALIF allow diagnostics without the use of vacuum ultra violet radiation [6] at the significant drawback that calibration is intricate. The most common way to generate VUV radiation is by discharge lamps. Other means to generate VUV generation is by stimulated Raman Scattering. Here, Raman Anti-Stokes radiation is generated when energy is transferred from the scattering molecules to the scattered photons. This occurs only when excited states are present, which can transfer additional energy to the incident photon. Raman scattering of intensive laser light generates a multitude of Stokes transition resulting in many excited states. This technique has been used to generate VUV Laser radiation at and below Lyman α [68, 69]. Many other interesting light sources ranging from the extreme UV (EUV) to the UV have been reported in literature to study low pressure plasmas using absorption spectroscopy. A pulsed soft x-ray source was used to generate EUV light [70, 71] and VUV radiation was created with a deuterium lamp [72]. For resonance absorption, a high pressure N_2 microdischarge hollow-cathode lamp [73], a dual-tube inductively coupled plasma light source [74] and via a surface wave excited discharge in Ar/O_2 at 130 nm to measure O atoms [75] were used. In the UV spectral region, the commonly used Xe or D_2 lamp sources [46, 64] are being increasingly replaced by UV LEDs [64, 72, 76]. The main reason behind this is that the former are unstable, leading to baseline fluctuations, reducing the sensitivity of the technique. Whereas LEDS have such a stable baseline that here, the baseline noise is the limiting factor ($<10^{-4}$). LEDs are solid-state light sources which provide a very bright light point without intensity fluctuations when the LED is thermo-regulated and fed by a stabilized current source. They cover the spectral range 240 nm–1500 nm with power >200 μW. Each diode has typically a spectral width of about 15 nm [28, 64, 76]. To enhance the quality of the setup, a collimating optics as shown in figure 1 can be applied, which transforms the LED into a point source and with the help of a lens produces a collimated beam [77].

An interesting new light source presented recently is a broadband light source (200–1000 nm), which is actually a laser induced plasma light source (laser-driven light source, Energetiq Technology, Inc.) for broadband absorption spectroscopy. A novel absorption spectroscopy setup was presented which allowed 250 nm-wide spectra to be recorded with random noise and baseline stability better than 10^{-4} [78]. A further option is to use the emission of discharges, containing the same species as in the plasma under investigation,

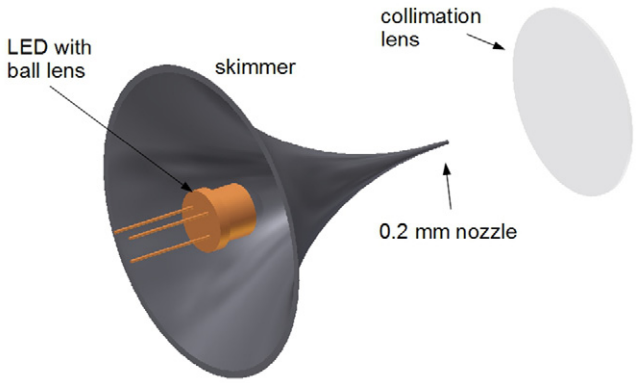

Figure 1. Skimmer and lens setup for collimation of a Broad band LED (©2013 Reprinted by permission of Wiley, Inc from [77]).

as light sources. One main issue in resonance absorption spectroscopy is the fact that the Beer–Lambert law (equation (4)) cannot be straightforwardly applied to determine the density of absorbing species. Let us consider the case where a lamp is used as the light source emitting radiation from transitions of the same atomic species under investigation in the plasma. Furthermore, both the emission from the lamp and the absorption in the plasma are assumed to have Gaussian profiles. The resultant transmitted spectral profile shows a dip in the centre of the profile which increases with increasing absorber density. Mitchell and Zemansky have published an extensive work on the theory behind resonance absorption spectroscopy and how to analyse the data [79]. Here, a brief formulism on how to determine the density for the considered case is given [80]. The emission spectral profile of the lamp is expressed by

$$I(\lambda) = I_0 \frac{2\sqrt{\ln 2}}{\Delta\lambda_{De}\sqrt{\pi}} \mathrm{Exp}\left[\frac{-4\ln 2(\lambda-\lambda_0)^2}{\Delta\lambda_{De}^2}\right], \tag{34}$$

and the absorption spectral profile by

$$k(\lambda) = k_0 \frac{2\sqrt{\ln 2}}{\Delta\lambda_{Da}\sqrt{\pi}} \mathrm{Exp}\left[\frac{-4\ln 2(\lambda-\lambda_0)^2}{\Delta\lambda_{Da}^2}\right]. \tag{35}$$

The Doppler widths of the emission spectral profile $\Delta\lambda_{De}^2$ and the absorption spectral profile, λ_{Da}^2, are calculated using equation (21) and it is assumed that

$$k_0 \propto f[N_a], \tag{36}$$

where f is the oscillator strength and N_a the absorbing atoms density.

The intensity of the transmitted light through the plasma with absorption length L is expressed as

$$I^T = \int I(\lambda)\mathrm{Exp}(-Lk(\lambda))\mathrm{d}\lambda. \tag{37}$$

The absorption rate, A_L, is described by

$$A_\mathrm{L} = 1 - \frac{I^T}{I_0}\sum_{m=1}^{\infty}\frac{(-1)^{m+1}}{m!}\frac{(k_0L)^m}{\sqrt{1+m\alpha^2}} \tag{38}$$

where $\alpha^2 = T_\mathrm{e}/T_\mathrm{a}$ with T_e being the temperature of the emitter and T_a of the absorbing medium. When f, L and α are known, the absorbing atoms density, N_a, can be deduced from a measurement of A_L. Note that the above relation only applies to a single line with Doppler line profiles. A modified Mitchell and Zemansky theory has been recently used for the study of atmospheric pressure plasmas [81, 82].

2.6.4. Improving signal-to-noise ratio. As mentioned above, one possibility to increase the sensitivity of an absorption technique is noise reduction. The contributions to the signal baseline noise, which limit the minimum detectable absorption, have a variety of sources in an absorption spectroscopy experiment (e.g. electrical, mechanical, optical…). In every absorption experiment, the detector itself has a signal-independent intrinsic level of noise associated with the light-generated charge carriers within a photodetector. The major two are known as *shot noise* and *white noise*. The former is also called quantum noise, due to shot noise that arises from the discrete nature of detection events; in this case, the incidence of photons on the detector, and the fluctuations within these event occurrences. The latter is associated with the Johnson–Nyquist power noise arising from thermal perturbations of the electrons within the detection system [83]. As white noise is random, averaging can minimize its influence in the measurements. In practice, the sensitivity limits imposed by these sources of noise are typically of the order of absorptions within the 10^{-2}–10^{-3} range (down to 10^{-5} levels may be achieved adopting a dual-balanced detection scheme), since other sources contribute to the overall noise level. Generally, these contributions fall under the category of $1/f$ *noise* or *pink noise*, so called because its contribution at dc can be orders of magnitude higher than in the high frequency (>kHz) regime. Its physical origins are still unclear, but may include thermal, mechanical, and acoustic fluctuations to which the experiment is exposed, as well as phase and amplitude noise associated with the laser itself. These noise levels are not necessarily the limiting factor in an experiment, and can be greatly reduced by moving detection to a higher frequency regime by using modulation techniques based on phase sensitive detection, as these noise levels tend to decrease with $1/f$ [84]. But besides the detector noise sources, other contributions from a laser absorption based setup need to be considered. Noise sources outside the detection system can include, for example, power fluctuations in the laser, or etalons formed between reflective surfaces that can all introduce variations in the baseline that interfere with the absorption information. Moreover, this kind of noise sources is more difficult to control. If fractions of absorption on the order of 10^{-2}–10^{-3} are typically measurable by direct absorption, using modulation techniques, fractions of absorption on the order of 10^{-5}–10^{-6} are generally detectable [85, 86], with species detection limit in plasmas down to ppt range (see [86]). Very low species detection limits in plasma can be achieved by means of phase sensitive detection using modulation of laser intensity or wavelength, Stark or Zeeman effects, particle density (plasma) modulation. Except the laser modulation techniques, the other methods can change the plasma characteristics. Thus, they are inappropriate for plasma diagnostic if we wish a non-intrusive

approach. Plasma modulation may be a solution for atmospheric pressure pulsed discharges and for species having short lifetimes. Here, the principle of laser wavelength modulation is described [84, 86, 87], above-mentioned techniques having a similar principle. The laser wavelength is modulated before being transmitted through the absorbing plasmas. For instance, in case of diode lasers, this is done by using a function generator (e.g. the internal function generator of a lock-in device) by applying a sine signal of small amplitude at a frequency in the kHz range on top of a low frequency laser tuning over the transition of interest, which slightly changes the current through the diode laser device. As a result, the wavelength of the laser is then modulated. A reference signal is given to a lock-in amplifier. The laser light transmitted through the plasma is then converted into a photocurrent by a photodiode and is analysed at the modulated frequency or at higher harmonics using a lock-in system. The lock-in amplifies the modulated absorption signal, multiplies it by the lock-in reference signal and integrates the product over a time much longer than the period of the modulation signal using a phase sensitive detector. Because of the orthogonality of the sinusoidal functions, the contribution of any signals that is not at the same frequency is attenuated to zero. Therefore, noise signals at any other frequency are cancelled out. The lock-in needs to lock the phase difference between the two signals and to adjust it to zero in order to maximize the absorption signal. If the laser wavelength is sinusoidally modulated at frequency ω, such that $\nu(t) = \nu_L + a\sin(\omega t)$, and is tuned over a weak absorption line (i.e. $I(\nu) \approx I_0(1 - k(\nu)l_{abs})$), it can be shown by Taylor development that the absorption fraction is [88]:

$$\frac{I(\nu) - I(\nu_L)}{I_0} = -al_{abs}\left\{\begin{array}{l}\left[\frac{a}{4}\frac{d^2k}{d\nu^2}(\nu_L) + ...\right] + \left[\frac{dk}{d\nu}(\nu_L) + ...\right]\sin(\omega t) \\ \quad + \left[-\frac{a}{4}\frac{d^2k}{d\nu^2}(\nu_L) + ...\right]\cos(2\omega t) \\ \quad\quad + \left[-\frac{a^2}{24}\frac{d^3k}{d\nu^3}(\nu_L) + ...\right]\sin(3\omega t) + ...\end{array}\right\} \quad (39)$$

For sufficiently small modulation amplitude, $a << \nu_L$, the first terms in each squared bracket are much larger than the terms that follows. Thus, behind the lock-in amplifier, the signal amplitudes in first, second and third harmonics are proportional to first, second and third derivatives of the absorption coefficient, respectively. For plasma sensing, the even harmonics are of most interest, because they have non-zero values at the line center. For Lorentzian profiles (which are typical absorption coefficients in atmospheric pressures plasmas), higher harmonics give in principle smaller signals. If signals are normalized to the 2nd harmonic, then we have at line center a signal of 53% in 4-th harmonic, 36% in 6-th harmonic and 27% in 8-th harmonic, respectively [89]. However, even if the signal decreases in higher harmonics, if noise is dominated by etalon signals (or optical feedback) and not by absorption noise, then employing higher harmonics may be favourable [89–91]. The key instrument in the phase sensitive detection techniques is the lock-in amplifier. Nowadays, fast multichannel lock-in devices are commercially available with input bandwidth of up to 600 MHz, time constants down to 30 ns and dynamic reserve of 100 dB. The benefit inherent in transposing the detection band to an even higher (MHz) frequency regime is expected to further reduce the noise contribution, although this is not always found to be the case as an increase in the thermal noise, due to low power levels and high-bandwidth detectors, tends to become the limiting factor. These advanced characteristics are important, for instance, when using absorption with novel high repetition frequency lasers.

2.7. Techniques of spatial resolution

Absorption spectroscopy is in general a line-of-sight diagnostic technique. To achieve space-resolved densities [92] from the line-of-sight integrated densities, without inserting a probe into the plasma, several approaches are possible [93]. *Tomography* is the most precise method to achieve spatial resolution by multiple angle measurements although it requires very high experimental effort. It has been applied to turbulent flames, e.g. by Samoro *et al* [94]. With this technique, projections of the density profiles are taken at different angles. From these measurements, a reconstruction of the 2D-profile can be achieved. The advantage is that arbitrary profiles can be studied and no previous assumption on symmetries needs to be made. An estimate of the space resolved ground state density can be derived by the following tomographical approximation. From two transversal scans of the plasma, the local density in the section plane can be determined with trade-offs in accuracy via [95, 96]:

$$n(x,y) \approx \frac{\int n\mathrm{d}x \int n\mathrm{d}y}{\iint n\mathrm{d}x\mathrm{d}y}. \quad (40)$$

In [95, 96], a rectangular shaped jet was investigate regarding its ozone density distribution (see section 3.3.1).

Under the simplifying assumption that the profile is axisymmetric, several other techniques can be applied. Most commonly used techniques are firstly Abel inversion, secondly onion peeling and thirdly Fourier deconvolution. In *onion peeling*, the investigated plasma is sectioned into concentric rings. Firstly, the line-of-sight outer most regions representing the outer ring density is measured and subtracted from the remaining densities. Subsequently, the next ring is analysed. This process is repeated yielding the complete density distribution. Disadvantage of this method is that small errors at the outer edge accumulate to larger errors towards the centre. Probably the most commonly used method to gain density distributions from line-of-sight measurements is *Abel inversion*, which leads to a line-of-sight density as a function of radius [97, 98]. It has been applied in many different

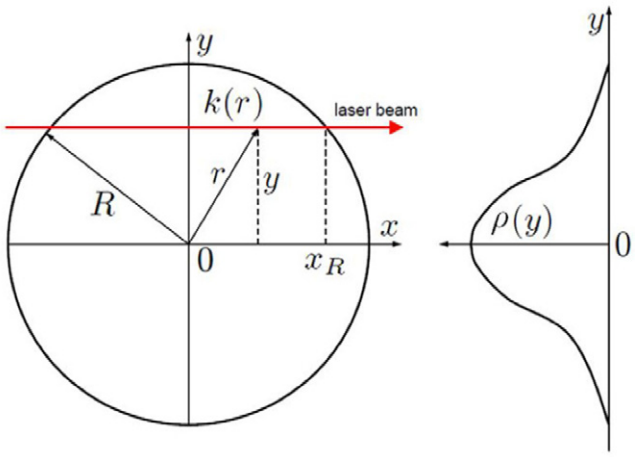

Figure 2. Illustration of the relation between spatial absorption coefficient distribution $k(r)$ and line-of-sight optical depth $\tau(y)$ [99] (© IOP Publishing. Reproduced with permission. All rights reserved).

atmospheric pressure discharges for absorption spectroscopy. The Abel integral is given by:

$$\tau(y,z,t,\nu_0) = 2\int_r^R k(r,z,t,\nu_0)\frac{r\mathrm{d}y}{\sqrt{r^2-y^2}} \qquad (41a)$$

with τ the optical depth, k the absorption coefficient at the position y, and r and z the radial and axial coordinates. R is the distance at which the absorber density has decreased to zero (see figure 2).

Assuming that the gradient for τ is higher than $1/r$, for an axisymmetric absorber distribution, the inverse Abel transform is given by equation (41*b*) and thus, from the optical depth τ, the absorption coefficient can be calculated (see e.g. [99]) as:

$$k(r,z,t,\nu_0) = -\frac{1}{\pi}\int_r^R \frac{\partial\tau(y,z,t,\nu_0)}{\partial y}\frac{\mathrm{d}y}{\sqrt{r^2-y^2}} \qquad (41b)$$

As the inversion process is highly sensitive to noise, usually the measured data is fitted using e.g. two Gaussian profiles and the derivative of the optical depth profile is performed on the fitted data. Abel inversion is a versatile tool, which has been applied in many studies of atmospheric plasma jets [60, 100, 101] e.g. in [18]. N_2(A) Metastables were detected in cavity ring down spectroscopy (CRDS), in [99], metastable helium atoms are studied. If a used a fitting procedure of an analytical density profile to the Abel transformation is used, complex profiles can be analyzed [101]. A simplified version of Abel transformation is the line integration method [102, 103]. A direct spatial resolution can be achieved by performing two measurements simultaneously with two light beams crossing each other perpendicularly. One example for this is the double beam modulated linear absorption technique described by Moskowitz [104]. Here, a modulated pump laser beam of high intensity is used to saturate the transition and thus deplete the investigated state. A split beam of the same laser but with significantly less intensity is used as probe beam at an angle of 90°. By a pulsed modulation of the saturating beam, a modulated absorption of the probe beam can be detected yielding a signal proportional to the state density.

2.8. Techniques and limits of time resolution

Absorption techniques can probe time-resolved species densities and temperatures when plasmas exhibit temporal behaviour. This can be done in two ways, either using a pulsed light source while the detector is constantly recording, or using a dc light source while gating the detector. From the UV to MIR, commercially available lasers such as Nd:Yag, dye and semiconductor lasers, are commonly pulsed in the ns-time domain. At present, new ultrafast picosecond and femtosecond lasers with tuning possibilities in the UV to NIR range are available at repetition frequencies of tens of kHz (used mainly for LIF and CARS experiments). Concerning detection systems, fast response time detectors and high bandwidth amplifiers are needed. UV to NIR ICCD cameras are now available with gate widths below 0.5 ns. In MIR, photo-detectors with ns response time are also accessible. Even faster detectors such as streak cameras are commercially available. However, time-resolved absorption spectroscopy is often limited by the reduced sensitivity. Enhanced detection is done not by measurements of the fraction of absorption but by the induced fluorescence light. From a spectral point of view, time-resolved absorption measurements are performed in different ways. Lasers are tuned either very fast (much faster than the species characteristics time) over the entire absorption feature, which is then recorded with a given time-step (e.g. [105]), or by simultaneous or sequential measurements at two wavelengths, (first at the absorption peak and then off-resonance) or at several wavelength over the absorption profile (e.g. [106]). In the first case, broadening changes in time may be recorded, and, therefore, the method is more appropriate. If the plasma is periodically changing, then average techniques can be used to improve the signal-to-noise ratio. High frequency lasers are of interest for noise reduction in repetitive discharges, but also for a single plasma event with a time scale longer than the inverse of the laser pulse frequency

3. Absorption spectroscopy for jet-like atmospheric pressure plasmas

Chapter 3 introduces work performed to date on the topic of absorption spectroscopy on atmospheric plasmas. Here, cold atmospheric plasma jets applicable in the field of plasma medicine form the focus. The chapter is sectioned according to wavelength from VUV to MIR, and the main techniques are discussed and examples are given. Where necessary or helpful, other plasma sources including low pressure plasmas are covered to present special techniques or interesting approaches or highlight an experiment that could be also transferred to the diagnostics of plasma jets.

3.1. Typical setups of absorption spectroscopy

Absorption spectroscopy is one of the simplest techniques to measure absolute densities. A simple setup consists of a

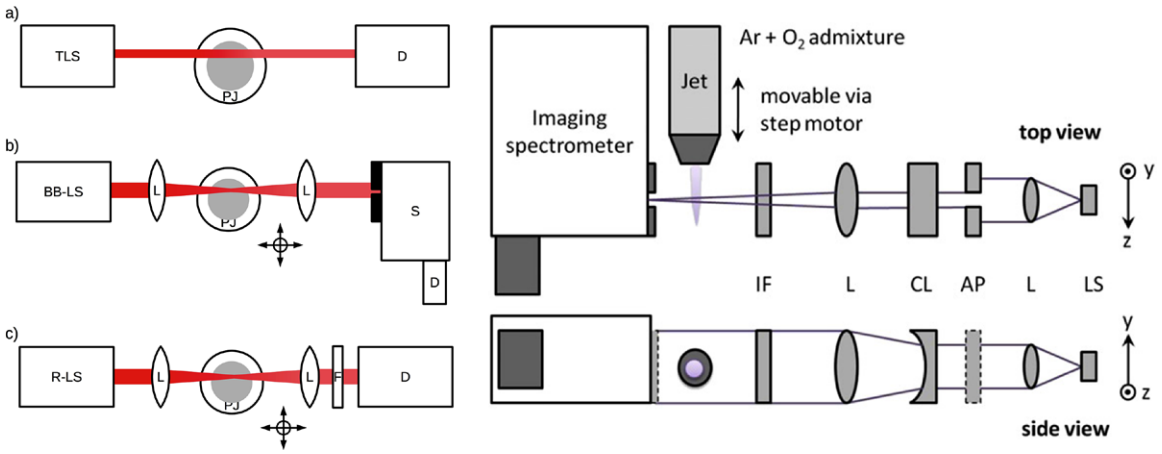

Figure 3. Left: (a) simple absorption setup: wavelength tunable light source (TLS), plasma jet (PJ) and detector (D); (b) broad band light source (BB-LS), focussing optics (L) and spectrograph (S) with detector (D); (c) resonant light source (R-LS), focusing optics (L) and filter (F); right: single measurement radial profile ozone absorption measurement setup: LS: UV-light source, L: lens, AP: aperture, CL: cylindrical lens, IF: interference filter [60] (© IOP Publishing. Reproduced with permission. All rights reserved).

monochromatic light source, an absorber (the plasma jet) and a detector (see figure 3(a)). The setup can be made more versatile by using a broadband light source and a spectrograph (see figure 3(b)). With this setup, the probed transition can be selected and absorption profiles can be measured. From the absorption profile, absolute densities can be gained. Instead of the broadband light source, a tuneable light source can be used, reducing the need for a spectrograph (see figure 3(c)). When a laser is used as light source, the plasma background radiation can be reduced to a minimum by using the appropriate filters and the accuracy can be improved.

In some studies, the investigated jet is placed inside an enclosed chamber to control the gas atmosphere surrounding the plasma jet. Here, it has to be considered that the flow conditions will most probably be different than in open-air operation. This can for example be done by comparing measurements in the chamber and in open atmosphere (see e.g. [95] for ozone absorption).

To use the advantage of measuring a complete radial profile of a plasma jet in a single measurement, an imaging detection system can be used. Combined with a spectrograph, both wavelength selection and parallel data recording can be achieved. Usually, the plasma is installed on a stepping motor stage to allow space-resolved, or for the case of the imaging optics axially resolved measurements. In radially symmetric cases, Abel inversion can be performed to gain space-resolved densities. If the precise wavelength of the light source is not known, such as, e.g. for tuneable diode laser spectroscopy (TDLAS), reference measurements have to be performed.

The typical apparatus used for measuring the spatial and temporal density of rare gas metastables by TDLAS is shown schematically in figure 4. To protect the diode from back-reflections an optical isolator is used. The laser beam is attenuated (to avoid saturation of the photodiodes (PD) and of the probed transition in the plasma) using neutral filters, and subsequently split into three branches by two beam splitters (BS). All three laser beams are detected by photo diodes and the signals are recorded with an oscilloscope. A shutter could be used to record separately the plasma emission and absorption

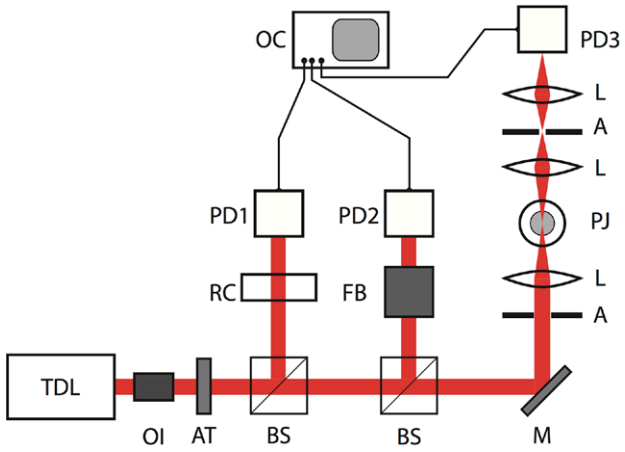

Figure 4. Typical setup used for TDLAS. TDL: Tuneable Diode Laser, OI: Optical Isolator, AT: Attenuator, BS: Beam Splitter, M: Mirror, A: Aperture, L: Lens, PJ: Plasma Jet, PD: Photo Detector (PD3: fast PD), RC: (low-pressure) Reference Cell, FB: Fabry–Perot interferometer, OC: Oscilloscope.

signals. The first beam passes through an absorption cell filled with a reference gas (usually of the probed species) for spectral identification. The second beam passes through a Fabry–Perot interferometer. This branch allows to convert the relative spectra x-axis in wavelength units and to ensure the single-mode operation of the laser, i.e. that the frequency scanning is performed continuously without jumping between different modes of the laser resulting in frequency discontinuities. This jumping is called mode hopping. During the measurements of the spectral profiles, the laser frequency is scanned over a larger spectral range than that FWHM of the studied absorption line. In this way, a reference line profile is thus obtained and this branch is used to tune the laser frequency exactly to the maximum value of the absorption line profile corresponding to the central wavelength of the absorption line. The laser frequency can then be tuned precisely over the spectral profile of interest by varying the current and temperature of the laser diode. Finally, the third beam passes the plasma jet, and, from its fraction of absorption, the density of metastable

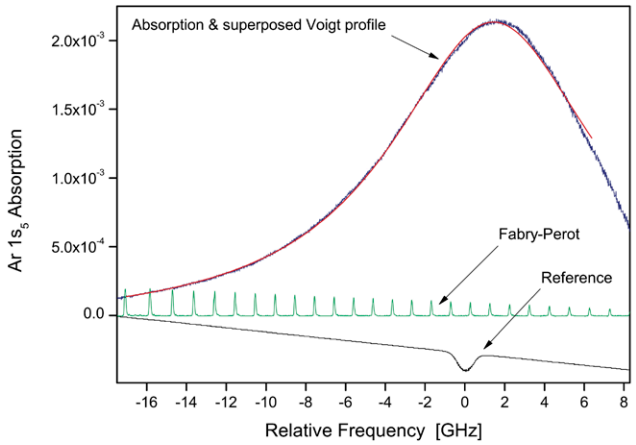

Figure 5. Pressure broadened absorption line profile of the Ar* $1s_5 \rightarrow 2p_9$ transition (blue). Also shown are the transmission peaks of the Fabry–Perot interferometer (green), the absorption signal from a low pressure reference discharge (black) and the Voigt fit on the profile (red). Measurements have been taken while operating a planar RF driven APPJ at 2 slm He flow with 5% Ar admixture and a power level slightly below the arcing threshold. The horizontal axis scale shows the frequency distance of the spectral features. From [107] (With kind permission from Springer Science and Business Media).

atoms is obtained. For time-resolved measurements, the photodiode detector should have a fast time response (preferably ns) since the lifetimes of He and Ar metastable states are of few μs under typical experimental conditions. For probing the lowest metastable states of Ar, Si photodiodes and for He, InGaAs photodiodes are recommended.

Figures 5 and 6 show typical time-averaged absorption spectral profiles of the Ar (811.5 nm) and He (1083 nm) lines obtained from a planar RF (13.56 MHz) driven APP jet and a co-axial RF (1 MHz) driven APP jet, respectively. Other examples can be found in [107–111] for Ar and in [99, 107, 112–114] for He. Note that as the upper level 2^3P of the He $2^3S_1 \rightarrow 2^3P_{0,1,2}$ transition consists of 3 sub-levels with $J = 0$, 1, 2, the spectral absorption profile has three components. While at low pressure this fine structure can be easily seen (see figure 6(a) for the case of the low pressure reference discharge), at atmospheric pressure, the $J = 1$, 2 components are mixed and not distinguishable due to pressure broadening of the lines (see figure 6(b) for the case of the atmospheric plasma jet). However, the $J = 0$ component is still distinctly observable even at atmospheric pressure. In order to determine the absorption coefficient, all absorption spectral lines should be fitted with Voigt profiles. For the case of helium, the absorption spectral profile should be represented by the superposition of two Voigt profiles, each for one fine-structure component, with a separation of 2.3 GHz and an intensity ratio of 5 to 3, according to their statistical weights. The Gaussian component of the absorption profiles, resulting from Doppler broadening, can be calculated from the value of the gas temperature, determined separately. The Lorentzian component should be varied until the calculated absorption profile fits the measured line.

As information about the Lorentzian and Gaussian part of an absorption line is best distinguished by the wings of the

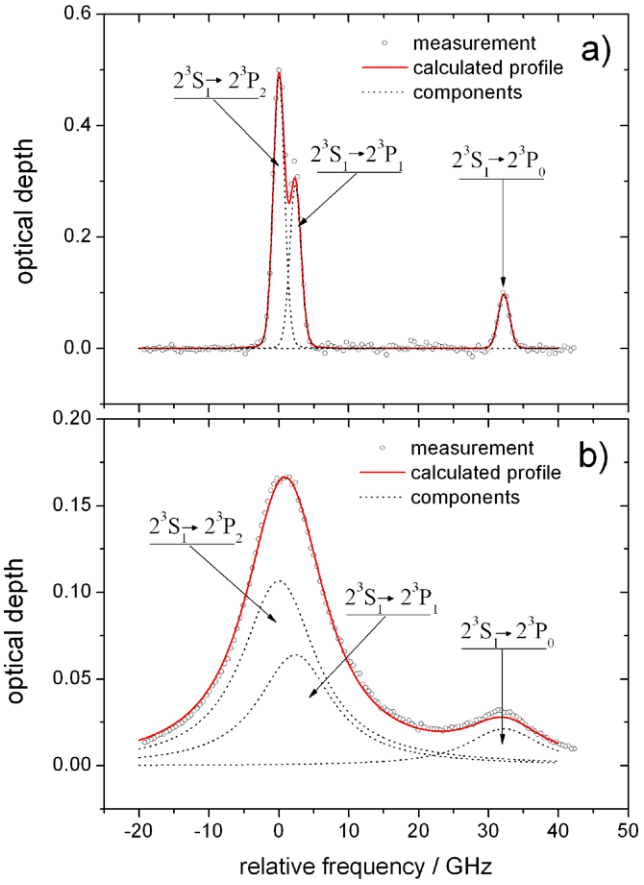

Figure 6. Time-averaged spectral absorption profile for (a) the low pressure He discharge lamp and (b) the kinpen Sci (atmospheric pressure, $y0 = 0$ mm, $z0 = 0.1$ mm). The solid curve is the superposition of the calculated absorption profiles for the three fine structure components (dashed lines). The zero point of the relative frequency axis refers to the peak position of the $2^3S_1 \rightarrow 2^3P_2$ component. From [99] (© IOP Publishing. Reproduced with permission. All rights reserved).

absorption line, it is important to scan over the line to the point where the absorption is zero. As most diode laser mode hop free tuning range is smaller than the absorption of a broadened line at atmospheric pressure, most scans are taken with the line maximum not in the centre of the tuning range. A different approach has been proposed by Bösel *et al* [115–117]. Using intracavity acousto-optic modulators, the wavelength of a Littrow type diode laser system is tuned mode-hop-free. The external resonator modes and the grating selectivity are independently and electrically alterable by two AOMs. Thus, a tuning of the external resonator over up to 1900 GHz is possible [116]. A precise computer control of laser diode and AOMs allowed a single-mode tuning of the whole laser with a tuning range of 225 GHz in 250 s. Additionally, a fast tuning over 90 GHz in 190 μs and a repetition rate of 2.5 kHz were demonstrated. The application was shown at higher pressure in a Hydrogen discharge [118].

3.2. VUV absorption spectroscopy

A lot of species relevant for cold atmospheric plasma jets absorb in the VUV-spectral region. Especially, atomic

species exhibit absorption features in that regime. However, VUV absorption spectroscopy at ambient conditions has the drawback that the VUV radiation is strongly absorbed due to the high absorption coefficients of humid air species in this spectral range. Plasma jets studied with VUV radiation are usually placed inside a vacuum vessel to control the ambient gas. Furthermore, light sources in this spectral range are scarce (see section 2.6.3). VUV absorption spectroscopy has been applied in monitoring and studying of depositing low-pressure plasmas (see e.g. [76]) and has been proven to be a suitable technique to diagnose the main reactive species in oxygen discharges [119]. Nevertheless, there are several examples, where atmospheric plasma jets are studied with VUV absorption spectroscopy, as described in the following.

3.2.1. Singlet delta oxygen: $O_2(a^1\Delta_g)$. Being one of the most reactive species among the ROS, singlet delta oxygen ($O_2(a^1\Delta_g)$), the first electronically excited low-energy state of O_2, has attracted the attention of many scientists working in almost every field of natural sciences, from physics to medicine, through chemistry and biology. $O_2(a^1\Delta_g)$ most remarkable feature is its extremely long and unique radiative lifetime of more than 75 min in the gas phase [120]. $O_2(a^1\Delta_g)$ is very resistant against homogeneous and heterogeneous relaxation processes [120] and can thus transport its energy far away from its place of production. This energy donor is useful for a large spectrum of applications, including removal of air pollutants [121], degradation of synthetic polymers [122], combustion [123], laser excitation [124], and biomedicine [125]. However, $O_2(a^1\Delta_g)$ is difficult to produce efficiently and detect accurately. A topical review concerning the production of $O_2(a^1\Delta_g)$ in low-temperature plasmas in various types of electric discharges and its detection by a variety of different experimental methods can be found in [126]. Although challenging, there are many different approaches for detecting $O_2(a^1\Delta_g)$, taking advantage of its specific chemical, spectroscopic and magnetic properties (e.g. [119, 126]): infrared emission spectroscopy, vacuum absorption spectroscopy, calorimetry, electron paramagnetic resonance, photoionization, Raman spectroscopy, intracavity laser spectroscopy, ring-down spectroscopy, and cavity-enhanced absorption spectroscopy. Each of these techniques has its own advantages and disadvantages, in terms of simplicity, sensitivity, selectivity, reliability, accuracy, and cost. The presence of $O_2(a^1\Delta_g)$ can be detected by its infrared emission at 1.268 μm. This is commonly used for measuring $O_2(a^1\Delta_g)$ concentration. However, this emission is extremely weak, since the transition is strictly forbidden for electric dipole radiation, being only permitted for magnetic dipole radiation, with the Einstein coefficient being of the order of magnitude of 10^{-4} s^{-1}, equivalent to a radiative lifetime of approximately 4500 s [127]. Nevertheless, Sousa *et al* have successfully developed a very simple and online method for the accurate determination of $O_2(a^1\Delta_g)$ absolute density, based on the infrared emission of $O_2(a^1\Delta_g)$ at 1.27 μm [128]. This method has been used to determine the $O_2(a^1\Delta_g)$ absolute concentration in the effluent of a single [129] or multiple micro-cathode sustained discharges (MCSD) [130], as well as in two pulsed kHz-driven APPJs with different geometries [131, 132], in the effluent of an ac MHz driven APPJ [133], and two geometrically different RF-driven APPJs [132, 133]. Even though this concentration measurement technique based on the infrared emission of $O_2(a^1\Delta_g)$ is simple to implement, it yields no spatial resolution and the measurements can only be performed in the effluent within a sampling detection cell and not in the main discharge region. Additionally, to obtain absolute concentrations from emission measurements, some prior assumptions concerning the spatial distribution of $O_2(a^1\Delta_g)$ in the sampling cell and estimations regarding the probability of a photon emitted within the detection cell reaching the detector have to be made.

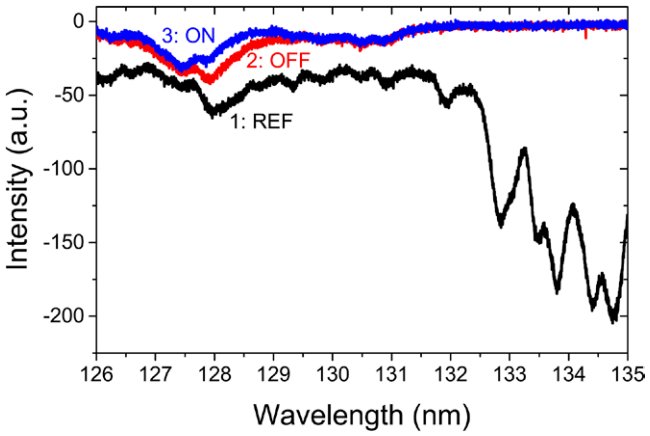

Figure 7. Typical VUV spectra: black curve 1: reference spectrum of a VUV H_2 source [119] (no absorption); red curve 2: transmitted spectrum of an Ar/O_2 mixture (9 slm of Ar with 1% of O_2) at a total pressure of 145 mbar (plasma OFF); blue curve 3: transmitted spectrum while operating at the experimental conditions of curve 2 an array of 4 MCSDs [130] at an equal current per discharge of 5 mA. From [128] (© IOP Publishing. Reproduced with permission. All rights reserved).

A more accurate and reliable method for measuring the $O_2(a^1\Delta_g)$ absolute density is based on VUV absorption by $O_2(a^1\Delta_g)$ molecules. In fact, $O_2(a^1\Delta_g)$ largely contributes to the light absorption between 125 and 130 nm in the atmosphere, as well as in cold atmospheric plasmas [119]. At 128.5 nm, the absorption cross-section of $O_2(a^1\Delta_g)$, σ_a = 167 × 10^{-19} cm^2, is 40 times larger than that of the ground state, $O_2(X^3\Sigma_g^-)$, σ_X = 4 × 10^{-19} cm^2 [134]. The absolute density of $O_2(a^1\Delta_g)$ can thus easily be deduced using equation (12). As the contribution of $O_2(a^1\Delta_g)$ to light absorption is negligible for wavelengths above 130 nm but lower than 140 nm, the VUV absorption method can also provide the absolute density of the ground state molecules, $O_2(X^3\Sigma_g^-)$ [135]. Hence, the $O_2(a^1\Delta_g)$ production yield can be directly measured by this method without any assumption about the value of the gas temperature. Figure 7 shows typical measured VUV transmission spectra. The difference between curves 2 and 3 is due to absorption by $O_2(a^1\Delta_g)$. For more details on these data see [128]. Furthermore, the VUV radiation at 144.1 nm and 148.7 nm [136], wavelengths for which the cross sections are well known, can also be used for absolute $O_2(a^1\Delta_g)$ density determination by VUV absorption

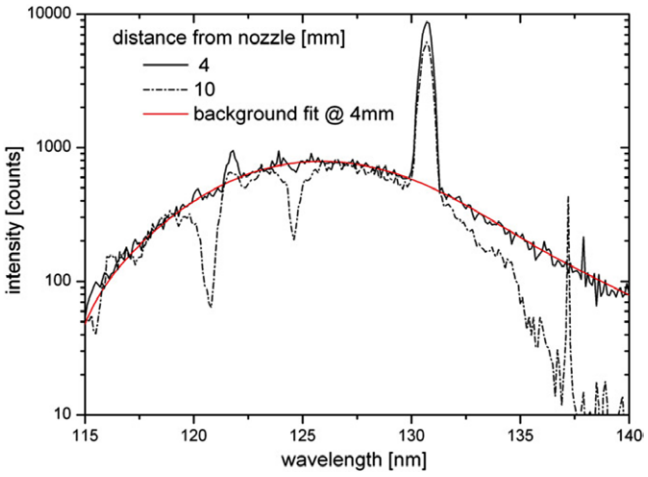

Figure 8. Argon excimer emission from a kinpen with absorption features originating from molecular oxygen [135] (© IOP Publishing. Reproduced with permission. All rights reserved).

spectroscopy. VUV absorption spectroscopy is thus a versatile technique well suited to detect singlet delta oxygen species.

3.2.2. O_2-molecules. For VUV absorption spectroscopy, very often plasmas are used to generate this radiation. Therefore, a majority of plasma VUV absorption measurements are resonant absorption spectroscopy measurements. The energy of the VUV photons is high, so that the non-invasiveness claimed for the technique cannot always be guaranteed, since pre-ionization by VUV photons can influence the breakdown of discharges, as shown in the case of surface spark discharges [137]. In [138], resonant absorption of VUV radiation was used to detect oxygen (see also [139]), nitrogen and hydrogen atoms. Quantification of absorption cross-sections is relatively easy by comparing the results to titration experiments, for example, of oxygen atoms with NO [67]. Titration as an alternative to absorption spectroscopy has also been applied to atmospheric plasma jets [140, 141]. Moravej *et al* used a titration method in combination with infrared absorption to measure the atomic oxygen density in an rf plasma jet [141]. O-atoms were titrated with NO and the resulting NO_2 was determined in an absorption cell by IR-absorption spectroscopy.

VUV radiation generated by plasma jets can reach long distances from the plasma jet nozzle. In a planar APPJ, VUV radiation was detected up to 10 cm distance from the nozzle while operated in ambient conditions [6]. It could be shown that this VUV radiation contributes significantly to the atomic oxygen generation in the jet effluent [95]. As a result, absorption by atmospheric oxygen could be observed in spectra at even greater distances [142]. The absorption of jet generated argon excimer radiation was utilized in [135] to determine the molecular oxygen diffusing from the surrounding air in the effluent of an argon plasma jet. Figure 8 shows the excimer continuum of the discharge measured end-on at 4 mm and at 10 mm distance to the spectrometer window. The absorption by this oxygen diffusing into the jet effluent can be clearly seen at 10 mm distance. The solid line is the fitted background used to calculate the absorption. With the help of a novel analytical approximation solution of the convection-diffusion-equation for near field fluid jets [143], molecular oxygen on axis absolute densities were evaluated.

3.2.3. O and N atoms. For light atoms, the transitions of the ground state to the first excited state are of high energy and require VUV photons. While lasers can be employed as VUV source, e.g. by Anti-stokes Raman scattering [69], often, these photons are generated by discharges using the same type of gas as the studied plasma. These discharges emit resonant photons for the desired transition. As shown above, photons from the studied discharge itself can be used. This self absorption usually also resonant can be used to detect e.g. metastable argon ions [144]. A thorough scientific work comparing resonant self-absorption with laser absorption on argon metastables is presented in [145]. Resonant absorption has been used for detection of oxygen (ground state and metastable) or nitrogen atoms in low-pressure plasmas (see e.g. [73, 75, 146]). Iseki *et al* also used an enclosed vessel at controlled conditions (argon atmosphere) and studied the ground state atomic oxygen densities with resonant absorption spectroscopy. The oxygen density correlated to the D-value of spore inactivation at D-values around 10 [147]. Jia *et al* deduced the absorption length for the O-densities measured by VUV absorption from TALIF measurements [148]. The oxygen densities measured with the same setup by Takeda *et al* [149] were in the order of 10^{14} to 10^{15} cm^3. These are the expected values for argon discharges with molecular admixture as determined by TALIF measurements [135, 150].

Recently an unusual approach to determine absolute atomic densities in an atmospheric plasma jet was performed using the continuum synchrotron radiation at the VUV beamline at the SOLEIL synchrotron facility [151]. With an all-reflective Fourier-Transform spectrometer, and the beam-line, a $\lambda/\Delta\lambda$ of 10^6 could be achieved at an instrumental resolution of 0.87 cm^{-1}. This resolution is high enough to resolve the atomic oxygen triplet (see figure 9).

To conclude, VUV absorption spectroscopy offers the possibility to diagnose a variety of different reactive species generated by atmospheric plasma jets. Even light atoms can be absolutely characterized without intricate calibration procedures. The high absorption of VUV radiation in ambient conditions, however, make measurement setups complex and sometimes requires the operation of the plasma jets in an artificial environment, which makes it difficult to transfer the results to real *in situ* situations.

3.3. UV absorption spectroscopy

In the UV-spectral range, many molecular species have high absorption cross-sections—usually several orders of magnitude higher than in the infrared spectral range. This makes UV absorption spectroscopy a relatively sensitive method for species detection. However, the spectral overlap between the species is drastic and measures have to be taken to avoid misinterpretation or over-estimation of species densities. Figure 10 shows absorption cross-sections for 6 different species relevant in many applications of cold plasma jets. The

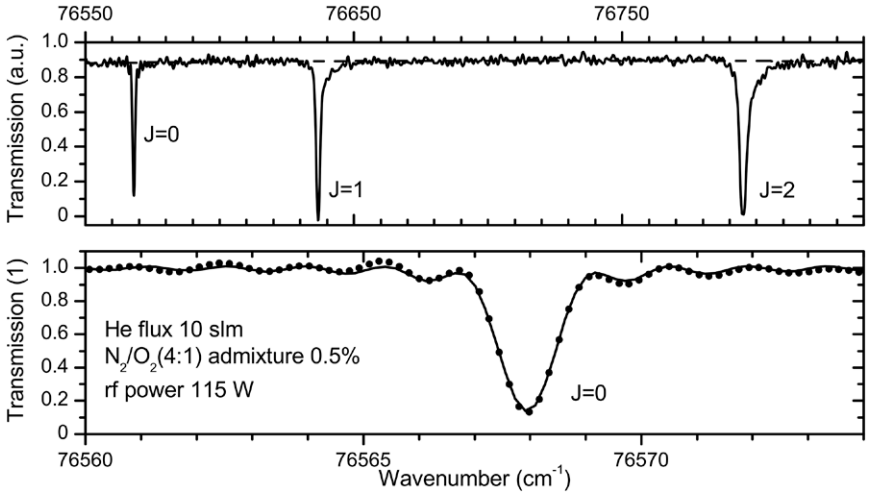

Figure 9. Resolved atomic oxygen triplet measured in a jet like setup by VUV continuum synchrotron radiation absorption. In this setup the plasma source had to be adapted to be operated in ultrahigh vacuum conditions required for the synchrotron beam-line. Reprinted with permission from [151]. Copyright 2013 AIP Publishing LLC.

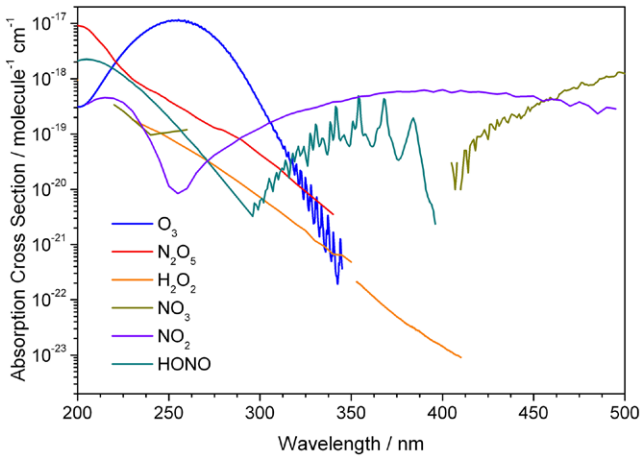

Figure 10. Absorption cross-sections of dominant species in humid air plasmas (Data taken from [53, 54].

data was taken from [53] and citations within the database. These are namely [152–154] for ozone [155, 156], for N_2O_5 [157, 158], for H_2O_2 [159], for NO_3 [160], for NO_2, and [161] for HONO.

In [162], the authors studied a broad gap DBD discharge for inactivation of microbes. For their absorption spectroscopic measurements, they took advantage of the fact that throughout the spectrum from 200 to 800 nm the domination in the absorption cross-section varies from species to species. In a similar figure to figure 10, the authors have pointed out that there are regions where UV absorption by certain species dominates that of the others. For example, while at 256 nm ozone absorbs one order of magnitude higher than other UV absorbing species, at 400 nm the absorption cross-section is several orders of magnitude higher for NO_2 than for other species. A deconvolution of the broadband absorption spectrum across all expected molecules yields total densities of a wide range of species. Observing the large overlap in figure 10, it is clear that this method has its limits and ultimately the advantage of high selectivity in the MIR spectral range has to be preferred (see chapter 3.4).

3.3.1. Ozone (O_3). One of the most studied species absorbing in the UV spectral range is ozone due to its large absorption cross-section around 250 nm and its dominant abundance in cold atmospheric oxygen containing plasmas. For example, with a deuterium lamp and a photomultiplier, a wire to plate streamer discharge was diagnosed for ozone in atmosphere surroundings [163]. Cold plasma jets have been studied by UV absorption spectroscopy almost since their first appearances in the late 1990s (see, e.g. [164, 165]). In [166], not only ozone but also O_2F was diagnosed in a parallel plate jet (APPJ) used for etching tantalum with CF_4 admixtures. Most easily, Hg lamps are used because of the dominant emission line at 254 nm at the central absorption wavelength of the Hartley bands. Since ozone has a long lifetime at ambient conditions, in [167], the ozone generation of a micro cathode sustained discharge sampled to an absorption cell 30 cm from the effluent was studied. The light source was a deuterium lamp and the absorption length was 50 cm. Due to the long absorption length, an accurate measurement of the absorbance profile was achieved (see figure 11).

Densities of O_3 in the range of 10^{12}–10^{16} cm^{-3} were measured and the limit of detection was 1.0×10^{12} cm^{-3}. The measured densities varied less than 10% over the time period of several months between measurements. Cross-sections for the ozone measurements were taken from [168]. In [169, 170], the distribution of ozone was measured in a pulsed corona discharge array. The 100 ns pulsed discharge was ignited in a 13 mm point to plane gap in dry air. The spatial resolution was 40 μm and the time resolution appeared to be better than 100 μs using a gated ICCD. As light source, a 2D expanded rectangular laser beam of a KrF Laser with low enough beam power density was used to avoid power saturation. An average over 10 discharge pulses was performed. With its high spatial, temporal and density resolution, this setup seems to be well suited for plasma jet diagnostics. In [96], the ozone density in

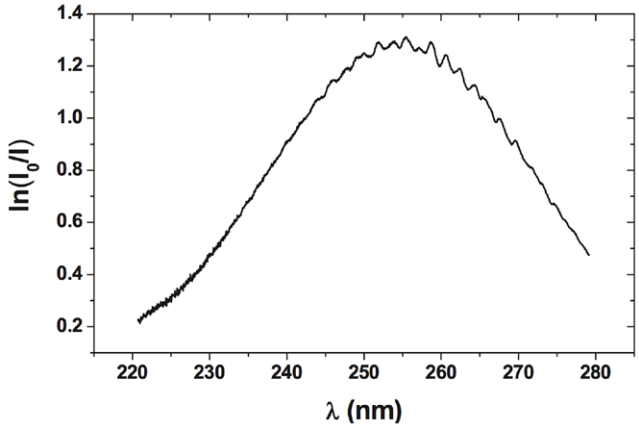

Figure 11. Evolution of the absorbance versus the wavelength in the range 220–270 nm. MCSD in a He/O_2 mixture, 1% of O_2 admixture from [167]. With kind permission of The European Physical Journal (EPJ).

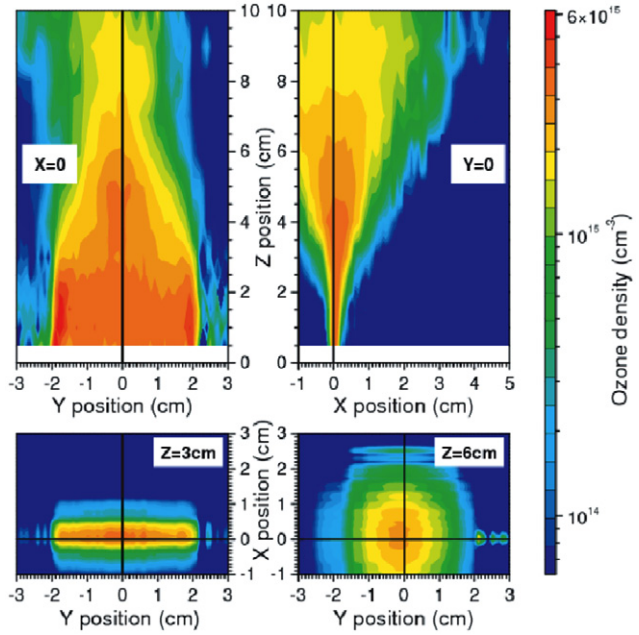

Figure 12. Ozone density in an Atmospheric Pressure Plasma Jet measured by UV absorption with an Hg-Lamp (©2007 Reprinted by permission of Wiley, Inc from [96].

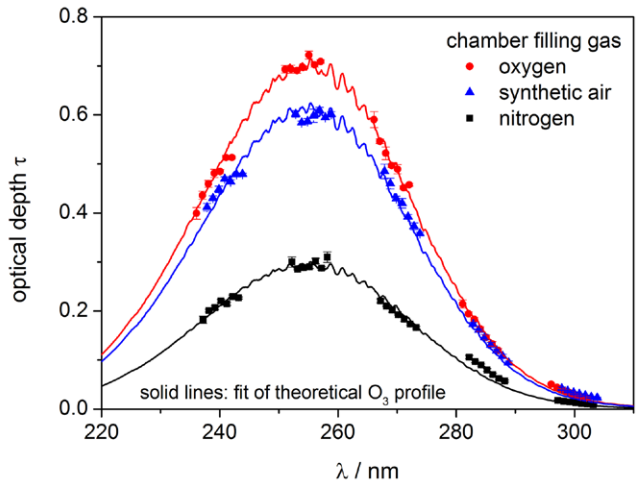

Figure 13. Ozone absorption in an artificial ambient surrounding (oxygen, synthetic air, nitrogen) compared to literature values [100] (© IOP Publishing. Reproduced with permission. All rights reserved).

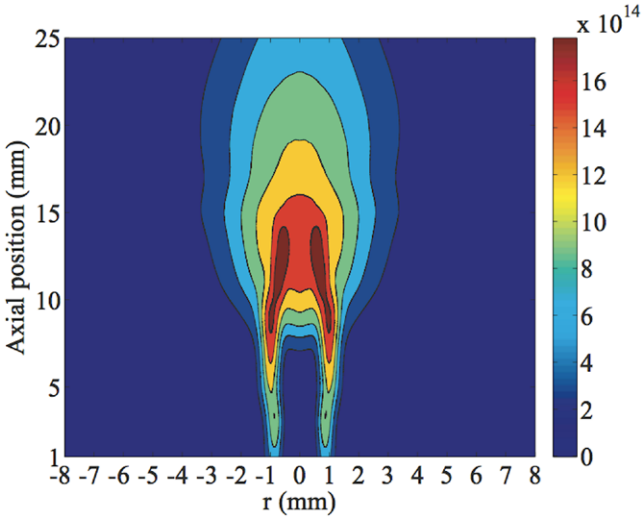

Figure 14. Ozone density map on an argon RF plasma jet [172] (© IOP Publishing. Reproduced with permission. All rights reserved).

a planar APPJ operated in helium was determined by a tomographic approach (see section 2.7). Figure 12 shows the ozone density in the effluent of a wide gap APPJ operated in helium with small oxygen admixtures. The density is derived from two transversal scans of the optical depth profile. Although artefacts of the simplified spatial resolution approach can be seen (see, e.g. z = 6 cm at x-position of 2.5 cm), the profile shows very important information such as the higher ozone production at the jets edges. Also the effluent shape can be seen and the spreading of the effluent, which is due to turbulence development in ambient air and is not present if the jet is blowing into a helium atmosphere [95].

In [60], an ozone density map of a MHz RF plasma jet (kinpen) was measured. By using an imaging spectrograph, a radial optical density profile was obtained in a single measurement. The density profile was derived by Abel-inversion. Here, the ozone density was not measured in the visible part of the plasma effluent, because the temperature profile deflected the beam. While this effect can be used for a temperature determination [101, 171], it changes the amount of light hitting the detector and thus influences the absorption measurements. However, to account for the problem of spectral overlap and variety of possible species produced, for a verification of the measurements, further studies were required. Therefore, in [100], a plasma jet was studied in different surrounding gas environments and the absorption was measured spectrally resolved with a spectrally selected light source to reduce photochemistry. The results from a comparison to the theoretical ozone absorption (see figure 13) revealed that the absorption signal was mainly originating from ozone.

In [172], a detailed ozone map of an argon/oxygen jet was measured (see figure 14). The interesting fact is that until a

distance of about 8 mm from the jet nozzle, the absorption profile exhibits a central dip, which is difficult to evaluate by Abel inversion. The authors used a fitting procedure of an analytical ozone profile to the Abel transformation according to [173], and included temperature corrections from Raleigh scattering.

In [174], ozone is determined in the effluent of a μAPPJ [27, 96] in combination with O-atom density measurements by TALIF spectroscopy. Especially the synergistic effects of O, O_3, and UV photons in polymer etching of a target are revealed in the study. Several investigations have tested UV absorption measurements of ozone to other diagnostic techniques—namely infrared absorption [60, 175] or molecular beam mass spectrometry [176]. Ozone is a suitable species to diagnose in cold plasma jets, not only because it is rather simple to measure it, but also because it gives an approximation for the order of magnitude of atomic oxygen production, which is the main source of ozone as others loss mechanisms are usually negligible [177, 178]. Furthermore, ozone plays a key role in plasma medicine and was initially thought to cure lung conditions when inhaled [11]. Studies have shown that in bacterial inactivation the bacterial log reduction correlates to the ozone production [179, 180]. Chapter VIII of [181] presents a collection of studies on the bactericidal mechanisms of ozone, as it has been used for water purification since the 1850s. Because the role of ozone in plasma medicine is still not clear due to its low solubility in watery liquids [182, 183] and its difficult detection in liquids, in addition to bacterial inactivation [184], many further studies on ozone initiated biological effects are and have to be performed, such as e.g. in lipid peroxidation [185], or in plasmid DNA interaction [186, 187]. Due to a multitude of reactive oxygen and nitrogen species in jet effluents including, e.g. $O(^1D)N_2$ excimer [186], a direct link is, however, intricate to make. As ozone is usually dominant in cold atmospheric plasma jets, UV absorption spectroscopy has proven very efficient in detecting this species under the conditions present in these jets. Due to the high absorption cross-section, sensitivity is high and spatially resolved maps can be measured and taken as reference for other measurements as for example for IR absorption spectroscopy.

3.3.2. Hydroxyl radical (OH). A molecule, which is of high relevance for medicine, is the hydroxyl radical, OH. Due to its high reactivity, it quickly forms new compounds and strongly interacts with biomolecules [181]. It is for example known to induce membrane lipid peroxidation [188, 189], which can explain plasma induced liposome modification as a model for plasma-membrane interaction [190]. It may also be responsible for lipid-A inactivation [185]. Furthermore, it plays a role in the innate immune system and the oxidative burst from macrophages [191, 192]. Not only due to its high reactivity, it is, however, much more difficult to detect by absorption spectroscopy than ozone. OH is readily used in emission spectroscopy [193] for the determination of the temperature of plasma species [24, 194] or as an indicator for humidity influences [175]. There are several works that detect OH in cold atmospheric plasma jets by LIF spectroscopy (see, e.g. [195–201]) inspired by the combustion community,

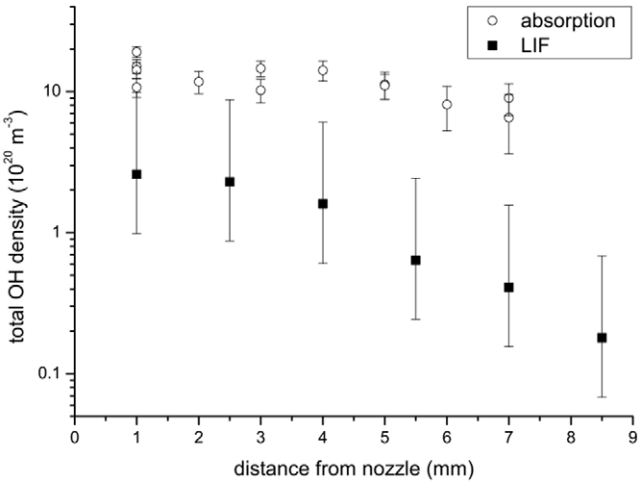

Figure 15. Comparison of LIF and UV-absorption on the OH radical determined in an RF plasma jet [201] (© IOP Publishing. Reproduced with permission. All rights reserved).

or use planar LIF on OH as a marker for the flow pattern of plasma jet effluents [202, 203]. In [170], LIF was used for OH in conjunction with laser absorption for ozone measurements. LIF measurements, however, require a method for absolute calibration, when absolute densities are required. If measured relatively, still processes such as the relevance of OH generation for H_2O_2 generation can be deduced [183]. A further drawback of LIF studies of OH is that quenching of the excited states introduces significant uncertainties on the measurements [12], and that the laser profile needs to be known, as it can distort the spectra used to determine OH densities [21]. Studies to detect OH via absorption spectroscopy are more rare, which can be attributed to the low absorption cross-section in the UV spectral range [204]. Therefore, OH has been detected by absorption either in a cavity ring down setup [205], or in plasmas with a long absorption length such as in [47] for an RF discharge similar to the planar APPJ [6]. OH has been determined by time resolved resonant absorption spectroscopy [206] or in combustion flames in conjunction with absorption temperature measurements [207]. Especially the commercial availability of new UV LEDs may provide better access to low density species by UV absorption spectroscopy. In [28, 162], a UV LED was used as a light source for broad band absorption spectroscopy on the OH radical. In this work, the absorption measurements served as a way to calibrate LIF measurements. For sensitivity, a key parameter is the LED radiance that can be guided to the detector. Suggestions to enhance this radiance were to use a more powerful LED, improve the collimation or use a larger CCD chip. Thus, the time resolution could be improved, or the sensitivity by decreasing the spectral bandwidth. In [77], the technique was improved by implementing a collimator system as shown in section 3.1 and the overall accuracy was raised.

An interesting example on why to use absorption spectroscopy can be found in a highly accurate single pass absorption measurement that has been performed in [201] on a filamentary RF argon plasma jet. Here, also a comparison of LIF and UV absorption measurements has been made (see figure 15).

Differences are attributed to the LIF uncertainties and can be partially explained by the filamentary character of the discharge in a turbulent channel [202].

While several groups are presently following cavity ring down approaches, single pass absorption has shown to yield accurate results.

A more exotic method to study OH has been applied to atmospheric plasmas in [208], where the so-called hook method is used to study the hydroxyl radical. The hook method consists in observing an interference structure of an absorbed and a reference beam in the shape of a hook occurring over a frequency variation. While the sensitivity of the method is not excellent and inferior to other techniques, it can be performed in single shot measurements.

In conclusion, UV spectroscopy is a simple and versatile tool for many species relevant in atmospheric plasma jets. A great variety of reactive species can be characterized. The drawback is the overlapping of spectral bands of different species, sometimes requiring a deconvolution or simulation procedure to interpret the signals. UV spectroscopy can be utilized to calibrate other more sensitive measurement techniques such as LIF spectroscopy. With the development of new light sources, which are more stable, collimated and point like, the technique gains in relevance, even for small scaled plasma sources.

3.4. Visible to NIR spectroscopy

The visible to near infrared (NIR) spectral region is dominantly used for studies of metastable species, as these are most prominent in this spectral region. However, in [162], the UV broadband absorption on a DB discharge was extended to the visible spectral region up to 800 nm in order to deconvolute the overlapping spectral features in the UV. In [209], a red LED was used to study NO_x trace gases in cavity enhanced absorption spectroscopy. Several Metastable spoecies have their transitions in the visible to NIR spectral region. Metastable formation by atmospheric pressure plasmas has been studied e.g. for argon, helium and nitrogen metastables. $N_2(A)$ metastables have been presumed to transport energy and initiate reaction chemistry in biologically relevant liquids [210]. $N_2(A)$ densities have been studied by emission spectroscopy [211]. Time-resolved $N_2(A)$ metastable densities were measured by the CRDS absorption technique using a ns-pulsed dye laser around 770 nm wavelengths (see figure 16). Noteworthy is the limit of detection down to 1 ppm for only 0.5 mm plasma length and the 50 ns time-resolution. Plasmas were produced by nanosecond repetitively pulsed discharges in nitrogen and air at atmospheric pressure [212].

In [18], $N_2(A)$ metastables were produced by an NRP discharge in atmospheric pressure nitrogen and were also measured by the CRDS absorption technique. Lateral measurements were realized by placing and translating the discharge at the cavity center. Space-resolved absorption coefficients were obtained after Abel-inversion (see figure 17).

Hovever, due to easier breakdown, most APP jets use argon or helium as main carrier gases. Due to their long lifetimes, argon and helium metastable states are often the most abundant

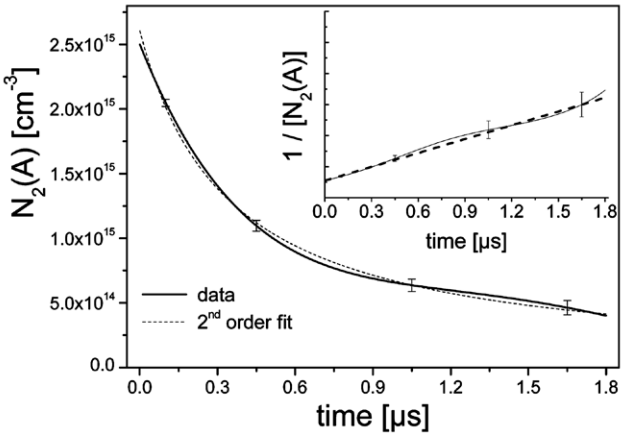

Figure 16. Time evolution of $N_2(A)$ metastable density measured by CRDS technique in nitrogen post-discharge generated by nanosecond repetitively high-voltage pulses. The inset shows a linear behavior of the reciprocal density indicating the pooling as the main loss process. (Reprinted with permission from [212]. Copyright (2010) American Chemical Society).

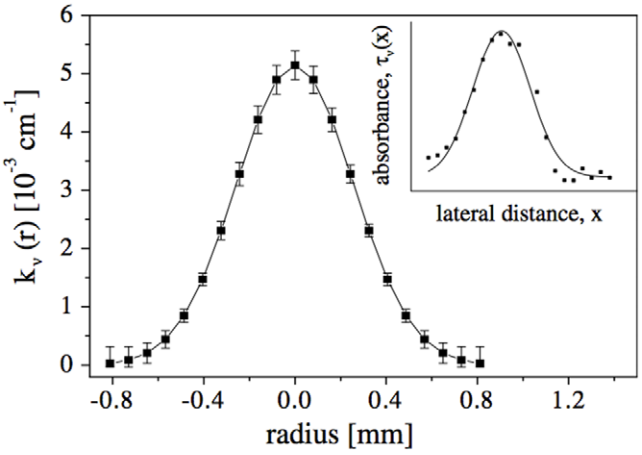

Figure 17. Radial profile of $N_2(A)$ absorption coeficient obtained after Abel inversion of CRDS lateral absorbance measurements in a nitrogen nanosecond repetitively pulsed discharge. The inset shows the lateral absorbance distribution [18] (© IOP Publishing. Reproduced with permission. All rights reserved).

energy carrying atoms in rare gas plasmas. Given their high potential energies (⩾11.5 eV for Ar,⩾19.8 eV for He), they are also an important reservoir of energy. Thus, they play a major role in plasma ionization, sustainment and excitation mechanisms. Stepwise ionization through these states is known to be a significant ionization process in low electron temperature high-pressure rare gas plasmas, as it is the case for APP jets. Rare gas metastable atoms are also an indicator of the presence of high energetic electrons, able to induce direct electron impact ionization and excitation. Furthermore, these species are very chemically active, having energies sufficient for the initiation of different chemical reactions. Therefore, the determination of the spatial-temporal absolute density distribution of argon and helium metastables is of high relevance to better understand the plasma physics and chemistry taking place in APPJs, a requirement for developing new applications and reliable process control.

Especially the density of metastable states of argon and helium has been studied in different APP jets [99, 107–114, 213–215]. As per definition, in a tuneable diode laser absorption spectroscopy (TDLAS) system, the light source is a tunable diode laser (TDL). Tuneable diode lasers typically have tuning ranges of a few GHz. Because the linewidth of the laser is negligible compared to the width of the absorption line (in particular at atmospheric pressure), not only the absolute density of the absorbing atoms (ground- or excited-state species) can be determined, but also the absorption profile can be recorded by scanning the laser frequency (achieved by changing either the temperature or the current of the TDL) across the absorption line profile without applying a deconvolution procedure, allowing to measure temperature, pressure, velocity and mass flux in the plasma volume (see section 2.4). Furthermore, the high spectral brightness of the laser and collimation over long distances allow distinguishing the laser radiation from the plasma background radiation as the latter decreases quadratically while the laser radiation remains constant with the distance. Another advantage of TDLAS is its high sensitivity and high temporal resolution. For instance, TDLAS allows the measurement of the concentration of trace gases below ppb if modulation techniques are employed. To resume, TDLAS is a reliable, relatively inexpensive, absorption spectroscopic technique providing the spectroscopic advantages of laser diagnostics in a compact, transportable and easy-to-implement system. In the following, TDLAS detection in the VIS to NIR spectral region of argon or helium metastables generated by APP jets is reviewed.

3.4.1. Argon metastables (visible). The density of the lowest argon metastable state atoms Ar($^3P_2$), which have an energy of 11.5 eV, has been measured by TDLAS ($4s^3P_2 \rightarrow 4p^3D_3$ transition of Ar at around 811.5 nm) in different APPJs: co-axial sinusoidal low frequency (40 kHz) driven [111], co-axial pulsed low frequency (22 KHz) driven [109], co-axial sinusoidal RF (1 MHz) driven [108], co-axial sinusoidal RF (13.56 MHz) driven [110] and planar sinusoidal RF (13.56 MHz) driven [107]. When operated in co-axial geometries, the Ar APP jets are characterized by the propagation of a fast ionization wave through the surrounding ambient air, producing a great variety of reactive species. In [111], Bussiahn *et al* reported a good correlation between the propagation of the ionization wave and the generation of Ar($^3P_2$) metastable atoms in the effluent of a co-axial sinusoidal low frequency (40 kHz) driven plasma jet. A similar behaviour of the spatio-temporal evolution of the relative densities of Ar($^3P_2$) metastables and of the intensity of the plasma emission in the visible spectral range was observed. Additionally, almost identical propagation velocities were also determined for the ionization waves (5–20 km s^{-1}) and the production zone of Ar($^3P_2$) metastable atoms (8–25 km s^{-1}). However, the observed spatio-temporal distribution of Ar($^3P_2$) metastables is much broader than that of the plasma emission due to the longer lifetimes of the metastables compared to the radiating species. Interestingly, the highest Ar($^3P_2$) metastables relative densities were measured in front of the nozzle. Co-axial argon jets in ambient conditions usually are filamentary and the ionization propagation pathway is defined by the impurities, which change due to the flow conditions [203]. Time-resolved optical emission measurements, using fast ICCD cameras, show that, even when appearing homogeneous to the naked eye, Ar plasma jets have usually a streamer-like character and a strong filamentary structure [108–111, 216]. The diameters of the single filaments have been estimated to few hundreds of μm. Even if TDLAS can be applied at very short absorption lengths, with the absorption being measured very accurately, a precise calculation of absolute metastable densities in measurements on single filaments is often unattainable. This is due to the fact that the spectral absorption profile is usually not constant both in time and space because of the strong fluctuating and inhomogeneous spatio-temporal character of the filaments, and the temporal resolution of current TDLAS setups (of few ns) is not high enough. Furthermore, the random filament position and thickness result in varying absorption lengths from one excitation cycle to another, as a coincidence of the fixed position of the laser beam and of the plasma filament position is a random event. In such inhomogeneous conditions, Abel inversion yields spurious results. Nevertheless, in [109] and [110], absolute densities of Ar($^3P_2$) metastables are determined using different approaches. In [109], Schröter *et al* studied a filamentary co-axial pulsed 22 KHz driven plasma jet, operated at atmospheric pressure in a quartz tube. A scan of the laser wavelength over the absorption profile allowed to obtain absolute values. Inside the filaments, Ar($^3P_2$) metastable densities of several 10^{14} cm^{-3} were determined. The estimation of the absorption length was performed by CCD imaging, which is less accurate than other methods, as the plasma emission is not necessarily related to the presence of Ar($^3P_2$) metastables, neither are they necessarily homogenously distributed. The temporal evolution of the Ar($^3P_2$) metastable density was found to have a reverse trend compared to the discharge current, the highest rise when the voltage is at its maximum value, and maxima correlated to minima of N_2 photoemission. Additionally, maxima of the Ar($^3P_2$) metastables density correlate with maxima of the diameter of plasma filament, which in [109] varies in time. Therefore, whenever the laser beam is equal or broader than the plasma filament, the absorption of Ar($^3P_2$) metastables is underestimated, while whenever the laser beam diameter is lower than the diameter of the plasma channel, the measured Ar($^3P_2$) metastable density is more reliable. In [110], space- and time-resolved measurements of Ar($^3P_2$) metastable atoms produced in a co-axial sinusoidal 13.56 MHz driven plasma jet are presented. The jet has an inner capillary, which can be used to add precursor for thin film deposition to the plasma zone similar to the one used in [217]. In the latter jet, a stable filament position can be achieved inside the capillary tube [218]. In [110], it was observed that the plasma extends up to 2 mm from the exit nozzle and, even if it appears homogeneous to the naked eye, it has a strong filamentary structure. Single filaments with a diameter of about 125 μm and metastable densities of few 10^{13} cm^{-3} were determined. Spectral absorption profiles were accumulated time-averaged over 500 pulse cycles, and the wavelength position of the maximum of the profile was used for space and time resolved measurements. However, as the spectral absorption profile is

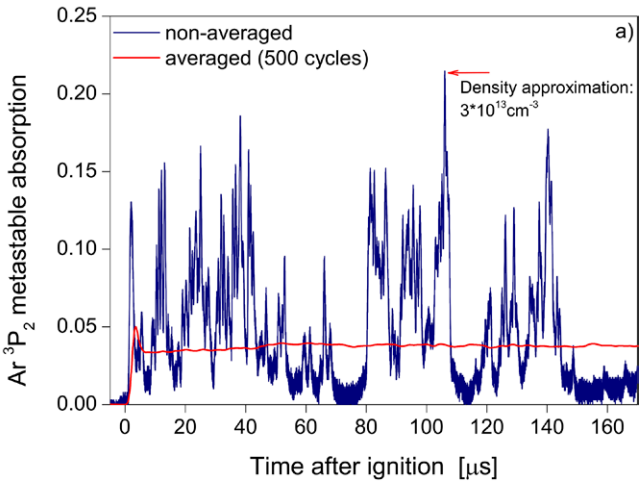

Figure 18. Non-averaged (blue) and averaged (red) time-resolved measurement of Ar($^3P_2$) metastables in the first 160 μs after the ignition of a co-axial sinusoidal 13.56 MHz driven argon jet, taken on the jet axis, about 200 μm in front of the nozzle. From [110] (© IOP Publishing. Reproduced with permission. All rights reserved).

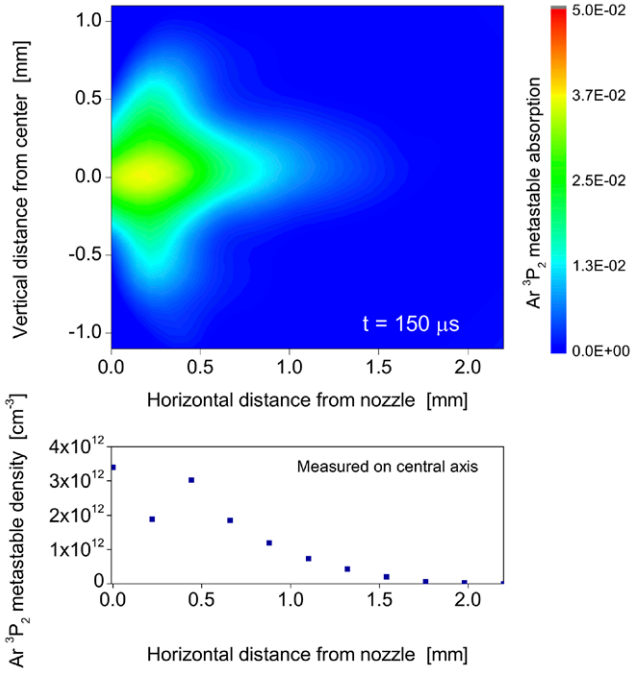

Figure 19. Top: averaged steady-state absorption map of the Ar($^3P_2$) metastable distribution, measured 150 μs after the ignition of a co-axial sinusoidal 13.56 MHz driven argon jet behind the nozzle. Bottom: steady-state density distribution on the central axis. From [110] (© IOP Publishing. Reproduced with permission. All rights reserved).

not expected to be constant in space and time, it is difficult to evaluate the precision of the calculation of Ar($^3P_2$) metastable absolute densities from time-averaged absorption data. Niermann *et al* observed a shift of the central position to longer wavelength by 3.3 GHz, which they attributed to Stark effects due to the high electron densities in the filament [110]. While the temporal evolution of each cycle is highly chaotic, averaging the signals resulted in stable signals, as it is shown in figure 18. The randomness of the signal is attributed to the following: whenever a filament crosses the laser beam, a strong absorption peak is obtained, while outside the filament, the absorption is more than one order of magnitude lower. As the first filament is, due to triggering, fixed in time, the average exhibits a stronger absorption signal at the beginning of the 170 μs recording window. A frequency analysis showed that the characteristic frequency of the filaments crossing the laser beam is around 1 MHz.

In order to determine the Ar($^3P_2$) metastable absolute densities, the full-width at half-maximum of the measured absorption profiles taken from 2D maps of the line-integrated averaged absorption (shown in figure 19 top) was assumed as absorption length. Thus, the calculated Ar($^3P_2$) metastable absolute densities are not the real densities found inside the filaments but rather time-averaged densities for a certain position in the plasma jet's effluent. The spatial absorption profiles have, on average, a symmetrical shape and extend up to 2 mm from the jet nozzle. As these 2D maps represent the probability of finding a plasma filament at a given position (averaging over 500 cycles), the star-shaped excitation profile in the effluent observed in figure 19 (top) can be easily explained by the bent course of the filaments that was determined by imaging [110]. Figure 19 (bottom) shows time-averaged absolute Ar($^3P_2$) metastable densities on the central axis from the nozzle of the jet. Due to the curved trajectory of the filaments, the time-averaged absolute Ar($^3P_2$) metastable density on the axis decreases first up to a distance of about 200 μm, it then increases up to a distance of around 400 μm, and it decreases again and continuously for longer distances from the jet's nozzle.

The temporal expansion of the plasma filaments coupled to the measurement of the dependence on the distance to the nozzle of the temporal Ar($^3P_2$) metastable absorption profile allowed Niermann *et al* to correlate the production of Ar($^3P_2$) metastable with the passage of an ionization wave.

Important for plasma medicine investigations is the interaction of the plasma jets with targets. In [110], the metastable were studied with and without a target in front of the plasma jet. While an electrically floating target does not affect the Ar($^3P_2$) metastable density distribution, a grounded target significantly changes the characteristics of the plasma jet. The plasma becomes more stable and is not any longer fully governed by the filamentary character observed in the free effluent. Close to the target's surface, the discharge spreads over a diameter of more than 3 mm. High Ar($^3P_2$) metastable densities can be maintained over the whole plasma column between the nozzle and the target, and on the target's surface. Under grounded target conditions the plasma column can even be extended over a distance of about 3 mm.

Finally, in [107] the spatial distribution of the absolute density of Ar($^3P_2$) metastable atoms in the plasma volume of a planar sinusoidal RF (13.56 MHz) driven helium plasma jet with up to 10% argon admixture was measured for various discharge conditions. In order to obtain absolute values for the Ar($^3P_2$) metastable density, the spectral absorption profile was recorded and analysed, enabling the determination of the pressure broadening and the peak intensities. Ar($^3P_2$)

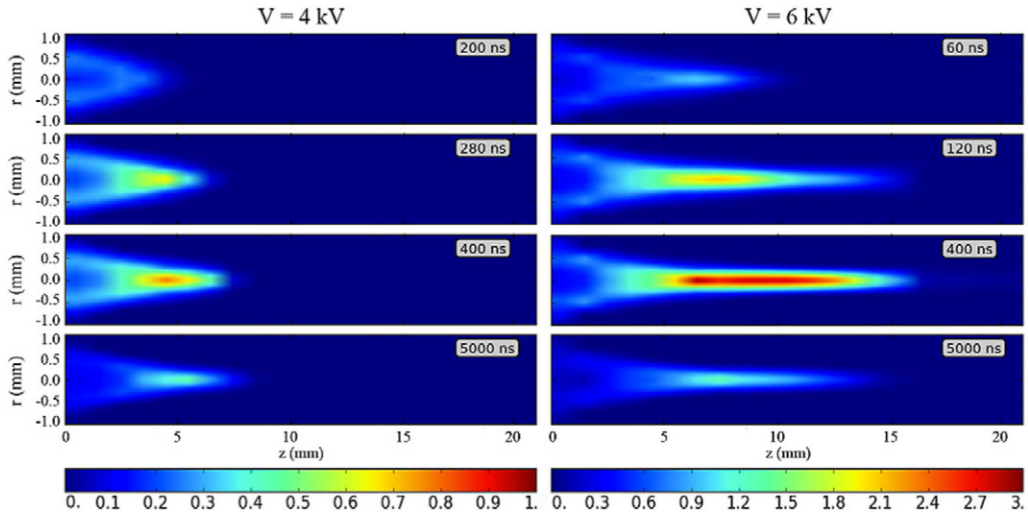

Figure 20. Snapshots illustrating the temporal evolution of the spatial distributions of the He(2^3S_1) metastable states produced during the propagation of a co-axial positive pulsed 20 KHz driven helium plasma jet into ambient air. The density unit indicated by the color bar is 10^{13} cm^{-3}. (© 2014 IEEE. Reprinted, with permission, from [213]).

metastable concentrations spanning from 10^9 to few 10^{11} cm^{-3} were measured in the plasma volume, while no metastables were detected in the effluent region behind the electrodes, even at higher power conditions. The density profiles between the electrodes reflected the plasma excitation distributions in the plasma volume, highlighting the sheath structure. It was observed that the Ar($^3P_2$) metastable densities depend strongly on the argon admixture to the helium feed gas. At 4% argon fraction, the Ar($^3P_2$) metastable density reaches its maximum and then it decreases for higher Ar admixture. Furthermore, a significant influence of air impurities on the Ar($^3P_2$) metastable density was determined. A study of the dependence of the metastable density on the power found a linear correlation of increasing argon metastable density with increasing applied power.

3.4.2. He metastables (NIR). TDLAS has been used to measure the density of the lowest helium metastable state atoms He(2^3S_1), which have an energy of 19.8 eV, by probing the $2^3S_1 \rightarrow 2^3P_{0,1,2}$ transition of He at around 1083 nm, in different APP jets: planar sinusoidal RF (13.56 MHz) driven [107, 114, 214, 215], bipolar pulsed low frequency (5 KHz) driven [113], co-axial positive pulsed low frequency (20 KHz) driven [112, 213], co-axial sinusoidal RF (1 MHz) driven [99]. Contrary to the operation in argon, the helium APP jets are diffuse, even in co-axial geometries, in which they are, as for the case of argon, characterized by the propagation through the surrounding ambient air of a fast ionization wave, producing a lot of reactive species. In [107, 114, 214, 215], the role of air impurities and minority admixtures of argon and O_2 on the He(2^3S_1) metastable density produced in a similar planar sinusoidal RF (13.56 MHz) driven APP jet was studied. Niermann *et al* found that ambient air intrusion through the front nozzle significantly quenched the He(2^3S_1) metastable density [107, 214, 215] resulting in an increase in density with gas flow, due to the reduced impurities density. Less impurities not only reduce metastable quenching by Penning ionization, but it also reduces electron energy loss to vibrational and rotational excitation of impurities. Another source of air impurities contaminating the feed gas is the gas supply system. For proper determination of the metastable density, the best is to work with stainless steel gas tubing, which should be conveniently and equally purged before each TDLAS measurements to remove excess impurities, especially humidity [175]. In [107], the influence of up to 5% Ar admixture was also studied. A strong decrease of the He(2^3S_1) metastable density with increasing Ar admixture was observed. Niermann *et al* explained this with the lower excitation threshold of 11.55 eV for Ar($^3P_2$) metastables compared to 19.82 eV for He(2^3S_1) metastables. In [114], it was found that the He(2^3S_1) metastable density decreases exponentially with increasing O_2 admixture, attributed to metastable quenching by Penning ionization with O_2, or due to a decrease of the electron temperature resulting from inelastic electron-impact collisions with O_2 and perhaps O_3 (produced by the plasma). In [114], the experimental results were compared with a numerical simulation of the plasma, allowing the identification of the main formation mechanisms of He(2^3S_1) metastable atoms, and the analysis of their pronounced spatio-temporal dynamics. However, it was concluded that on this APP jet the He(2^3S_1) metastable atoms are not an important energy carrying species into the jet effluent and therefore will not play a direct role in remote surface treatments using this planar RF-driven APPJ. The absence of He(2^3S_1) metastable atoms in the effluent region behind the electrodes was also experimentally observed by Niermann *et al* [107]. The He(2^3S_1) metastable density increases slightly over-linearly with increasing RF power [107]. Finally, the density profiles of He(2^3S_1) metastable atoms in the volume between the electrodes observed in [107, 214, 215] revealed the sheath structure, reflecting the plasma excitation distribution which is determined by the electron density and temperature distribution in the discharge volume. In [214], the spatial profiles were obtained for various electrode gap distances, showing the transition from a normal glow plasma to a pure sheath discharge.

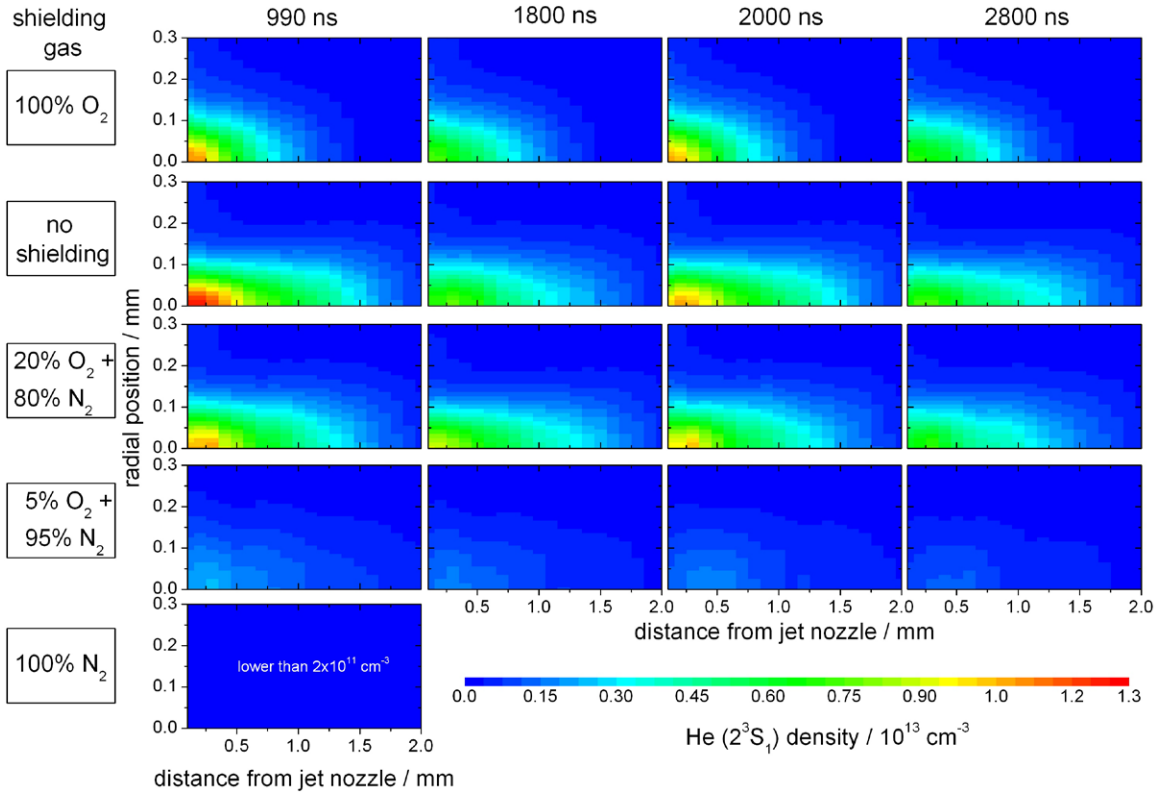

Figure 21. Spatio-temporal He(2^3S_1) metastable density measured in a co-axial sinusoidal RF (1 MHz) driven He plasma jet. From [99] (© IOP Publishing. Reproduced with permission. All rights reserved).

While [107, 114, 214, 215] found He(2^3S_1) metastable densities up to few 10^{11} cm^{-3} in a planar sinusoidal RF (13.56 MHz) driven APP jet, Douat *et al* measured much higher He(2^3S_1) metastable densities, up to some 10^{13} cm^{-3} (2 orders of magnitude higher) [112, 213] in a co-axial positive pulsed low frequency (20 KHz) driven APP jet. Thanks to the cylindrical symmetry of this plasma jet, the radial distributions were deduced using Abel transforms, and the temporal evolution of the spatial distribution of He(2^3S_1) metastable atoms was investigated (see figure 20). It was observed that as the plasma jet propagates, the He(2^3S_1) metastable density radial distribution evolves from a ring shape, observed near the exit of the dielectric tube, to a conical form centered on-axis. On the same jet setup, a similar evolution of the spatio-temporal distribution was also observed for the electron density [219] as well as for the plasma emission [112]. In particular, the spatio-temporal evolution of the radial distribution of the first negative system of N_2 is similar to that of the He(2^3S_1) metastable atoms, indicating that N_2^+ is mainly populated through Penning ionization of N_2 by He(2^3S_1). As shown in figure 20, the spatio-temporal distribution of the He(2^3S_1) metastable density depends on the applied voltage, with higher He(2^3S_1) metastable densities being obtained for higher applied voltages. By measuring the characteristic decay time of the metastable atoms, Douat *et al* determined that a region of the plasma jet that appears pink to the naked eye and is rich in He(2^3S_1) metastable atoms corresponds to a plasma volume where the value of the decay time is constant and approximately equal to 5 μs. Given that according to [42, 220] the theoretical lifetime of He(2^3S_1) metastable in pure helium is expected to be 5.8 μs, the He gas in this pink cone is only faintly contaminated.

In [99], the impact of different oxygen/nitrogen shielding gas mixtures on the He(2^3S_1) metastable density generated by a co-axial sinusoidal RF (1 MHz) driven APPJ is discussed. Spatio-temporal as well as radial profiles, determined by means of Abel inversion technique, of He(2^3S_1) metastable atoms are presented (see figure 21). The surrounding atmosphere of the plasma jet was varied from pure oxygen to pure nitrogen with a gas shielding device [221]. This technique allows to tune the plasma for a targeted biological effect [222]. Similarly to the above-mentioned co-axial APPJ, He(2^3S_1) metastable densities up to few 10^{13} cm^{-3} were obtained, however at different distributions and shorter plume length. Concerning the different shielding gas compositions, the highest He(2^3S_1) metastable density was found for the absence of shielding gas, in which the volume where He(2^3S_1) metastable atoms are detected is also the greatest. Logically, a similar spatial density profile was obtained when shielding the plasma jet with artificial air (20% O_2 + 80% N_2). For pure O_2 shielding, the plasma volume rich on He(2^3S_1) metastable atoms is much smaller. For small O_2 fractions on the gas shielding (5% O_2 + 95% N_2), the He(2^3S_1) metastable density decreases significantly but the spatial profile remains almost similar to that of artificial air (not clearly seen in this figure). Indeed, the lower the O_2 amount on the gas shielding, the lower the He(2^3S_1) metastable density. When no O_2 is present in the shielding gas (pure N_2 shielding), no He(2^3S_1) metastables can be measured at all. Most interestingly, even when N_2 was replaced by Ar, a similar behavior was observed (not shown in this

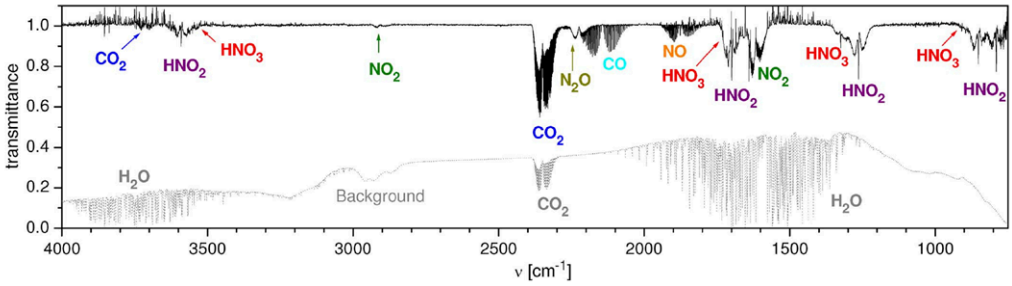

Figure 22. Broadband multipass FTIR absorption spectrum of an argon atmospheric plasma jet with air admixture (© 2009 IEEE. Reprinted, with permission, from [234]).

figure). In [223], Schmidt-Bleker *et al* attributed this behaviour to a focusing of the electric field by negative oxygen species. The electric field generated by the anions contributes to a focusing of the electrons towards the center of the helium channel, thereby promoting the propagation of the ionization wave during the negative phase. In this way, anions can be generated at distances of a few mm from the jet nozzle. These anions can then provide the seed electrons for the counter-propagating streamer observed during the next positive phase [223]. From the decay times of He(2^3S_1) metastables (in the range of 2.3 μs $\pm$ 0.1 μs), and from diffusion analysis, it was concluded that feed gas impurities, especially water molecules, are more likely responsible for the determined high quenching rate. Thus, again, for the measurement of He(2^3S_1) metastable atoms density, the use of stainless steel tubes for the gas supply system is recommended. The evaluation of the temporal evolution of the He(2^3S_1) metastable density revealed that the metastables atoms are only produced in the positive phase of the applied voltage. The He(2^3S_1) metastable density never drops to zero during a voltage period, as the decay time of He(2^3S_1) is larger than the period of the voltage signal, and it is, thus, significant for the reactive species generation in the plasma jet.

It can be concluded that argon metastable measurements are particularly challenging, due to the filamentary nature of the discharge. Good time and space resolution can be gained depending on the type of detector used. Due to the stochastik nature of the filament position, averaging and Abel inversion are intricate and sometimes impossible. In helium, the measurement is somewhat simpler as the discharges typically are homogeneous and averaging or Abel inversion procedures can be applied. Important are impurities, as they have a strong influence on the measured densities. Good care has to be taken to have a pure environment and feed gas tubings. Analysing metastable species can yield important insights into the discharge mechanisms, which makes Visible and NIR TDLAS an important measurement technique for atmospheric plasma jets.

3.5. MIR absorption spectroscopy

Absorption spectroscopy in the infrared has the advantage that required photon energies lie in the order of 0.1 eV for the MIR, the spectral range from 2 to 30 μm. This means that even high power light sources do not disturb the plasma. Furthermore, in the MIR, ro-vibrational bands of a large variety of hetero nuclear and thus infrared active molecules are present [38]. Although the absorption cross-sections of these transitions are usually orders of magnitude smaller than for transitions in the UV spectral range, they are typically two orders of magnitude larger than in the near-infrared. The high selectivity of molecular spectra in the MIR with their relatively strong absorption cross-sections makes this spectral region ideally suited to study the composition of reactive atmospheric plasmas. IR spectroscopy has been used in atmospheric diagnostics for decades [224, 225]. Both broadband non-coherent light sources and lasers are used for spectroscopy in the MIR as described in the following.

3.5.1. FTIR absorption spectroscopy. Spectroscopic setups with continuous light sources and dispersive spectrometers or Michelson spectrometers such as FTIR spectrometers can be used to detect infrared active molecules. In FTIR spectrometers, the spectral resolution can be up to 0.001 cm^{-1} for a (?) given integration time and long Michelson mirror pathway, although typical laboratory FTIRs have spectral resolutions around 0.1 cm^{-1}. Spatial resolution is harder to achieve than for UV or visible light absorption setups. But, nevertheless, recently, an FTIR absorption spectroscopic setup, that achieves a 2 mm lateral resolution, has been applied in low pressure [226]. Collimating optics were placed inside the FTIR sampling chamber, the IR beam was guided through the 50 mm long plasma chamber and a retro reflector was placed at the other side of the plasma. Gas phase analysis with a FTIR spectrometer is known, e.g. from NO_x removal in exhaust gas with DBD discharges [227], plasma driven catalysis for VOCs removal [228], or hydrocarbon assisted NO oxidation in diesel exhausts from ships [229]. While FTIR absorption spectroscopy is better known for its application in low-pressure reactive plasmas for process monitoring, it has been used more and more at atmospheric pressure to study the reactive species generation in discharges. In [230], an FTIR gas analyser was used on a DBD for mechanism studies on the deactivation of *Escheria Coli*. The identification of fundamental mechanisms through peroxynitride formation in a DBD treated liquid was supported by identification of HNO_3 and ONOOH in the gas phase [230]. In [227], a DBD operated with dry gas was studied and the NO_x reaction chemistry was observed simultaneously for several species. In [231], a DBD is studied with an *in situ* FTIR setup. Here, the reaction chemistry is studied in

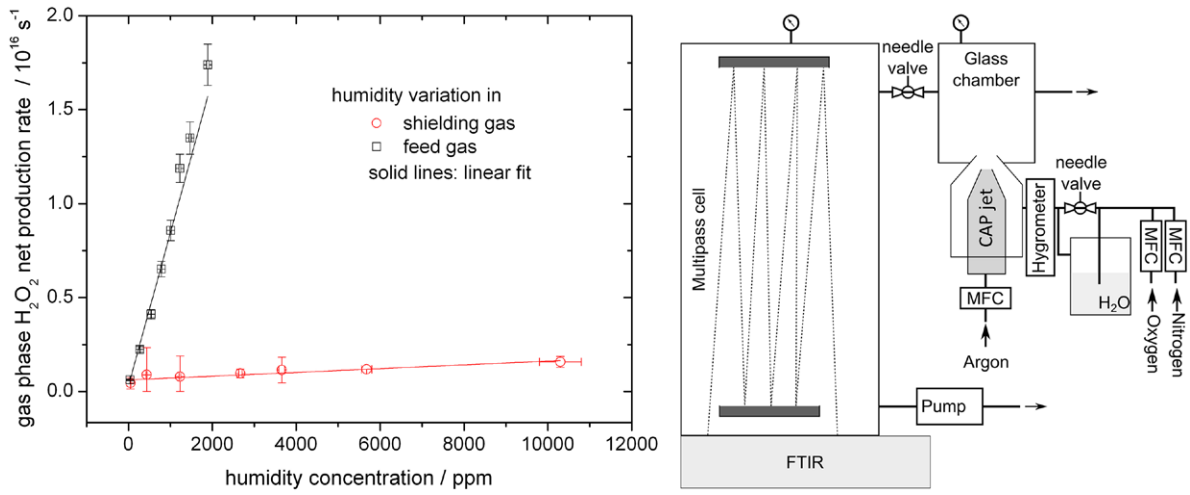

Figure 23. Development of H_2O_2 as a function of humidity admixture to the feed gas or ambient of an argon RF plasma jet (left) [240]. Setup of the FTIR measurements and the sampling chamber (right) [238] (© IOP Publishing. Reproduced with permission. All rights reserved).

the diffusion-dominated zone between discharge and treated surface. The absorption length is 50 mm. In [232], the CF_2 concentration in a depositing argon/fluorocarbon DBD was studied. In [191], the NO and O_3 density in the plasma was studied both with FTIR and UV-absorption spectroscopy. For the UV absorption measurements, cross-sections from [233] were taken. The difference between UV and FTIR measurements were relatively large with a factor of 2, which was attributed to erroneous FTIR measurements rather than UV absorption spectroscopy. The work shows the correlation of power input into the gas volume and NO/O_3 ratio. Longer treatment times or higher power density result in higher gas volume temperature yielding a reduction of ozone and an increase in NO derived species.

FTIR spectroscopy has also been applied to jet diagnostics. While Moravej used IR absorption to indirectly measure atomic oxygen by titration [141], Pipa *et al* [234] performed a first study directly on the RF atmospheric plasma jet generated species with FTIR absorption. The studied plasma source was similar to the kinpen. Production rates of molecules NO, NO_2, N_2O, $HNO_{2/3}$ as well as CO and CO_2 (from impurities or wall reactions) have been detected (see figure 22). Spectral data were taken from a compilation of $H_xN_yO_z$ spectroscopic experiments in a review [235], and for the case of HNO_2 from the ATMOS [236] database as well as HITRAN [39] and the commercially available QASoft database [237].

The combination of multipass absorption for high sensitivity with plasma kinetics simulation is a promising approach [231]. In atmospheric plasmas, this has been applied in [238] to gain further insight into reactive species production. Here, a kinpen was placed inside a collecting vessel from which the gas was sampled into the multipass cell (see figure 23 right). With a time dependent weighting function, resulting from flow dynamics calculations, residence times were estimated and the reaction dynamics was calculated [238]. The same setup was used to study the mechanisms of hydrogen peroxide formation by adding humidity to the feed gas of the kinpen [175, 239]. It was found that cell viability correlates under the studied conditions with H_2O_2 production rate. If H_2O_2 is held constant, other effects dominate the cell activity inhibition [10, 222]. A comparison of feed gas effects to ambient effects reveals that core plasma effects dominate the hydrogen peroxide production (see figure 23) [239, 240].

In [238], a parameter variation of the surrounding gas of the plasma jet served as an input for a simple chemical kinetics model. This was possible as the core plasma conditions remained constant, while the reactive species composition was varied and the long living species composition was varied. This was detected in the multipass cell, and, from the chemical kinetics model, valuable insights into the reactive species generation could be gained so that the development of, e.g. ozone and NO_2, could be fitted with only one fitting parameter (see figure 24).

To summarize, FTIR is a versatile technique detecting various species in parallel and having the advantage to make a specific identification of individual absorbing species possible. The disadvantage of low sensitivity can be overcome by sampling the plasma generated reactive species in a multipass cell and combining the measurements with modelling. From this, valuable insights into reactive species pathways can be gained.

3.5.2. MIR-LAS. Over the last two decades, mid-infrared laser absorption spectroscopy (MIR-LAS) in the molecular fingerprint region from 3 to 20 μm has evolved into a powerful and versatile diagnostic technique for *in situ* plasma studies. Laser based spectrometers operating in the MIR enable access to strong fundamental vibrational bands of many compounds with absorption cross-sections that are typically two orders of magnitude larger than in the near-infrared. MIR-LAS provides a means of determining the absolute concentrations of the ground states of stable and transient molecular species at time resolutions below a microsecond, which is of particular importance for the investigation of reaction kinetics and dynamics. Especially for irreproducible plasmas, absorption laser systems were developed allowing for time-resolved absorption profile measurements. In [37], the methyl radical

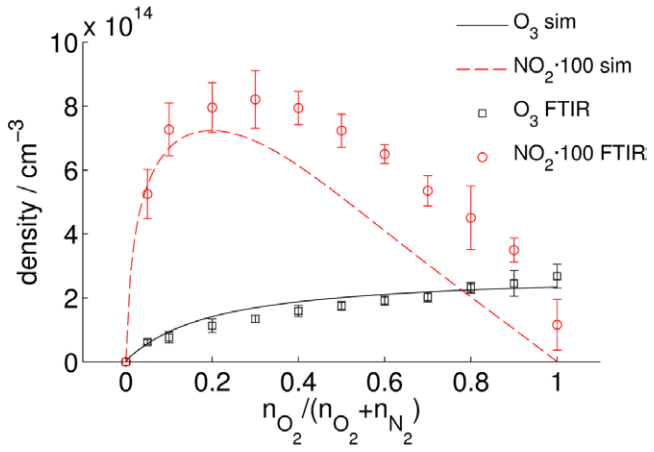

Figure 24. Density of ozone and nitrogen dioxide upon oxygen to nitrogen shielding gas variation [238] (© IOP Publishing. Reproduced with permission. All rights reserved).

was measured in low-pressure microwave plasmas using a MIR lead salt diode laser with a resolution of 1 ms. Entire line profile scans were performed, therefore all broadening changes in time could be taken into account.

Information about gas temperature and population densities can also be derived from MIR-LAS measurements. Apart from well-known FTIR spectroscopy, also laser based diagnostics have been applied in this spectral region due to the development of new light sources [241]. Continuous wave (cw) tunable lead salt diode lasers have been the most popular devices for tunable diode laser absorption spectroscopy (TDLAS) in this region, because they offer relatively high spectral intensity, narrow bandwidth (10^{-3}–10^{-4} cm^{-1}), and continuous tunability (typically 10s of cm^{-1}) over an absorption profile. However, output powers tend to be fairly low (sub-mW), and, more importantly, these lasers have the drawback that they require cryogenic cooling. A recent review on the application of lead salt TDLAS to plasma diagnostics can be found in [242].

As far as we know only two papers have been reported by Pipa *et al* on the application of TDLAS with lead salt lasers in the mid infrared to study the gas phase of a kinpen like atmospheric plasma jet, both related to the production rate of NO molecules [243, 244]. The higher sensitivity and better signal-to-noise ratio of TDLAS measurements allowed a more accurate and detailed quantitative analysis of NO production compared to previous reported FTIR absorption spectroscopy on the same jet [234]. In both, the measurements were performed with the transportable two laser beam infrared (TOBI) system [245] and the kinpen was mounted in an astigmatic Herriot multipass cell (100 m optical path in 3 l volume). It was demonstrated that TDLAS is capable to provide reliable measurements even under unfavourable conditions present in APPJs, namely its small dimension, short absorption length, unfavourable jet geometry, high gas flow conditions, etc. Furthermore, the absolute concentration measurements agreed very well with results from OES measurements in the UV region of the spectrum [243, 244].

An alternative to direct MIR sources is the production of radiation via nonlinear optical processes utilizing widely available room temperature laser sources in the near-infrared (NIR). These lasers have the same advantageous features as the lead salt diode lasers but without the necessity of cryogenic operation, which makes their use much simpler. Besides, because of their importance to telecommunications, they are based on mature technology. In difference frequency generation (DFG), the NIR lasers are mixed in a nonlinear crystal to produce a beam in the MIR with optical qualities directly related to those of the source lasers. Primarily, periodically poled lithium niobate (PPLN) has been used either in a DFG or optical parametric oscillator (OPO) arrangement to generate radiation in the MIR [246]. Recently, the practicality of a compact solid-state laser based DFG system has been demonstrated as a tool for probing low pressure hydrocarbon based plasmas [247].

Developments in material engineering led to the introduction of the quantum cascade laser (QCL) by Faist *et al* in 1994; a narrow band, relatively high powered, semiconductor based laser, producing radiation in the MIR [248]. Radiation is generated in aligned biased multi quantum wells in a semiconductor layer stack. Furthermore, as the energy levels within the wells are determined by quantum confinement, the energy of the lasing transition is determined entirely by the thickness of the layers and there is no need to use exotic materials with specially designed band gaps. As a result, the emission wavelength of the laser can be tailored over a wide wavelength range throughout the infrared molecular fingerprint region and beyond (3 to 300 μm). Nowadays, commercially available thermoelectrically cooled semiconductor cw QCLs operating near room temperature have become standard technology with only water assisted Peltier cooling. Furthermore, distributed feedback (DFB) QCLs provide (i) continuous mode-hop free wavelength tuning, (ii) increasingly high output powers up to hundreds of mW, and (iii) narrow linewidth radiation. These features make them an attractive and competitive radiation source for infrared laser spectroscopy in comparison with lead salt diodes and radiation generated via difference frequency mixing.

Consequently, pulsed and cw DFB-QCLs are rapidly becoming the radiation source of choice for working in the MIR for wavelengths longer than 3.4 μm, and interband cascade lasers (ICLs) for shorter wavelengths. The tunability of commercially available DFB-QCLs is typically limited to a few cm^{-1}. For more information on the developments and applications of DFB-QCLs, we refer the reader to various review articles and the references therein [66, 249–253]. In contrast to DFB-QCLs, external-cavity quantum cascade lasers (EC-QCLs) have tuning ranges of up to 200 cm^{-1}, which, when combined with their high output power of up to 350 mW and narrow linewidths, open up new possibilities in high resolution absorption spectroscopy including multicomponent detection encompassing molecules with broader absorption structures. For more details on the developments and applications of EC-QCLs, we refer the reader to various articles [254–258] and the references therein. All these developments have stimulated very significant improvements in QCLAS for plasma diagnostic purposes [66, 252].

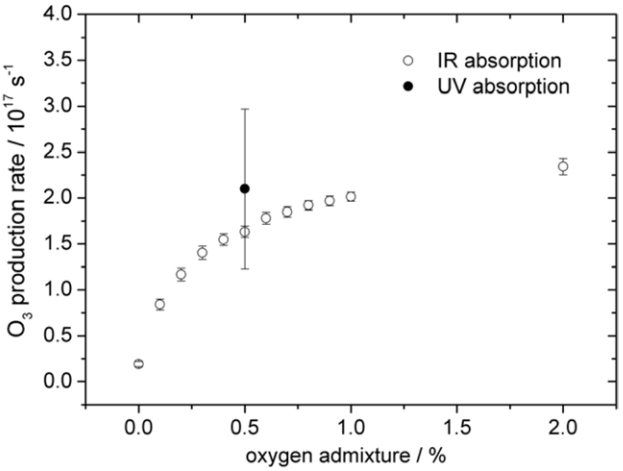

Figure 25. Comparison of UV and MIR absorption measurements on ozone [60] (© IOP Publishing. Reproduced with permission. All rights reserved).

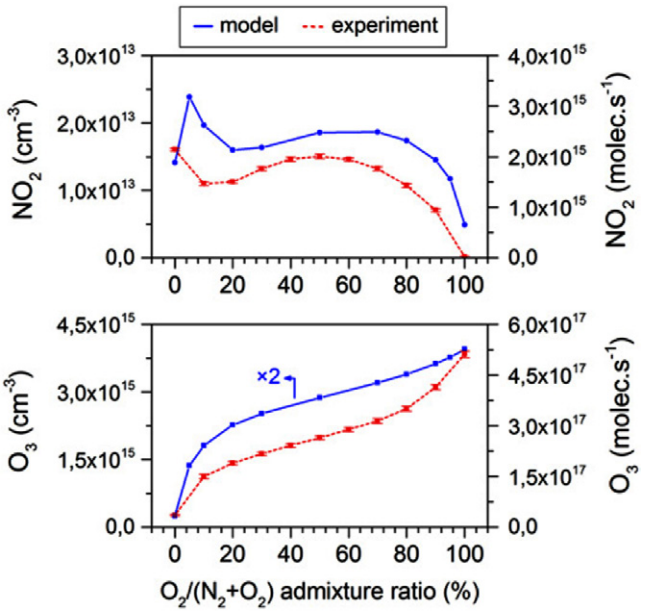

Figure 26. NO_2 and O_3 densities in a multipass measurement chamber obtained by QCLAS and calculated data from a RF-jet model in different $O_2/(O_2 + N_2)$ ratios. From [267].

Since kinetic processes are inherent to plasmas ignited in molecular gases, high time-resolution on subsecond timescales with high sensitivity is frequently desired for fundamental studies as well as for process monitoring in applied research and industry. Pulsed DFB-QCLs can be operated at high repetition rates (kHz) in the so-called intrapulse operation mode, allowing the study of fast kinetic processes. This is because a complete absorption spectrum may be obtained during a single current pulse of tens up to hundreds of nanoseconds. In this intrapulse mode, the QCL laser is scanned through the Doppler width of a transition on a time scale that is much faster than the relaxation processes in low-pressure gases, resulting in the occurrence of the so-called rapid passage effect. Although this effect distorts the lineshape of the transition profiles and thus leads to lower quantitative accuracy, still accurate densities and rotational temperatures of species in low-pressure plasmas can be obtained [243, 250–253]. Indeed, here is one of the few effects that do not disturb measurements at atmospheric pressure, which means that this relatively simple method is ideal to study fast kinetic processes in atmospheric plasma jets.

To enable multi-component detection with high time-resolution, a compact and transportable three channel QCL system, TRIPLE Q, has been developed. In the TRIPLE Q spectrometer, the radiation of three independently controlled QCLs is combined. This setup was used for time-resolved studies of multiple molecular components in a low pressure discharge tube [259]. All three QCLs are operated in the intrapulse mode with typical pulse lengths of the order of 100 to 200 ns. Using a multiplexed detection arrangement, N_2O, NO and NO_2 were measured with a (total) time resolution of better than 1 μs. How a pulsed QCL can provide a simple method for probing the kinetics of transient species has been reported for CF_3 [57].

While QCL absorption spectroscopy (QCLAS) has been in use for the monitoring and diagnosis of molecular plasmas in research and industrial environments [56, 66, 252, 260–265], species generated by atmospheric pressure plasmas have only recently been studied with this method [60, 240, 266]. Reuter at al [60] used QCLAS to investigate the ozone production rate in a MHz argon atmospheric plasma jet. For these measurements, a commercial absorption spectrometer (Q-MACS, neoplas control GmbH) has been used, with a specification of the spectral resolution of 0.004 cm^{-1}, which offers a higher resolution than a more commonly used FTIR spectrometer. A total absorption length of 16.8 m was achieved by placing the plasma jet in a multipass White cell at atmospheric pressure and in ambient air, to allow the plasma jet to be operated under the same conditions as in open air. It yielded high sensitivity results of the spatially averaged ozone concentration of the jet with high accuracy. The results were in excellent agreement with UV-absorption spectroscopy in the Hartley band to determine the space-resolved distribution of the ozone concentration in the jet effluent (see figure 25) [60].

The same setup was later on used to study the influence of ambient and feed gas humidity on ozone generation by the plasma [240]. Iseni *et al* investigated the NO_2 production dynamics for a RF argon plasma jet (kinpen) operating at ambient conditions using QCLAS [266]. Again the plasma jet was placed inside a multipass White cell with open gas flow. In a recent paper, the absolute net production rates of O_3 and NO_2 species have been measured with QCLAS for an atmospheric plasma jet operating in Ar with different admixture fractions of nitrogen and oxygen with a dry air gas curtain surrounding the device [267]. The experimental data were compared to the production rates of these reactive molecules calculated with a 0D semi-empirical reaction kinetics model. A very good qualitative and even quantitative agreement between the calculated and measured data has been demonstrated (see figure 26).

Furthermore, it was shown that such a combination of experimental and theoretical investigations can be used to acquire important insight in the reaction kinetics in all

Species	Light source	Plasma source	Absorption length	Time resolution	Density measured	Lower detection limit	Error	Technique	Ref.
OH	DBD	DBD	20 cm	$\geqslant$ 200 ns			10%	Resonant Absorption	[206]
OH	UV LED	Jet	0.4 mm	None	10^{15} cm^{-3}	$\leqslant 8 * 10^{20}$ m^{-3}	50 100%		[21, 201]
OH	UV LED	DBD			$(2.6 \pm 0.65) \times 10^{13}$ cm^{-3}		50%		[28]
OH	UV LED	RF Glow Discharge	10 cm	None	0.6–4 10^{14} cm^{-3}				[47]
OH	UV LED	Plasma jet	0.4 mm	200–400 ns	$(1.5 \pm 0.3) \times 10^{16}$ cm^{-3}			BB-UV absorption	[21]
O_3	D_2-Lamp	RF Jet	1–2 mm FWHM		0.1–1.5 $\times$ 10^{16} cm^{-3}			UV absorption (imaging Spectrograph) & wavelength selected D2 Lamp	[100]
O_3	FTIR Hg-Lamp	RF-Jet	19.2 m		Production rate 0.5–4 $\times$ 10^{17} s^{-1}			FTIR & UV absorption	[175]
O_3	KrF Excimer Laser	Needle Plate Corona	1.2 mm	20 μs	1–10 $\times$ 10^{15} cm^{-3}				[169, 170]
O_3	D_2 Lamp	RF Jet	4–9 mm (UV)		6.5 $\times$ 10^{15} cm^{-3}			UV absorption QCLAS	[60]
O_3	Hg-Lamp	μAPPJ	1–4 mm FWHM		relative			UV-absorption	[174]
O_3	Hg-Lamp	APPJ	10 cm		1–6 $\times$ 10^{15} cm^{-3}			UV-absorption	[164, 165]
O_3	FTIR Hg-Lamp	Surface DBD	50 mm	30 s–3 min	1000–6000 ppm		Factor of 2 difference	FTIR & UV absorption	[191]
O_3	D_2-Lamp	MCSD	8–50 cm	None	10^{12}–10^{16} cm^{-3}	1.0 $\times$ 10^{12} cm^{-3}	0.1%	UV absorption	[128, 130, 167]
O_3	QCL	RF Jet	16.8 m (MIIR)	10 min	(8–93) $\times$ 10^{13} cm^{-3}	300 ppb	4%	QCLAS	[60]
O_3	HG Lamp	RF APPJ	3 mm–40 mm		0.03–6 $\times$ 10^{15} cm^{-3}			UV Absorption	[96]
O_3	Ar/HG Lamp	DBD	26 mm		10–4000 ppm			UV Absorption	[179]
O(^{3}P)	MHCD	Ar-Jet	6.5 mm		10^{15} cm^{-3}			VUV resonant absorption	[147]
O(^{3}P)	MHCD	Ar-Jet	6.5 mm		1–10 $\times$ 10^{14} cm^{-3}			VUV resonant absorption	[149]
N_2(A)	YAG dye	ns pulsed plasma	0.6 mm	50 ns	1.0 $\times$ 10^{14}–2.5 $\times$ 10^{15} cm^{-3}	1 ppm	40%	CRDS	[211]
H_2O_2	FTIR	RF Jet	19.2 m		Production rate 0.1–2 $\times$ 10^{16} s^{-1}			FTIR Multipass	[240]
H_2O_2	FTIR	RF -Jet	19.2 m		1–5 ppm			FTIR Multipass	[183]
H_2O_2	FTIR	RF -Jet	19.2 m		Production rate 0.1–2 $\times$ 10^{16} s^{-1}			FTIR Multipass	
O_3, N_2O_4, NO_2, N_2O_5, NO_3	D_2 Halogen Lamp	DBD	2.4 cm	15–90 s	10–5000 ppm			UV-VIS w. deconvolution & Modell	[162]
NH_3	FTIR	DBD	5 cm $\times$ 2 mm		200 ppm			FTIR Absorption	[226]

(*Continued*)

NO_2, O_3	FTIR	RF Jet	19.2 m		2×10^{12} cm^{-3} $1–10 \times 10^{14}$ cm^{-3}			FTIR Multipass	[238]
NO_2	Lead-salt diode laser	RF Jet	100 m		5–150 ppm		10%	TDLAS	[244]
NO_2	QCL	RF Jet	19.2 m	10 min	350–1000 ppb	20 ppb	80 ppb	QCLAS	[266]
NO	Lead-salt diode laser	RF Jet	100 m		0.1–200 ppm		10%	TDLAS	[244]
O_2	Ar Excimer	RF-Jet	4–10 mm	1–5 min	Up to 10^{17} cm^{-3}		10%	Self absorption	[135]
NO, CO	QCL	Nanosecond repetitively pulsed discharge	2 m	1–10 s	1–240 ppm, 8–1000 ppm	1 ppm	10%	QCLAS	[265]
$O_2(a^1\Delta_g)$	Microwave hydrogen plasma	MCSD	50 cm	none	$10^{13}–10^{16}$ cm^{-3}			VUV absorption	[128]
$Ar(^3P_2)$	TDL (811.5 nm)	Co-axial RF jet	125 μm	40 ns	$10^{11}–10^{13}$ cm^{-3}			TDLAS	[110]
$Ar(^3P_2)$	TDL (811.5 nm)	Co-axial pulsed kHz jet	200–350 μm	< 1 μs	$10^{13}–10^{14}$ cm^{-3}			TDLAS	[109]
$Ar(^3P_2)$	TDL (811.5 nm)	Planar RF jet	1 mm		$10^{9}–10^{11}$ cm^{-3}			TDLAS	[107]
$Ar(^3P_2)$	TDL (811.5 nm)	Coaxial DBD Jet		100 ns	Relative			TDLAS	[111]
$Ar(^3P_2)$	TDL (811.5 nm)	Co-axial RF jet		3 ns	$10^{10}–10^{11}$ cm^{-3}			TDLAS	[108]
$He(2^3S_1)$	TDL (1083 nm)	Planar RF jet	1 mm		$10^{9}–10^{11}$ cm^{-3}			TDLAS	[107, 214, 215]
$He(2^3S_1)$	TDL (1083 nm)	Planar RF jet	30 mm		$10^{9}–10^{10}$ cm^{-3}	1.0×10^{9} cm^{-3}		TDLAS	[114]
$He(2^3S_1)$	TDL (1083 nm)	Bipolar pulsed kHz jet			$10^{9}–10^{11}$ cm^{-3}			TDLAS	[113]
$He(2^3S_1)$	TDL (1083 nm)	Co-axial pulsed kHz jet		3 ns	$10^{11}–10^{13}$ cm^{-3}			TDLAS	[112, 213]
$He(2^3S_1)$	TDL (1083 nm)	Co-axial RF jet		3 ns	$10^{11}–10^{13}$ cm^{-3}	2.0×10^{11} cm^{-3}		TDLAS	[99]

regions of the plasma jet, even in areas that are not accessible by optical diagnostics [267]. All these examples show that QCLAS opens up the way for advanced monitoring and controlling of the production rates of relevant reactive molecules in plasma jets.

4. Comparison of different experiments

In the following table, above described examples on jet diagnostics are listed according to the studied species. The light source used, the plasma source studied and the experimental parameters, such as the absorption length, the time resolution, the density measured and the error or the detection limit are indicated. With this table, a quick overview is given for the possibilities of absorption spectroscopy on cold atmospheric plasma jets.

5. Summary and conclusion

Cold atmospheric plasma jets are at the focus of the attention due to exciting applications such as plasma medicine. For a fundamental study of plasma induced processes—e.g. in the interaction with biological systems—a detailed analysis of particle fluxes is mandatory. Several diagnostic techniques can yield this information at considerable technical and data analysis effort. One diagnostic technique that has to rely less on technical and analytical power is absorption spectroscopy. Due to its simplicity and reliability AS poses a diagnostic method that is suited excellently for absolute diagnostics of atmospheric pressure plasmas including atmospheric plasma jets. In this review, the fundamental aspects of atomic and molecular absorption, the application of Beer–Lambert Law, and how to derive population densities have been described. Special focus was set on lineshape and broadening mechanisms as these can yield valuable information on the studied species.

This review on absorption spectroscopy of atmospheric plasma jets in the special issue cluster 'Best practices for atmospheric pressure plasma diagnostics' presents a best practice approach and introduces databases and tools as well as techniques for spatial and time resolution and for sensitivity enhancement.

The present status of atmospheric plasma jet absorption spectroscopy is described in an extensive example section. Additionally to absorption spectroscopy on jet-like atmospheric pressure plasmas, other special techniques are introduced that have been used on non-jet-like or low pressure plasmas but are also excellently suitable for plasma jet diagnostics. Absorption spectroscopy was presented from VUV to MIR spectral range. The review closed with a tabulated list of the presented measurement examples sorted by the species studied.

For a deep understanding of reactive species generation and transport mechanisms that is required for present and future plasma applications, not only knowledge about species fluxes, requiring the determination of particle densities and velocities, but also radiative fluxes, local fluid temperatures, internal energies and energy branching ratios need to be determined. This enormous task can only be handled, if a combination of different complementary techniques providing special and temporal information is applied together with absorption spectroscopy determining absolute species densities. The aim is to be able to perform simultaneous highly space and time resolved measurements necessary for highly dynamic atmospheric plasma jets in turbulent gas flow situations.

Present studies have shown that a sensitivity enhancement is possible by implementation of heterodyne detection, cavity based methods and multi pass approaches. The increase in detector sensitivity combined with more stable and better to focus light sources and fast acquisition technology will allow to study lower species concentrations in smaller atmospheric plasma jets.

In summary, absorption spectroscopy has found its way into cold atmospheric plasma jet diagnostics and will help to understand complex interaction mechanisms for a broad range of novel applications.

Acknowledgment

The authors thank COST MP1101 for establishing this special issue cluster. Acknowledgment also goes to K-D Weltmann for support and discussion.

References

[1] Iza F, Kim G J, Lee S M, Lee J K, Walsh J L, Zhang Y T and Kong M G 2008 Microplasmas: sources, particle kinetics, and biomedical applications *Plasma Process. Polym.* **5** 322–44

[2] Léveillé V and Coulombe S 2005 Design and preliminary characterization of a miniature pulsed RF APGD torch with downstream injection of the source of reactive species *Plasma Sources Sci. Technol.* **14** 467–76

[3] Schutze A, Jeong J Y, Babayan S E, Jaeyoung P, Selwyn G S and Hicks R F 1998 The atmospheric-pressure plasma jet: a review and comparison to other plasma sources *IEEE Trans. Plasma Sci.* **26** 1685–94

[4] Stoffels E, Flikweert A J, Stoffels W W and Kroesen G M W 2002 Plasma needle: a non-destructive atmospheric plasma source for fine surface treatment of (bio)materials *Plasma Sources Sci. Technol.* **11** 383–8

[5] Niemi K, Reuter S, Schaper L, Knake N, Gathen V S-V D and Gans T 2007 Diagnostics on an atmospheric pressure plasma jet *J. Phys. D: Conf. Ser.* **71** 012012

[6] Reuter S, Niemi K, Schulz-von der Gathen V and Döbele H F 2009 Generation of atomic oxygen in the effluent of an atmospheric pressure plasma jet *Plasma Sourc. Sci. Technol.* **18** 015006

[7] von Woedtke T, Reuter S, Masur K and Weltmann K D 2013 Plasmas for medicine *Phys. Rep.* **530** 291–320

[8] Graves D B 2014 Low temperature plasma biomedicine: a tutorial review *Phys. Plasmas* **21** 080901

[9] Machala Z, Chládeková L and Pelach M 2010 Plasma agents in bio-decontamination by dc discharges in atmospheric air *J. Phys. D: Appl. Phys.* **43** 222001

[10] Reuter S, Tresp H, Wende K, Hammer M U, Winter J, Masur K, Schmidt-Bleker A and Weltmann K-D 2012 From RONS to ROS: tailoring plasma jet treatment of skin cells *IEEE Trans. Plasma Sci.* **40** 2986–93

[11] Weltmann K-D, Polak M, Masur K, Woedtke T V, Winter J and Reuter S 2012 Plasma processes and plasma sources in medicine *Control. Plasma Phys.* **52** 644–54

[12] Dilecce G 2014 Optical spectroscopy diagnostics of discharges at atmospheric pressure *J. Phys. D*: *Appl. Phys.* **23** 015011

[13] Mondello L, Tranchida P Q, Dugo P and Dugo G 2008 Comprehensive 2D gas chromatography-mass spectrometry: a review *Mass Spectrom. Rev.* **27** 101–24

[14] Laux C O, Spence T G, Kruger C H and Zare R N 2003 Optical diagnostics of atmospheric pressure air plasmas *Plasma Sourc. Sci. Technol.* **12** 125–38

[15] Sadeghi N 2004 Molecular spectroscopy techniques applied for processing plasma diagnostics *J. Plasma Fusion Res.* **80** 767–76

[16] Schulz-von der Gathen V, Schaper L, Knake N, Reuter S, Niemi K, Gans T and Winter J 2008 Spatially resolved diagnostics on a microscale atmospheric pressure plasma jet *J. Phys. D: Appl. Phys.* **41** 194004

[17] Šimek M 2014 Optical diagnostics of streamer discharges in atmospheric gases *J. Phys. D: Appl. Phys.* **47** 463001

[18] Stancu G D, Kaddouri F, Lacoste D A and Laux C O 2010 Atmospheric pressure plasma diagnostics by OES, CRDS and TALIF *J. Phys. D: Appl. Phys.* **43** 124002

[19] Bruggeman P and Brandenburg R 2013 Atmospheric pressure discharge filaments and microplasmas: physics, chemistry and diagnostics *J. Phys. D: Appl. Phys.* **46** 464001

[20] Fantz U 2006 Basics of plasma spectroscopy *Plasma Sources Sci. Technol.* **15** S137–47

[21] Verreycken T, van der Horst R M, Sadeghi N and Bruggeman P J 2013 Absolute calibration of OH density in a nanosecond pulsed plasma filament in atmospheric pressure He–H_2O: comparison of independent calibration methods *J. Phys. D: Appl. Phys.* **46**

[22] Benedikt J, Ellerweg D and von Keudell A 2009 Molecular beam sampling system with very high beam-to-background ratio: the rotating skimmer concept *Rev. Sci. Instrum.* **80** 055107

[23] Dünnbier M, Schmidt-Bleker A, Winter J, Wolfram M, Hippler R, Weltmann K D and Reuter S 2013 Ambient air particle transport into the effluent of a cold atmospheric-pressure argon plasma jet investigated by molecular beam mass spectrometry *J. Phys. D: Appl. Phys.* **46** 435203

[24] Bruggeman P J, Sadeghi N, Schram D C and Linss V 2014 Gas temperature determination from rotational lines in non-equilibrium plasmas: a review *Plasma Sourc. Sci. Technol.* **23** 023001

[25] Capitelli M, Ferreira C M, Gordiets B F and Osipov A I 2000 *Plasma Kinetics in Atmospheric Gases* vol 31 (New York: Springer)

[26] Stancu G D 2014 Laser based spectroscopic diagnostics from UV to Mid-IR applied to the study of atmospheric pressure discharges *Spectroscopy and Spectroscopic: Measurement Techniques for Aerospace Flows* ed D Giordano and Y Babou (Belgium: Von Karman Institute for Fluid Dynamics)

[27] Niemi K, Reuter S, Schaper L, Knake N, Gathen V S-V D and Gans T 2007 Diagnostics on an atmospheric pressure plasma jet *J. Phys.: Conf. Ser.* **71** 012012

[28] Dilecce G, Ambrico P F, Simek M and Benedictis S D 2012 OH density measurement by time-resolved broad band absorption spectroscopy in an Ar–H_2O dielectric barrier discharge *J. Phys. D: Appl. Phys.* **45** 125203

[29] Demtröder W 2008 *Laser Spectroscopy Vol. 1: Basic Principles* (Berlin: Springer)

[30] Griem H R 1964 *Plasma Spectroscopy* (New York: McGraw-Hill)

[31] Kunze H J 2009 *Introduction to Plasma Spectroscopy* vol 56 (Berlin: Springer)

[32] Hilborn R C 1982 Einstein coefficients, cross sections, *f* values, dipole moments, and all that *Am. J. Phys.* **50** 982

[33] Sadeghi N 2014 Diagnostics des plasmas par absorption optique; de Mitchell et Zemansky à la CRDS jrpf2014.sciencesconf.org/48557/document

[34] Kramida A, Ralchenko Y, Reader J and 'NIST-ASD-Team' 2014 *NIST Atomic Spectra Database (Version 5.2)* www.nist.gov/pml/data/asd.cfm, Accessed: 2015, Last Update: September 2014

[35] Rothman L S *et al* 1998 The Hitran molecular spectroscopic database and Hawks (Hitran atmospheric workstation): 1996 edition *J. Quant. Spectrosc. Radiat. Transfer* **60** 665–710

[36] Herzberg G 1989 *Molecular Spectra and Molecular Structure* vol 1–3 (Malabar, FL: Krieger) (Reprint)

[37] Stancu G D, Ropcke J and Davies P B 2005 Line strengths and transition dipole moment of the nu_2 fundamental band of the methyl radical *J. Chem. Phys.* **122** 14306

[38] Rothman L S 2014 The Hitran database www.cfa.harvard.edu/hitran/, Accessed: 2014, Last Update: 11 October 2013

[39] Rothman L S *et al* 2013 The HITRAN2012 molecular spectroscopic database *J. Quant. Spectrosc. Radiat. Transfer* **130** 4–50

[40] Welzel S, Stepanov S, Meichsner J and Röpcke J 2009 Application of quantum cascade laser absorption spectroscopy to studies of fluorocarbon molecules *J. Phys. Conf. Ser.* **157** 012010

[41] Nikiforov A Y, Leys C, Gonzalez M A and Walsh J L 2015 Electron density measurement in atmospheric pressure plasma jets: Stark broadening of hydrogenated and non-hydrogenated lines *Plasma Sources Sci. Technol.* **24** 034001

[42] Hubner S, Sadeghi N, Carbone E A D and van der Mullen J J A M 2013 Density of atoms in Ar*(3p(5)4s) states and gas temperatures in an argon surfatron plasma measured by tunable laser spectroscopy *J. Appl. Phys.* **113**

[43] Penache C, Miclea M, Bräuning-Demian A, Hohn O, Schössler S, Jahnke T, Niemax K and Schmidt-Böcking H 2002 Characterization of a high-pressure microdischarge using diode laser atomic absorption spectroscopy *Plasma Sources Sci. Technol.* **11** 476–83

[44] Olivero J J and Longbothum R L 1977 Empirical fits to the Voigt line width: a brief review *J. Quant. Spectrosc. Radiat. Transfer* **17** 233–6

[45] Whiting E E 1968 An empirical approximation to the Voigt profile *J. Quant. Spectrosc. Radiat. Transfer* **8** 1379–84

[46] Kogelschatz M, Cunge G and Sadeghi N 2004 Identification of halogen containing radicals in silicon etching plasmas and density measurement by UV broad band absorption spectroscopy *J. Phys. D: Appl. Phys.* **37** 1954–64

[47] Bruggeman P, Cunge G and Sadeghi N 2012 Absolute OH density measurements by broadband UV absorption in diffuse atmospheric-pressure He-H_2O RF glow discharges *Plasma Sourc. Sci. Technol.* **21** 035019

[48] SpectralFit 2014 SpecAir www.specair-radiation.net, Accessed: 2015, Last Update: 2012

[49] SRI International 2014 LIFBASE Spectroscopy Tool www.sri.com/engage/products-solutions/lifbase, Accessed: 2014, Last Update: n.n

[50] Letzgus M 2011 *LASKIN a LIF Simulation Programm* www.uni-bielefeld.de/chemie/arbeitsbereiche/pc1-kohse/forschung/spektroskopie/laskinv2.html, Accessed: 2014, Last Update: 19 July 2012

[51] Control N Q-MACSoft-HT online available: www.neoplas-control.de/, Accessed: Last Update

[52] Sharpe S 2014 PNNL Northwest-Infrared vapor phase infrared spectral library https://secure2.pnl.gov/nsd/nsd.nsf/Welcome, Accessed: 2014, Last Update: n.n

[53] Keller-Rudek H, Moortgat G K, Sander R and Sörensen R 2013 The MPI-Mainz UV/VIS spectral atlas of gaseous molecules of atmospheric interest *Earth Syst. Sci. Data* **5** 365–73

[54] Keller-Rudek H, Moortgat G K, Sander R and Sörensen R 2014 The MPI-Mainz UV/VIS spectral atlas of gaseous molecules of atmospheric interest (www.uv-vis-spectral-atlas-mainz.org)

[55] Western C 2014 *PGOPHER a Program for Simulating Rotational Structure Version 8.0* http://pgopher.chm.bris.ac.uk/, Accessed: 2015, Last Update: January 2015

[56] Hübner M, Lang N, Zimmermann S, Schulz S E, Buchholtz W, Röpcke J and van Helden J H 2015 Quantum cascade laser based monitoring of CF_2 radical concentration as a diagnostic tool of dielectric etching plasma processes *Appl. Phys. Lett.* **106** 031102

[57] Hancock G, Horrocks S J, Ritchie G A, Helden J H and Walker R J 2008 Time-resolved detection of the CF3 photofragment using chirped QCL radiation *J. Phys. Chem.* A **112** 9751–7

[58] White J U 1942 Long optical paths of large aperture *J. Opt. Soc. Am.* **32** 285

[59] Herriott D R and Schulte H J 1965 Folded optical delay lines *Appl. Opt.* **4** 883

[60] Reuter S, Winter J, Iseni S, Peters S, Schmidt-Bleker A, Dünnbier M, Schäfer J, Foest R and Weltmann K-D 2012 Detection of ozone in a MHz argon plasma bullet jet *Plasma Sources Sci. Technol.* **21** 034015

[61] Pipa A V, Reuter S, Foest R and Weltmann K D 2012 Controlling the NO production of an atmospheric pressure plasma jet *J. Phys. D: Appl. Phys.* **45**

[62] Berden G and Engeln R 2009 *Cavity Ring-Down Spectroscopy: Techniques and Applications* (Chichester: Wiley-Blackwell)

[63] Gagliardi G and Loock H-P 2014 *Cavity-Enhanced Spectroscopy and Sensing* vol 179 (Heidelberg: Springer)

[64] Cunge G, Vempaire D, Touzeau M and Sadeghi N 2007 Broadband and time-resolved absorption spectroscopy with light emitting diodes: application to etching plasma monitoring *Appl. Phys. Lett.* **91**

[65] Niermann B, Budunoğlu I L, Gürel K, Böke M, Ilday F Ö and Winter J 2012 Application of a mode-locked fiber laser for highly time resolved broadband absorption spectroscopy and laser-assisted breakdown on micro-plasmas *J. Phys. D: Appl. Phys.* **45** 245202

[66] Röpcke J, Davies P, Lang N, Rousseau A and Welzel S 2012 Applications of quantum cascade lasers in plasma diagnostics: a review *J. Phys. D: Appl. Phys.* **45** 423001

[67] Morse F A and Kaufman F 1965 Determination of ground-state O, N, and H by light absorption and measurement of oscillator strengths *J. Chem. Phys.* **42** 1785

[68] Spaan M, Goehlich A, Gathen V S V D and Döbele. H F 1994 Experimental test of a novel Raman cell for vacuum ultraviolett generation to below Lyman-a *Appl. Opt.* **33** 3865

[69] Wagner D, Dikmen B and Dobele H F 1996 Vacuum ultraviolet absorption spectroscopy in the spectral interval of Lyman-alpha of atomic hydrogen and deuterium in an ion source plasma *Rev. Sci. Instrum.* **67** 1800–6

[70] Riordan J C 1980 Xuv absorption-spectroscopy of a backlighted aluminum plasma *Bull. Am. Phys. Soc.* **25** 916

[71] Riordan J C and Pearlman J S 1981 Extreme ultraviolet-absorption spectroscopy of a backlighted aluminum plasma *Appl. Phys. Lett.* **39** 543–5

[72] Bodart P, Brihoum M, Cunge G, Joubert O and Sadeghi N 2011 Analysis of pulsed high-density HBr and Cl-2 plasmas: impact of the pulsing parameters on the radical densities *J. Appl. Phys.* **110**

[73] Tada S, Takashima S, Ito M, Hori M, Goto T and Sakamoto Y 2000 Measurement and control of absolute nitrogen atom density in an electron-beam-excited plasma using vacuum ultraviolet absorption spectroscopy *J. Appl. Phys.* **88** 1756–9

[74] Kuwahara A, Matsui M and Yamagiwa Y 2012 Development of vacuum ultraviolet absorption spectroscopy system for wide measurement range of number density using a dual-tube inductively coupled plasma light source *Rev. Sci. Instrum.* **83**

[75] Booth J P, Joubert O, Pelletier J and Sadeghi N 1991 Oxygen atom actinometry reinvestigated—comparison with absolute measurements by resonance-absorption at 130 Nm *J. Appl. Phys.* **69** 618–26

[76] Cunge G, Bodart P, Brihoum M, Boulard F, Chevolleau T and Sadeghi N 2012 Measurement of free radical kinetics in pulsed plasmas by UV and VUV absorption spectroscopy and by modulated beam mass spectrometry *Plasma Sourc. Sci. Technol.* **21**

[77] Martini L M, Dilecce G, Scotoni M, Tosi P and Benedictis S D 2014 OH density measurements by time-resolved broad band absorption spectroscopy in a He–H_2O dielectric barrier discharge with small O_2 addition *Plasma Process. Polym.* **11** 232–8

[78] Foucher M, Carbone E, Chabert P and Booth J P 2014, Inductively-coupled plasmas of Cl_2/O_2: measurements of atoms, Cl_xO_y and electron densities *Proc. of the XXII Europhysics Conf. on Atomic and Molecular Physics of Ionized Gases* (*Greifswald, Germany*)

[79] Mitchell A C G and Zemansky M W 2009 *Resonance Radiation and Excited Atoms* (Cambridge: Cambridge University Press)

[80] Sadeghi N 2014 private communication

[81] Li L, Nikiforov A, Britun N, Snyders R and Leys C 2015 Emission and absorption spectroscopy study of Ar excited states in 13.56 MHz argon plasma operating at sub-atmospheric to atmospheric pressure *Spectrochim. Acta* B **107** 75–85

[82] Castaños-Martínez E and Moisan M 2010 Absorption spectroscopy measurements of resonant and metastable atom densities in atmospheric-pressure discharges using a low-pressure lamp as a spectral-line source and comparison with a collisional-radiative model *Spectrochim. Acta* B **65** 199–209

[83] Yariv A and Yeh P 2006 *Photonics: Optical Electronics in Modern Communications* (Oxford: Oxford University Press)

[84] Supplee J M, Whittaker E A and Lenth W 1994 Theoretical description of frequency modulation and wavelength modulation spectroscopy *Appl. Opt.* **33** 6294–302

[85] Liger V, Zybin A, Kuritsyn Y and Niemax K 1997 Diode-laser atomic-absorption spectrometry by the double-beam—double-modulation technique *Spectrochim. Acta* B **52** 1125–38

[86] Franzke J, Stancu D G and Niemax K 2003 Measurements of sulfur compounds in CO_2 by diode laser atomic absorption spectrometry *Spectrochim. Acta* B **58** 1359–66

[87] Reid J and Labrie D 1981 Second-harmonic detection with tunable diode lasers? Comparison of experiment and theory *Appl. Phys.* B **26** 203–10

[88] Stancu G D 2014 Laser based spectroscopic diagnostics for fundamentals and applications of reactive plasmas University of Paris Sud, France

[89] Kluczynski P, Gustafsson J, Lindberg Å M and Axner O 2001 Wavelength modulation absorption spectrometry—an extensive scrutiny of the generation of signals *Spectrochim. Acta* B **56** 1277–354

[90] Cassidy D T and Reid J 1982 Atmospheric pressure monitoring of trace gases using tunable diode lasers *Appl. Opt.* **21** 1185–90

[91] Kluczynski P, Lindberg Å M and Axner O 2001 Background signals in wavelength-modulation spectrometry with frequency-doubled diode-laser light. I. theory *Appl. Opt.* **40** 770–82

[92] Rogoff G L 1985 Optical probe for spatially resolved plasma emission and absorption-spectroscopy *Appl. Opt.* **24** 1733–5
[93] Hughey B J and Santavicca D A 2007 A comparison of techniques for reconstructing axisymmetric reacting flow fields from absorption measurements *Combust. Sci. Technol.* **29** 167–90
[94] Santoro R J, Semerjan H G, Emmerman P J and Gouldard R 1981 Optical tomography for flow field diagnostics *Int. J. Heat Mass Transfer* **24** 1139–50
[95] Reuter S 2008 *Formation Mechanisms of Atomic Oxygen in an Atmospheric Pressure Plasma Jet Characterised by Spectroscopic Methods* (Göttingen: Cuvillier)
[96] Schulz-von der Gathen V, Buck V, Gans T, Knake N, Niemi K, Reuter S, Schaper L and Winter J 2007 Optical diagnostics of micro discharge jets *Control. Plasma Phys.* **47** 510–9
[97] Walsh K T, Fielding J and Long M B 2000 Effect of light-collection geometry on reconstruction errors in Abel inversions *Opt. Lett.* **25** 457–9
[98] Luque J, Juchmann W, Brinkman E A and Jeffries J B 1998 Excited state density distributions of H, C, C_2, and CH by spatially resolved optical emission in a diamond depositing dc-arcjet reactor *J. Vac. Sci. Technol.* A **16** 397–408
[99] Winter J, Sousa J S, Sadeghi N, Schmidt-Bleker A, Reuter S and Puech V 2015 The spatio-temporal distribution of He (2^3S_1) metastable atoms in a MHz-driven helium plasma jet is influenced by the oxygen/nitrogen ratio of the surrounding atmosphere *Plasma Sources Sci. Technol.* **24** 025015
[100] Winter J, Dunnbier M, Schmidt-Bleker A, Meshchanov A, Reuter S and Weltmann K D 2012 Aspects of UV-absorption spectroscopy on ozone in effluents of plasma jets operated in air *J. Phys. D: Appl. Phys.* **45**
[101] Schmidt-Bleker A, Reuter S and Weltmann K D 2015 Quantitative schlieren diagnostics for the determination of ambient species density, gas temperature and calorimetric power of cold atmospheric plasma jets *J. Phys. D: Appl. Phys.* **48** 175202
[102] Buuron A J M, Otorbaev D K, Vandesanden M C M and Schram D C 1994 Absorption-spectroscopy on the argon 1st excited-state in an expanding thermal arc plasma *Phys. Rev.* E **50** 1383–93
[103] Flikweert A J, Meunier A F, Nimalasuriya T, Kroesen G M W and Stoffels W W 2008 Imaging laser absorption spectroscopy of the metal-halide lamp under hyper-gravity conditions ranging from 1 to 10 g *J. Phys. D: Appl. Phys.* **41** 195202
[104] Moskowitz P E 1987 Novel laser diagnostic for mercury rare gas low pressure discharges *Appl. Phys. Lett.* **50** 891
[105] Stancu G D, Ropcke J and Davies P B 2008 Measurement of the transition dipole moment of the first hot band of the nu2 mode of the methyl radical by diode laser spectroscopy *J. Phys. Chem.* A **112** 6285–8
[106] Vitelaru C, Lundin D, Stancu G D, Brenning N, Bretagne J and Minea T 2012 Argon metastables in HiPIMS: time-resolved tunable diode-laser diagnostics *Plasma Sources Sci. Technol.* **21** 025010
[107] Niermann B, Boke M, Sadeghi N and Winter J 2010 Space resolved density measurements of argon and helium metastable atoms in radio-frequency generated He-Ar micro-plasmas *Eur. Phys. J.* D **60** 489–95
[108] Schmidt-Bleker A, Winter J, Tresp H, Sousa J S, Puech V, Weltmann K D and Reuter S 2014 The influence of shielding gas composition on the dynamics, temperature and reactive species generated by a cold atmospheric pressure plasma jet with gas shielding device *XXII Europhysics Conf. on Atomic and Molecular Physics of Ionized Gases (Greifswald, Germany, 15–19 July 2014)*
[109] Schröter S, Pothiraja R, Awakowicz P, Bibinov N, Böke M, Niermann B and Winter J 2013 Time-resolved characterization of a filamentary argon discharge at atmospheric pressure in a capillary using emission and absorption spectroscopy *J. Phys. D: Appl. Phys.* **46** 464009
[110] Niermann B, Reuter R, Kuschel T, Benedikt J, Boke M and Winter J 2012 Argon metastable dynamics in a filamentary jet micro-discharge at atmospheric pressure *Plasma Sourc. Sci. Technol.* **21** 034002
[111] Bussiahn R, Kindel E, Lange H and Weltmann K D 2010 Spatially and temporally resolved measurements of argon metastable atoms in the effluent of a cold atmospheric pressure plasma jet *J. Phys. D: Appl. Phys.* **43** 165201
[112] Claire D 2014 Étude d'un micro-jet de plasma à pression atmosphérique *PhD Thesis* Université Paris-Sud, Paris, France
[113] Urabe K, Morita T, Tachibana K and Ganguly B N 2010 Investigation of discharge mechanisms in helium plasma jet at atmospheric pressure by laser spectroscopic measurements *J. Phys. D: Appl. Phys.* **43** 095201
[114] Niemi K, Waskoenig J, Sadeghi N, Gans T and O'Connell D 2011 The role of helium metastable states in radio-frequency driven helium-oxygen atmospheric pressure plasma jets: measurement and numerical simulation *Plasma Sourc. Sci. Technol.* **20**
[115] Bösel A, Ehlbeck J, König N, Salewski K-D and Röpcke J 2012 On enhanced tuning capabilities of external cavity lasers using acousto-optic modulators *Opt. Rev.* **19** 332–6
[116] Bösel A, Salewski K-D and Kinder T 2007 Fast mode-hop-free acousto-optically tuned laser with a simple laser diode *Opt. Lett.* **32** 1956
[117] Bösel A and Salewski K-D 2009 Fast mode-hop-free acousto-optically tuned laser: theoretical and experimental investigations *Appl. Opt.* **48** 818
[118] Winter J, Mussard M D V S, Bösel A, Ehlbeck J, Rousseau A and Reuter S 2014 Characterization of a low-pressure He–H_2 bullet discharge by laser atom absorption spectroscopy on Balmer Hα transition *ESCAMPIG XXII (Greifswald, Germany 15–19 July 2014)*
[119] Gousset G, Panafieu P, Touzeau M and Vialle M 1987 Experimental study of a d.c. oxygen glow discharge by V.U.V. absorption spectroscopy *Plasma Chem. Plasma Process.* **7** 409–27
[120] Frimer A A 1985 *Singlet Oxygen* (Boca Raton, FL: CRC Press)
[121] Pitts J N, Khan A U, Smith E B and Wayne R P 1969 Singlet oxygen in the environmental sciences. Singlet molecular oxygen and photochemical air pollution *Environ. Sci. Technol.* **3** 241–7
[122] Rabek J F and anby B 1975 Role of singlet oxygen in photo-oxidative degradation and photostabilization of polymers *Polym. Eng. Sci* **15** 40–3
[123] Starik A M and Titova N S 2001 Low-temperature initiation of the detonation combustion of gas mixtures in a supersonic flow under excitation of the O_2(a) *Dokl. Phys.* **46** 627
[124] McDermott W E, Pchelkin N R, Benard D and Bousek R 1978 An electronic transition chemical laser *Appl. Phys. Lett.* **32** 469
[125] Dougherty T J, Kaufman J E, Goldfarb A, Weishaupt K R, Boyle D and Mittleman A 1978 Photoradiation therapy for the treatment of malignant tumors *Cancer Res.* **38** 2628–35
[126] Ionin A A, Kochetov I V, Napartovich A P and Yuryshev N N 2007 Physics and engineering of singlet delta oxygen production in low-temperature plasma *J. Phys. D: Appl. Phys.* **40** R25–61
[127] Newman S M, Orr-Ewing A J, Newnham D A and Ballard J 2000 Temperature and pressure dependence

of line widths and integrated absorption intensities for the $O_2a^1\Delta_g - X_3\Sigma_g^-(0,0)$ transition *J. Phys. Chem.* A **104** 9467–80

[128] Sousa J S and Puech V 2013 Diagnostics of reactive oxygen species produced by microplasmas *J. Phys. D: Appl. Phys.* **46** 464005

[129] Sousa J S, Bauville G, Lacour B, Puech V, Touzeau M and Pitchford L C 2008 $O_2(a^1\Delta_g)$ production at atmospheric pressure by microdischarge *Appl. Phys. Lett.* **93** 011502

[130] Sousa J S, Bauville G and Puech V 2013 Arrays of microplasmas for the controlled production of tunable high fluxes of reactive oxygen species at atmospheric pressure *Plasma Sourc. Sci. Technol.* **22** 035012

[131] Sousa J S, Douat C, Bauville G, Fleury M and Puech V 2013 *Proc. of the 31st ICPIG (Granada, Spain, 14–19 July 2013)*

[132] Sousa J S, Niemi K, Cox L J, Algwari Q T, Gans T and O'Connell D 2011 Cold atmospheric pressure plasma jets as sources of singlet delta oxygen for biomedical applications *J. Appl. Phys.* **109** 123302

[133] Sousa J S, Hammer M U, Winter J, Tresp H, Duennbier M, Iseni S, Martin V, Puech V, Weltmann K D and Reuter S 2012 *Proc. of the 65th Gaseous Electronics Conf. (Austin Texas USA, 22–26 October, 2012)*

[134] Ogawa S and Ogawa M 1975 Absorption cross sections of $O_2(a^1\Delta_g)$ and $O_2(X_3\Sigma_g^-)$ in the region from 1087 to 1700 Å *Can. J. Phys.* **53** 1845–52

[135] Reuter S, Winter J, Schmidt-Bleker A, Schroeder D, Lange H, Knake N, Schulz-von der Gathen V and Weltmann K D 2012 Atomic oxygen in a cold argon plasma jet: TALIF spectroscopy in ambient air with modelling and measurements of ambient species diffusion *Plasma Sourc. Sci. Technol.* **21** 024005

[136] Coxon J A and Roychowdhury U K 1986 A spectrometric technique for monitoring $[O_2(a^1\Delta_g)]$ in the gas phase *Appl. Spectrosc.* **40** 203–9

[137] Laity G, Neuber A, Rogers G and Frank K 2010 System for time resolved spectral studies of pulsed atmospheric discharges in the visible to vacuum ultraviolet range *Rev. Sci. Instrum.* **81** 083103

[138] Laity G, Fierro A, Dickens J, Neuber A and Frank K 2013 Simultaneous measurement of nitrogen and hydrogen dissociation from vacuum ultraviolet self-absorption spectroscopy in a developing low temperature plasma at atmospheric pressure *Appl. Phys. Lett.* **102**

[139] Nagai H, Hiramatsu M, Hori M and Goto T 2003 Measurement of oxygen atom density employing vacuum ultraviolet absorption spectroscopy with microdischarge hollow cathode lamp *Rev. Sci. Instrum.* **74** 3453

[140] Niemi K, Gathen V S-V D and Döbele H F 2005 Absolute atomic oxygen density measurements by two-photon absorption laser-induced fluorescence spectroscopy in an RF-excited atmospheric pressure plasma jet *Plasma Sources Sci. Technol.* **14** 375–86

[141] Moravej M, Yang X, Hicks R F, Penelon J and Babayan S E 2006 A radio-frequency nonequilibrium atmospheric pressure plasma operating with argon and oxygen *J. Appl. Phys.* **99** 093305

[142] Schulz-von der Gathen V, Schaper L, Knake N, Reuter S, Niemi K, Gans T and Winter J 2008 Spatially resolved diagnostics on a microscale atmospheric pressure plasma jet *J. Phys. D: Appl. Phys.* **41** 194004

[143] Schmidt-Bleker A, Reuter S and Weltmann K-D 2014 Non-dispersive path mapping approximation for the analysis of ambient species diffusion in laminar jets *Phys. Fluids* **26** 083603

[144] Giapis K P, Sadeghi N, Margot J L, Gottscho R A and Lee T C J 1993 Limits to ion energy control in high density glow discharges: measurement of absolute metastable ion concentrations *J. Appl. Phys.* **73** 7188

[145] Wang Z-B, Sadeghi N, Tsankov T V and Pu Y-K 2013 The influence of the spatial nonuniformity on the measurement of $Ar^*(1s_5)$ density by the self-absorption technique *J. Phys. D: Appl. Phys.* **46** 475205

[146] Kitajima T, Nakano T and Makabe T 2006 Increased $O(^1D)$ metastable density in highly Ar-diluted oxygen plasmas *Appl. Phys. Lett.* **88** 091501

[147] Iseki S, Hashizume H, Jia F, Takeda K, Ishikawa K, Ohta T, Ito M and Hori M 2011 Inactivation of penicillium digitatum spores by a high-density ground-state atomic oxygen-radical source employing an atmospheric-pressure plasma *Appl. Phys. Express* **4** 116201

[148] Jia F, Ishikawa K, Takeda K, Kano H, Kularatne J, Kondo H, Sekine M and Hori M 2014 Spatiotemporal behaviors of absolute density of atomic oxygen in a planar type of Ar/O_2 non-equilibrium atmospheric-pressure plasma jet *Plasma Sources Sci. Technol.* **23** 025004

[149] Takeda K, Kato M, Jia F, Ishikawa K, Kano H, Sekine M and Hori M 2013 Effect of gas flow on transport of O (3Pj) atoms produced in ac power excited non-equilibrium atmospheric-pressure O_2/Ar plasma jet *J. Phys. D: Appl. Phys.* **46** 464006

[150] Fricke K, Reuter S, Schroder D, Schulz-von der Gathen V, Weltmann K-D and von Woedtke T 2012 Investigation of surface etching of poly(ether ether ketone) by atmospheric-pressure plasmas *IEEE Trans. Plasma Sci.* **40** 2900–11

[151] Niemi K, O'Connell D, de Oliveira N, Joyeux D, Nahon L, Booth J P and Gans T 2013 Absolute atomic oxygen and nitrogen densities in radio-frequency driven atmospheric pressure cold plasmas: synchrotron vacuum ultra-violet high-resolution Fourier-transform absorption measurements *Appl. Phys. Lett.* **103** 034102

[152] Daumont D, Brion J, Charbonnier J and Malicet J 1992 Ozone UV spectroscopy I: absorption cross-sections at room temperature *J. Atmos. Chem.* **15** 145–55

[153] Brion J, Chakir A, Daumont D, Malicet J and Parisse C 1993 High-resolution laboratory absorption cross section of O_3. Temperature effect *Chem. Phys. Lett.* **213** 610–2

[154] Malicet J, Daumont D, Charbonnier J, Parisse C, Chakir A and Brion J 1995 Ozone UV spectroscopy. II. Absorption cross-sections and temperature dependence *J. Atmos. Chem.* **21** 263–73

[155] Osborne B A, Marston G, Kaminski L, Jones N C, Gingell J M, Mason N, Walker I C, Delwiche J and Hubin-Franskin M J 2000 Vacuum ultraviolet spectrum of dinitrogen pentoxide *J. Quant. Spectrosc. Radiat. Transfer* **64** 67–74

[156] Yao F, Wilson I and Johnston H 1982 Temperature-dependent ultraviolet absorption spectrum for dinitrogen pentoxide *J. Phys. Chem.* **86** 3611–5

[157] Schürgers M and Welge K H 1968 Absorptionskoeffizient von H_2O_2 und N_2H_4 zwischen 1200 and 2000 Å *Z. Naturforsch.* **23a** 1508–10

[158] Nicovich J M and Wine P H 1988 Temperature-dependent absorption cross sections for hydrogen peroxide vapor *J. Geophys. Res.* **93** 2417

[159] Sander S P 1986 Temperature dependence of the nitrogen trioxide absorption spectrum *J. Phys. Chem.* **90** 4135–42

[160] Atkinson R, Baulch D L, Cox R A, Crowley J N, Hampson R F, Hynes R G, Jenkin M E, Rossi M J and Troe J 2004 Evaluated kinetic and photochemical data for atmospheric chemistry: volume I—gas phase reactions of O_x, HO_x, NO_x and SO_x species *Atmos. Chem. Phys.* **4** 1461–738

[161] Sander S P *et al* 2011 *Chemical Kinetics and Photochemical Data for Use in Atmospheric Studies, Evaluation No. 17 (JPL Publication 10–6)* (Pasadena, CA: Jet Propulsion Laboratory)
[162] Moiseev T, Misra N N, Patil S, Cullen P J, Bourke P, Keener K M and Mosnier J P 2014 Post-discharge gas composition of a large-gap DBD in humid air by UV–Vis absorption spectroscopy *Plasma Sources Sci. Technol.* **23** 065033
[163] Hegeler F and Akiyama H 1997 Spatial and temporal distributions of ozone after a wire-to-plate streamer discharge *IEEE Trans. Plasma Sci.* **25** 1158–65
[164] Park J, Henins I, Herrmann H W, Selwyn G S, Jeong J Y, Hicks R F, Shim D and Chang C S 2000 An atmospheric pressure plasma source *Appl. Phys. Lett.* **76** 288
[165] Jeong J Y, Park J, Henins I, Babayan S E, Tu V J, Selwyn G S, Ding G and Hicks R F 2000 Reaction chemistry in the afterglow of an oxygen – helium, atmospheric-pressure plasma *J. Phys. Chem.* A **104** 8027–32
[166] Kim Y, Park J, Rosocha L A, Teslow H L and Herrmann H W 2005 Measurements of dioxygen fluoride (O_2F) in an atmospheric pressure plasma jet *Appl. Phys. Lett.* **87** 011502
[167] Sousa J S, Bauville G, Lacour B, Puech V and Touzeau M 2009 Atmospheric pressure generation of $O_2(a^1\Delta_g)$ by microplasmas *Eur. Phys. J. Appl. Phys.* **47** 22807
[168] Molina L T and Molina M J 1986 Absolute absorption cross sections of ozone in the 185–350 nm wavelength range *J. Geophys. Res.* **91** 14501
[169] Ono R and Oda T 2004 Spatial distribution of ozone density in pulsed corona discharges observed by 2D laser absorption method *J. Phys. D: Appl. Phys.* **37** 730–5
[170] Ono R and Oda T 2003 Dynamics of ozone and OH radicals generated by pulsed corona discharge in humid-air flow reactor measured by laser spectroscopy *J. Appl. Phys.* **93** 5876
[171] Schafer J, Foest R, Reuter S, Kewitz T, Sperka J and Weltmann K D 2012 Laser schlieren deflectometry for temperature analysis of filamentary non-thermal atmospheric pressure plasma *Rev. Sci. Instrum.* **83** 103506
[172] Zhang S, van Gaens W, van Gessel B, Hofmann S, van Veldhuizen E, Bogaerts A and Bruggeman P 2013 Spatially resolved ozone densities and gas temperatures in a time modulated RF driven atmospheric pressure plasma jet: an analysis of the production and destruction mechanisms *J. Phys. D: Appl. Phys.* **46** 205202
[173] Dribinski V, Ossadtchi A, Mandelshtam V A and Reisler H 2002 Reconstruction of Abel-transformable images: the Gaussian basis-set expansion Abel transform method *Rev. Sci. Instrum.* **73** 2634
[174] Schroeder D, Bahre H, Knake N, Winter J, de los Arcos T and Schulz-von der Gathen V 2012 Influence of target surfaces on the atomic oxygen distribution in the effluent of a micro-scaled atmospheric pressure plasma jet *Plasma Source Sci. Technol.* **21**
[175] Winter J, Wende K, Masur K, Iseni S, Dunnbier M, Hammer M U, Tresp H, Weltmann K D and Reuter S 2013 Feed gas humidity: a vital parameter affecting a cold atmospheric-pressure plasma jet and plasma-treated human skin cells *J. Phys. D: Appl. Phys.* **46** 295401
[176] van Ham B T J, Hofmann S, Brandenburg R and Bruggeman P J 2014 *In situ* absolute air, O_3 and NO densities in the effluent of a cold RF argon atmospheric pressure plasma jet obtained by molecular beam mass spectrometry *J. Phys. D: Appl. Phys.* **47** 224013
[177] Eliasson B and Kogelschatz U 1991 Modeling and applications of silent discharge plasmas *IEEE Trans. Plasma Sci.* **19** 309–23
[178] Waskoenig J, Niemi K, Knake N, Graham L M, Reuter S, Schulz-von der Gathen V and Gans T 2010 Atomic oxygen formation in a radio-frequency driven micro-atmospheric pressure plasma jet *Plasma Sourc. Sci. Technol.* **19** 045018
[179] Shimizu T, Sakiyama Y, Graves D B, Zimmermann J L and Morfill G E 2012 The dynamics of ozone generation and mode transition in air surface micro-discharge plasma at atmospheric pressure *New J. Phys* **14** 103028
[180] Matthes R, Bender C, Schluter R, Koban I, Bussiahn R, Reuter S, Lademann J, Weltmann K D and Kramer A 2013 Antimicrobial efficacy of two surface barrier discharges with air plasma against *in vitro* biofilms *PLoS One* **8** e70462
[181] Gaunt L F, Beggs C B and Georghiou G E 2006 Bactericidal action of the reactive Species produced by gas-discharge nonthermal plasma at atmospheric pressure: a review *IEEE Trans. Plasma Sci.* **34** 1257–69
[182] Kosak-Channing L F and Helz G R 1983 Solubility of ozone in aqueous solutions of 0–0.6 M ionic strength at 5–30 °C *Environ. Sci. Technol.* **17** 145–9
[183] Winter J *et al* 2014 Tracking plasma generated H_2O_2 from gas into liquid phase and revealing its dominant impact on human skin cells *J. Phys. D: Appl. Phys.* **47** 285401
[184] Cheng C, Peng L, Lei X, Li-Ye Z, Ru-Juan Z and Wen-Rui Z 2006 Development of a new atmospheric pressure cold plasma jet generator and application in sterilization *Chin. Phys.* **15** 1544–8
[185] Chang H-W, Hsu C-C, Ahmed M, Liu S Y, Fang Y, Seog J, Oehrlein G S and Graves D B 2014 Plasma flux-dependent lipid a deactivation *J. Phys. D: Appl. Phys.* **47** 224015
[186] Han X, Klas M, Liu Y, Sharon Stack M and Ptasinska S 2013 DNA damage in oral cancer cells induced by nitrogen atmospheric pressure plasma jets *Appl. Phys. Lett.* **102** 233703
[187] O'Connell D, Cox L J, Hyland W B, McMahon S J, Reuter S, Graham W G, Gans T and Currell F J 2011 Cold atmospheric pressure plasma jet interactions with plasmid DNA *Appl. Phys. Lett.* **98** 043701
[188] Radi R, Beckman J S, Bush K M and Freeman B A 1991 Peroxynitrite-induced membrane lipid peroxidation: the cytotoxic potential of superoxide and nitric oxide *Arch. Biochem. Biophys.* **288** 481–7
[189] Van der Paal J, Aernouts S, van Duin A C T, Neyts E C and Bogaerts A 2013 Interaction of O and OH radicals with a simple model system for lipids in the skin barrier: a reactive molecular dynamics investigation for plasma medicine *J. Phys. D: Appl. Phys.* **46** 395201
[190] Hammer M U, Forbrig E, Kupsch S, Weltmann K-D and Reuter S 2013 IInfluence of plasma treatment on the structure and function of lipids *Plasma Med.* **3** 97–114
[191] Pavlovich M J, Clark D S and Graves D B 2014 Quantification of air plasma chemistry for surface disinfection *Plasma Sources Sci. Technol.* **23** 065036
[192] Bogdan C, Röllinghoff M and Diefenbach A 2000 Reactive oxygen and reactive nitrogen intermediates in innate and specific immunity *Curr. Opin. Immunol.* **12** 64–76
[193] Walsh J L and Kong M G 2008 Contrasting characteristics of linear-field and cross-field atmospheric plasma jets *Appl. Phys. Lett.* **93** 111501
[194] Packan D, Laux C O, Gessman R J, Pierrot L and Kruger C H 2003 Measurement and Modeling of OH, NO, and CO_2 infrared radiation at 3400 K *J. Thermophys. Heat Transfer* **17** 450–6
[195] Ono R and Oda T 2008 Measurement of gas temperature and OH density in the afterglow of pulsed positive corona discharge *J. Phys. D: Appl. Phys.* **41** 035204

[196] Vorac J, Dvorak P, Prochazka V, Ehlbeck J and Reuter S 2013 Measurement of hydroxyl radical (OH) concentration in an argon RF plasma jet by laser-induced fluorescence *Plasma Sourc. Sci. Technol.* **22** 025016
[197] Dilecce G, Ambrico P F, Simek M and De Benedictis S 2012 LIF diagnostics of hydroxyl radical in atmospheric pressure He–H_2O dielectric barrier discharges *Chem. Phys.* **398** 142–7
[198] Tochikubo F, Uchida S and Watanabe T 2004 Study on decay characteristics of OH radical density in pulsed discharge in Ar/H_2O *Japan. J. Appl. Phys.* **43** 315–20
[199] Nikiforov A, Xiong Q, Britun N, Snyders R, Lu X P and Leys C 2011 Absolute concentration of OH radicals in atmospheric pressure glow discharges with a liquid electrode measured by laser-induced fluorescence spectroscopy *App. Phys. Express* **4** 026102
[200] Nikiforov A, Li L, Britun N, Snyders R, Vanraes P and Leys C 2014 Influence of air diffusion on the OH radicals and atomic O distribution in an atmospheric Ar (bio) plasma jet *Plasma Sources Sci. Technol.* **23** 015015
[201] Verreycken T, Mensink R, van der Horst R, Sadeghi N and Bruggeman P J 2013 Absolute OH density measurements in the effluent of a cold atmospheric-pressure Ar-H2O RF plasma jet in air *Plasma Sourc. Sci. Technol.* **22**
[202] Iseni S, Reuter S, Schmidt-Bleker A and Weltmann K-D 2014 Flow and discharge development in an argon atmospheric pressure plasma Jet observed by ICCD and PLIF imaging *IEEE Trans. Plasma Sci.* **42** 2458–9
[203] Iseni S, Schmidt-Bleker A, Winter J, Weltmann K D and Reuter S 2014 Atmospheric pressure streamer follows the turbulent argon air boundary in a MHz argon plasma jet investigated by OH-tracer PLIF spectroscopy *J. Phys. D: Appl. Phys.* **47** 152001
[204] Bird P F and Schott G L 1965 Quantitative line absorption spectrophotometry: absorbance of the OH radical near 3090 Å *J. Quant. Spectrosc. Radiat. Transfer* **5** 783–4
[205] Srivastava N and Wang C 2011 Determination of OH radicals in an atmospheric pressure helium microwave plasma jet *IEEE Trans. Plasma Sci.* **39** 918–24
[206] Hibert C, Gaurand I, Motret O and Pouvesle J M 1999 [OH_X] measurements by resonant absorption spectroscopy in a pulsed dielectric barrier discharge *J. Appl. Phys.* **85** 7070
[207] Lempert W R 1988 Microwave resonance lamp absorption technique for measuring temperature and OH number density in combustion environments *Combust. Flame* **73** 89–98
[208] Gerling T 2014 Beiträge zur optischen und elektrischen Charakterisierung des dynamischen Verhaltens von Plasmaspezies in Atmosphärendruck-Plasmen Ernst-Moritz-Arndt-Universität Greifswald, Greifswald
[209] Triki M, Cermak P, Méjean G and Romanini D 2008 Cavity-enhanced absorption spectroscopy with a red LED source for NOx trace analysis *Appl. Phys.* B **91** 195–201
[210] Bekeschus S, Iseni S, Reuter S, Masur K and Weltmann K-D 2015 Nitrogen shielding of an argon plasma jet and Its effects on human immune cells *IEEE Trans. Plasma Sci.* **43** 776–81
[211] Simek M 2003 Determination of N_2(A 3 u) metastable density produced by nitrogen streamers at atmospheric pressure: 1. Design of diagnostic method *Plasma Sources Sci. Technol.* **12** 421–31
[212] Stancu G D, Janda M, Kaddouri F, Lacoste D A and Laux C O 2010 Time-resolved CRDS measurements of the N_2(A3Sigma(u)+) density produced by nanosecond discharges in atmospheric pressure nitrogen and air *J. Phys. Chem.* A **114** 201–8
[213] Cadot G, Douat C, Puech V and Sadeghi N 2014 Spatio-temporally resolved mapping of helium metastable density in an atmospheric pressure plasma jet *IEEE Trans. Plasma Sci.* **42** 2446–7
[214] Niermann B, Hemke T, Babaeva N Y, Böke M, Kushner M J, Mussenbrock T and Winter J 2011 Spatial dynamics of helium metastables in sheath or bulk dominated rf micro-plasma jets *J. Phys. D: Appl. Phys.* **44** 485204
[215] Niermann B, Kanitz A, Böke M and Winter J 2011 Impurity intrusion in radio-frequency micro-plasma jets operated in ambient air *J. Phys. D: Appl. Phys.* **44** 325201
[216] Reuter S, Schmidt-Bleker A, Iseni S, Winter J and Weltmann K-D 2014 On the bullet-streamer dualism *IEEE Trans. Plasma Sci.* **42** 2428–9
[217] Schäfer J, Foest R, Quade A, Ohl A and Weltmann K D 2008 Local deposition of SiO_x plasma polymer films by a miniaturized atmospheric pressure plasma jet (APPJ) *J. Phys. D: Appl. Phys.* **41** 194010
[218] Peters S, Andrasch M, Schafer J, Foest R, Reuter S and Weltmann K-D 2014 Phase-resolved spectroscopy synchronized to low-frequency self-organized mode of an atmospheric pressure plasma jet *IEEE Trans. Plasma Sci.* **42** 2462–3
[219] Hübner S, Sousa J S, Puech V, Kroesen G M W and Sadeghi N 2014 Electron properties in an atmospheric helium plasma jet determined by Thomson scattering *J. Phys. D: Appl. Phys.* **47** 432001
[220] Adamek P, Olejnicek J, Cada M, Kment S and Hubicka Z 2013 Time-resolved tunable diode laser absorption spectroscopy of pulsed plasma *Opt. Lett.* **38** 2428–30
[221] Reuter S, Winter J, Schmidt-Bleker A, Tresp H, Hammer M U and Weltmann K-D 2012 Controlling the ambient air affected reactive species composition in the effluent of an argon plasma jet *IEEE Trans. Plasma Sci.* **40** 2788–94
[222] Jablonowski H, Hansch M A, Dunnbier M, Wende K, Hammer M U, Weltmann K D, Reuter S and Woedtke T 2015 Plasma jet's shielding gas impact on bacterial inactivation *Biointerphases* **10** 029506
[223] Schmidt-Bleker A, Norberg S A, Winter J, Johnsen E, Reuter S, Weltmann K and Kushner M J 2015 Propagation mechanisms of guided streamers in plasma jets: the influence of electronegativity of the surrounding gas *Plasma Sources Sci. Technol.* (Provisionally scheduled for May 2015)
[224] Bacsik Z, Mink J and Keresztury G 2004 FTIR spectroscopy of the atmosphere. I. Principles and methods *Appl. Spectrosc. Rev.* **39** 295–363
[225] Bacsik Z, Mink J and Keresztury G 2005 FTIR spectroscopy of the atmosphere part 2. Applications *Appl. Spectrosc. Rev.* **40** 327–90
[226] Laroche G, Vallade J, Bazinette R, van Nijnatten P, Hernandez E, Hernandez G and Massines F 2012 Fourier transform infrared absorption spectroscopy characterization of gaseous atmospheric pressure plasmas with 2 mm spatial resolution *Rev. Sci. Instrum.* **83** 103508
[227] Khacef A, Cormier J M and Pouvesle J M 2002 NO_x remediation in oxygen-rich exhaust gas using atmospheric pressure non-thermal plasma generated by a pulsed nanosecond dielectric barrier discharge *J. Phys. D: Appl. Phys.* **35** 1491–8
[228] Kim H-H, Ogata A and Futamura S 2005 Atmospheric plasma-driven catalysis for the low temperature decomposition of dilute aromatic compounds *J. Phys. D: Appl. Phys.* **38** 1292–300
[229] Schmidt M, Basner R and Brandenburg R 2012 Hydrocarbon assisted NO oxidation with non-thermal plasma in simulated marine diesel exhaust gases *Plasma Chem. Plasma Process.* **33** 323–35

[230] Oehmigen K, Winter J, Hähnel M, Wilke C, Brandenburg R, Weltmann K-D and von Woedtke T 2011 Estimation of possible mechanisms of *Escherichia coli* inactivation by plasma treated sodium chloride solution *Plasma Process. Polym.* **8** 904–13
[231] Sakiyama Y, Graves D B, Chang H-W, Shimizu T and Morfill G E 2012 Plasma chemistry model of surface microdischarge in humid air and dynamics of reactive neutral species *J. Phys. D: Appl. Phys.* **45** 425201
[232] Vinogradov I P, Dinkelmann A and Lunk A 2004 Measurement of the absolute CF_2 concentration in a dielectric barrier discharge running in argon/fluorocarbon mixtures *J. Phys. D: Appl. Phys.* **37** 3000–7
[233] Smith M A H, Devi V M, Benner D C and Rinsland C P 2001 Absolute intensities of $^{16}O_3$ lines in the 9–11 μm region *J. Geophys. Res.* **106** 9909–21
[234] Pipa A V and Ropcke J 2009 Analysis of the mid-infrared spectrum of the exhaust gas from an atmospheric pressure plasma jet (APPJ) working with an argon-air mixture *IEEE Trans. Plasma Sci.* **37** 1000–3
[235] Melen F and Herman M 1992 Vibrational bands of $H_xN_yO_z$ molecules *J. Chem. Ref. Data* **21** 831–81
[236] Brown L R, Farmer C B, Rinsland C P and Toth R A 1987 Molecular line parameters for the atmospheric trace molecule spectroscopy experiment *Appl. Opt.* **26** 5154–82
[237] Hanst P L and Hanst S T 1993 *Infrared Spectra for Quantitative Analysis of Gases* (Infrared Analysis Inc.)
[238] Schmidt-Bleker A, Winter J, Iseni S, Dunnbier M, Weltmann K D and Reuter S 2014 Reactive species output of a plasma jet with a shielding gas device-combination of FTIR absorption spectroscopy and gas phase modelling *J. Phys. D: Appl. Phys.* **47**
[239] Winter J, Hänel M, Dünnbier M and Reuter D S 2014 Ambient humidity has minor influence on OH emission of an atmospheric pressure argon plasma jet than feed gas humidity *Application Report*
[240] Reuter S, Winter J, Iseni S, Schmidt-Bleker A, Dunnbier M, Masur K, Wende K and Weltmann K-D 2014 The influence of feed gas humidity versus ambient humidity on atmospheric pressure plasma jet-effluent chemistry and skin cell viability *IEEE Trans. Plasma Sci.* accepted
[241] Röpcke J, Davies P B, van Helden J H, Hübner M, Lang N and Welzel S 2014 Fundamental and applied studies of molecular plasmas using infrared absorption techniques *Springer Series on Atomic, Optical, and Plasma Physics* vol 82, pp 235–66
[242] Ropcke J, Lombardi G, Rousseau A and Davies P B 2006 Application of mid-infrared tuneable diode laser absorption spectroscopy to plasma diagnostics: a review *Plasma Sourc. Sci. Technol.* **15** S148–68
[243] Pipa A V, Bindemann T, Foest R, Kindel E, Ropcke J and Weltmann K D 2008 Absolute production rate measurements of nitric oxide by an atmospheric pressure plasma jet (APPJ) *J. Phys. D: Appl. Phys.* **41** 194011
[244] Pipa A V, Reuter S, Foest R and Weltmann K D 2012 Controlling the NO production of an atmospheric pressure plasma jet *J. Phys. D: Appl. Phys.* **45** 085201
[245] McManus J B, Nelson D, Zahniser M, Mechold L, Osiac M, Röpcke J and Rousseau A 2003 TOBI: a two-laser beam infrared system for time-resolved plasma diagnostics of infrared active compounds *Rev. Sci. Instrum.* **74** 2709
[246] Chen W, Cousin J, Poullet E, Burie J, Boucher D, Gao X, Sigrist M W and Tittel F K 2007 Continuous-wave mid-infrared laser sources based on difference frequency generation *C. R. Phys.* **8** 1129–50
[247] van Helden J H, Hancock G, Peverall R and Ritchie G A D 2011 A 3 μm difference frequency laser source for probing hydrocarbon plasmas *J. Phys. D: Appl. Phys.* **44** 125202
[248] Faist J, Capasso F, Sivco D L, Sirtori C, Hutchinson A L and Cho A Y 1994 Quantum cascade laser *Science* **264** 553–6
[249] Capasso F 2010 High-performance midinfrared quantum cascade lasers *Opt. Eng.* **49** 111102
[250] Curl R F, Capasso F, Gmachl C, Kosterev A A, McManus B, Lewicki R, Pusharsky M, Wysocki G and Tittel F K 2010 Quantum cascade lasers in chemical physics *Chem. Phys. Lett.* **487** 1–18
[251] Li J S, Chen W and Fischer H 2013 Quantum cascade laser spectrometry techniques: a new trend in atmospheric chemistry *Appl. Spectrosc. Rev.* **48** 523–59
[252] Welzel S, Hempel F, Hubner M, Lang N, Davies P B and Ropcke J 2010 Quantum cascade laser absorption spectroscopy as a plasma diagnostic tool: an overview *Sensors* **10** 6861–900
[253] Hancock G, Ritchie G, van Helden J P, Walker R and Weidmann D 2010 Applications of midinfrared quantum cascade lasers to spectroscopy *Opt. Eng.* **49** 111121
[254] Hugi A, Maulini R and Faist J 2010 External cavity quantum cascade laser *Semicond. Sci. Technol.* **25** 083001
[255] Walker R J, van Helden J H and Ritchie G A D 2010 Quantum cascade laser absorption spectroscopy of the band of deuterium bromide at 5 μm *Chem. Phys. Lett.* **501** 20–4
[256] Lopatik D, Lang N, Macherius U, Zimmermann H and Röpcke J 2012 On the application of cw external cavity quantum cascade infrared lasers for plasma diagnostics *Meas. Sci. Technol.* **23** 115501
[257] van Helden J H, Lopatik D, Nave A, Lang N, Davies P B and Röpcke J 2015 High resolution spectroscopy of silane with an external-cavity quantum cascade laser: Absolute line strengths of the ν_3 fundamental band at *J. Quant. Spectrosc. Radiat. Transfer* **151** 287–94
[258] van Helden J H, Lang N, Macherius U, Zimmermann H and Röpcke J 2013 Sensitive trace gas detection with cavity enhanced absorption spectroscopy using a continuous wave external-cavity quantum cascade laser *Appl. Phys. Lett.* **103** 131114 (Addendum: 2014 *Appl. Phys. Lett.* **104** 099901)
[259] Hubner M, Welzel S, Marinov D, Guaitella O, Glitsch S, Rousseau A and Ropcke J 2011 TRIPLE Q: a three channel quantum cascade laser absorption spectrometer for fast multiple species concentration measurements *Rev. Sci. Instrum.* **82** 093102
[260] Marinov D, Lopatik D, Guaitella O, Hübner M, Ionikh Y, Röpcke J and Rousseau A 2012 Surface vibrational relaxation of N_2 studied by CO_2 titration with time-resolved quantum cascade laser absorption spectroscopy *J. Phys. D: Appl. Phys.* **45** 175201
[261] Marinov D, Lopatik D, Guaitella O, Ionikh Y, Röpcke J and Rousseau A 2014 Surface deactivation of vibrationally excited N_2 studied using infrared titration combined with quantum cascade laser absorption spectroscopy *J. Phys. D: Appl. Phys.* **47** 015203
[262] Lopatik D, Marinov D, Guaitella O, Rousseau A and Röpcke J 2013 On the reactivity of plasma-treated photo-catalytic TiO_2 surfaces for oxidation of C_2H_2 and CO *J. Phys. D: Appl. Phys.* **46** 255203
[263] Lopatik D, Niemietz S, Frohlich M, Ropcke J and Kersten H 2012 Plasma chemical study of a RF discharge containing aluminum tri-isopropoxide using MIR absorption spectroscopy based on external-cavity quantum cascade lasers *Control. Plasma Phys.* **52** 864–71

[264] Hubner M, Marinov D, Guaitella O, Rousseau A and Ropcke J 2012 On time resolved gas temperature measurements in a pulsed dc plasma using quantum cascade laser absorption spectroscopy *Meas. Sci. Technol.* **23**

[265] Stancu G D, Simeni M S and Laux C O 2013 Study of nitric oxide and carbon monoxide production in plasma assisted combustion by quantum cascade laser absorption spectroscopy *Proc. of the 21st ISPC (Cairns, Australia, 2013)*

[266] Iséni S, Reuter S and Weltmann K-D 2014 NO_2 dynamics of an Ar/Air plasma jet investigated by *in situ* quantum cascade laser spectroscopy at atmospheric pressure *J. Phys. D: Appl. Phys.* **47** 075203

[267] Gaens W V, Iseni S, Schmidt-Bleker A, Winter J, Weltmann K-D, Reuter S and Bogaerts A 2014 Numerical analysis of the effect of nitrogen and oxygen admixtures on the chemistry of a plasma jet operating in argon. *New J. Phys.*